METAL-ORGANIC FRAMEWORKS FOR LONG-TERM VACCINE STORAGE

A Dissertation
Presented to
The Academic Faculty

by

Rohan A. Murty

In Partial Fulfillment
of the Requirements for the Degree
Doctor of Philosophy in the
School of Chemical and Biomolecular Engineering

Georgia Institute of Technology
December 2022

METAL-ORGANIC FRAMEWORKS FOR LONG-TERM VACCINE STORAGE

Approved by:

Dr. Mark R. Prausnitz, Advisor
School of Chemical and Biomolecular Engineering
Georgia Institute of Technology

Dr. Blair K. Brettmann
School of Chemical and Biomolecular Engineering and School of Materials Science and Engineering
Georgia Institute of Technology

Dr. Krista S. Walton, Advisor
School of Chemical and Biomolecular Engineering
Georgia Institute of Technology

Dr. M.G. Finn
School of Chemistry and Biochemistry
Georgia Institute of Technology

Dr. Andreas S. Bommarius
School of Chemical and Biomolecular Engineering
Georgia Institute of Technology

Date Approved: October 24, 2022

To my family and friends.

For keeping me grounded.

ACKNOWLEDGEMENTS

It takes a village to defend a PhD, and I was fortunate to have a wonderful set of mentors, colleagues, friends, and family throughout my graduate school journey. First and foremost, I must thank Prof. Mark Prausnitz and Prof. Krista Walton for their invaluable guidance, insight, and emotional support these last five years. None of us knew exactly what we were getting into when we started in the fall of 2017, but Mark and Krista expertly navigated their first co-advised student, and we ultimately ended up with some very cool results. I would also like to acknowledge Prof. Andreas Bommarius, Prof. Blair Brettmann, and Prof. M.G. Finn—the members of my doctoral committee—for asking the right questions and helping to identify gaps in my research.

One of the best parts of graduate school is the collaborative atmosphere and the ability to learn from those who know more than you (*i.e.*, everyone during the first few years). I would like to thank Dr. Ian Walton for providing expert insights into MOF chemistry and for helping us start the collaboration with Argonne National Labs— these experiments ended up forming an entire aim of my thesis. I would also like to thank Dr. Mrinal Bera for running many, many remote SAXS experiments and bringing the perspective of a physicist to our discussions. All synchrotron experiments were conducted at NSF's ChemMatCARS Sector 15 at Argonne National Labs (supported by grant number NSF/CHE-1834750). This research used resources of the Advanced Photon Source, a U.S. Department of Energy (DOE) Office of Science User Facility operated for the DOE Office of Science by Argonne National Laboratory under Contract No. DE-AC02-06CH11357.

In the Prausnitz Lab, I must thank Dr. Andrey Romanyuk, Dr. Pradeep Bhumireddy, and Juan Mena for helping with experiments. Andrey was always ready to answer my ELISA questions and ran all the live-animal experiments for the tetanus project. Pradeep was invaluable in getting good Confocal images, and Juan ran OCT for my first lead author publication.

At an elite graduate institution like Georgia Tech, I often worked with undergraduates that were smarter than me. To my three stellar undergraduate students Christina Whetzel, Isabella Bowland, and Abishek Sankaranarayanan, I must give a huge thanks for their efforts in churning out key data for our publications. I am very lucky to have played a small part in their training at Georgia Tech and am excited to see what cool discoveries Abishek and Isabella will make during their graduate school careers at Wash U and MIT.

Thanks to all the Prausnitz lab members past and present, especially Dr. Amir Hejri, Dr. Joshua Palacios, Dr. Simple Kumar, Amy, Youngeun, Kunal, Thy, Mikayla, and many others for interesting questions at group meetings and (perhaps more importantly) great times at lab barbecues, MLK day parties, and epic group retreats in the panhandle. I would like to thank Donna Bondy for always having solutions to my problems and being a consistent source of positivity in the Prausnitz lab. Thanks also to Marnie McMurry for helping with borderline insane scheduling requests these last few years. Of course, I must also thank the many Walton lab members that made for such a memorable graduate school experience: Dr. Danny Shade, Dr. Carmen Chen, Tania, Lukas, Brandon, and all the rest.

I was lucky to have many brilliant classmates that also knew how to unwind after a long week. I must specifically thank Dr. Conrad Roos for being a fantastic roommate throughout my time in graduate school, but also need to acknowledge Dr. Maggie Manspeaker and Dr. William Bradley for the many coffee dates, lunches, dinners, and interesting conversations over the years.

Thanks to the oldest friends in the Signal chat: Sriram, Karun, Nitin, Charles, Jake, and Will, for keeping me laughing and being the best travel partners. Thanks also to the pandemic friends who ended up becoming some of my best friends; the thousands of cumulative hours spent in Discord calls with Kevin, John, and Colton helped to remind me that there is more to life than graduate school. I also must deeply thank Lauren for being an incredible source of comfort, happiness, and advice. I would have lost my mind several times over without her input and reassurance.

Finally, I would like to thank my mother and father for the endless emotional (not to mention, financial) support throughout my life. Making my parents proud has been one of my strongest motivators in graduate school, and I hope they are excited to finally be able to call their son “doctor.” I would also like to thank my brother, Sanjeev, for inspiring me with his genius, hosting me so many times in New York, and for always having interesting takes on current events.

TABLE OF CONTENTS

LIST OF TABLES

LIST OF FIGURES

LIST OF SYMBOLS AND ABBREVIATIONS

ATR	Attenuated total reflection
BSA	Bovine serum albumin
BSA@ZIF-8	Bovine serum albumin encapsulated in zeolitic imidazolate framework-8
BSA@ZIF-67	Bovine serum albumin encapsulated in zeolitic imidazolate framework-67
BSL	Biosafety level
CDC	Center for disease control
CMC	Carboxymethyl cellulose
CLSM	Confocal laser scanning microscopy
DI	Deionized (water)
D_{max}	Maximum interatomic distance
DOX	Doxorubicin
DSF	Differential scanning fluorimetry
DTaP	Diphtheria, Tetanus, and Pertussis vaccine
ELISA	Enzyme-linked immunosorbent assay
EPIT	Epicutaneous immunotherapy
Et	Ethanol
FTIR	Fourier transform infrared spectroscopy
Immunoglobulin G	IgG
H&E	Hematoxylin and eosin
HRP	Horseradish peroxidase
IPV	Inactivated poliovirus vaccine
I(q)	SAXS intensity as a function of the scattering vector

MMR	Measles, mumps, and rubella vaccine
MN	Microneedle
MNP	Microneedle patch
mRNA	Messenger ribonucleic acid
MOF	Metal-Organic Framework
OCT	Optical coherence tomography
OIT	Oral immunotherapy
OPV	Oral poliovirus vaccine
PDDF	Pair distance distribution function
PG	Propylene glycol
P(r)	Pair distribution function
pXRD	Powder X-ray diffraction
Q	Scattering vector in SAXS spectra
R_g	Radius of gyration
RT	Room temperature
SAXS	Small angle X-ray scattering
SCIT	Subcutaneous allergen immunotherapy
SEM	Scanning electron microscopy
SUV	Subunit vaccine
TT	Tetanus toxoid
TT@ZIF-8	Tetanus toxoid encapsulated in zeolitic imidazolate framework-8
T_m	Melting temperature (of a protein)
TMV	Tobacco mosaic virus
VLP	Virus-like particle
WHO	World health organization

XRD	X-ray diffraction
ZIF	Zeolitic imidazolate framework
ZIF-8	Zeolitic imidazolate framework-8
ZIF-67	Zeolitic imidazolate framework-67

SUMMARY

Vaccination campaigns have significantly improved financial, social, and health outcomes globally. In post-industrial nations, immunization rates for diseases like Diphtheria, Tetanus, and Pertussis are 90 – 99% for infants. Yet, in several developing African and southeast Asian countries, early childhood coverage for these vaccines is 50% or lower. This striking disparity is partially explained by logistical challenges associated with transporting and storing vaccines in warm, tropical climates. Because vaccines are highly temperature-sensitive, short lapses in refrigeration can cause irreversible potency losses. Indeed, such failures in this "cold chain" significantly damage up to 50% of all vaccines globally.

A recently discovered approach for stabilizing biomacromolecule guests involves encapsulating proteins or viruses inside metal-organic frameworks (MOFs), a class of porous materials formed by the coordination of metal centers and organic ligands. By growing MOF scaffolds around guest molecules, previous groups have shown that significant thermostability can be imparted, perhaps offering an opportunity to eliminate refrigeration during vaccine storage/transport. To date, almost all studies on MOF biocomposites have focused on model guests of low clinical relevance and have not examined the long-term thermostability of these materials. Additionally, the supposed mechanism of enhanced thermostability has not yet been supported by strong experimental evidence.

In CHAPTER 3, we sought to address these literature gaps by encapsulating the clinically relevant Tetanus Toxoid (TT) vaccine within the MOF structure zeolitic-

imidazole framework-8 (ZIF-8). We first employed a variety of crystallographic, spectroscopic, and microscopic methods to confirm that TT was encapsulated and fully distributed within the bulk of the TT@ZIF particles, and that this incorporation did not significantly disrupt the ZIF's crystalline structure. To characterize the long-term thermostability of TT@ZIF, we conducted accelerated stability studies at 40˚C and 60˚C, studying dried preparations, aqueous suspensions, and organic suspensions of TT@ZIF. The best thermostability results were obtained for TT@ZIF suspended in a mixture of propylene glycol and ethanol, which retained ~90% TT stability for 3 months at 40˚C. In contrast, the aqueous liquid TT vaccine lost ~90% activity in the same conditions.

In CHAPTER 4, we employed small angle x-ray scattering (SAXS) to provide evidence for the hypothesized mechanism of improved thermostability afforded by MOF encapsulation. By studying bovine serum albumin (BSA) encapsulated in two ZIFs, we found that scaled subtraction of the pure ZIF spectra from the BSA@ZIF biocomposite spectra yielded the encapsulated BSA spectra. Analysis of pair distribution functions and Kratky plots showed that when exposed to a temperature of 70˚C, ZIF-encapsulated BSA showed no signs of unfolding or aggregation while the free-standing BSA denatured completely. This finding supported the prevailing literature hypothesis that rigid confinement of guest biomacromolecules within roughly guest-sized MOF cavities prevents unfolding, and thus, activity losses resulting from thermal exposure.

Ultimately, the work presented here demonstrates the feasibility of vaccine-MOF materials for long-term storage of clinically relevant guests, offering a viable approach for breaking the cold chain with a highly stable liquid formulation. Suspending TT@ZIF in a biocompatible organic solvent afforded ≥80% stability retention for 3 months at

temperatures as high as 60˚C, representing a marked improvement over liquid and lyophilized TT vaccine stability. MOF encapsulation provides several benefits over standard vaccine stabilization approaches as it is cheap, may be produced in a continuous process, and eliminates the need for reconstitution. Our work also provided evidence for the mechanism of heightened thermostability seen in ZIF biocomposites, which appears to rely on rigid guest confinement within the MOF cavities. This finding may be used in the rational design of even more stable vaccine-ZIF formulations in the future. Furthermore, the SAXS spectra subtraction approach established in our work may be abstracted to other inorganic-organic host-guest systems, perhaps enabling new insights in other fields.

CHAPTER 1. INTRODUCTION

Immunization campaigns have markedly improved financial, social, and health outcomes globally. Vaccination rates for common vaccines like diphtheria, pertussis, and tetanus (DTaP) are exceptionally high in post-industrial nations, averaging around 90% coverage for infants in the first year of life. Yet, in the developing world, there is a significant lack of vaccine access for easily preventable diseases. Just this year, the World Health Organization (WHO) estimated there were 25 million infants who did not receive a full immunization schedule for the DTaP vaccine, with over 60% of these children residing in certain African and southeast Asian countries.

The massive disparity between vaccination rates in underdeveloped nations is largely explained by logistical issues, notably including the refrigeration cold chain. Since vaccines contain highly temperature-sensitive biological macromolecules such as proteins and live viruses, they must typically be maintained at a range of 4 – 8°C from the moment of manufacture until they are finally administered months to years later. This poses a significant barrier to widespread immunization campaigns in the developing world, as harsh climates and inconsistent access to electricity make cold chain failures frequent. Indeed, the WHO estimates that up to 50% of all vaccines globally are lost to errors in cold chain transport and storage.

There already exist several methods for stabilizing vaccines at elevated temperatures such as freeze-drying, excipient addition, and incorporating vaccines into highly stable polymeric matrices; however, these solutions each have their associated drawbacks. Lyophilization is an expensive batch process requiring reconstitution before

administration, excipient screening for specific formulations is time-consuming, and scale-up barriers exist for novel solutions like polymeric microneedle patches. Notably, these stabilization methods have had limited impact on the cold chain, since almost all vaccines still require continuous refrigerated storage.

In this work, we consider a novel method for vaccine stabilization employing metal-organic frameworks (MOFs), a class of highly tunable and crystalline porous materials formed by the coordination of metal centers and organic ligands. Through a self-assembly reaction know as biomimetic mineralization, MOF structures may be grown around a variety of biological guests (*e.g.*, proteins, viruses, and cells), imparting significant chemical and thermostability in the process. These highly stable vaccine-MOF biocomposites may offer a cheap, abstractable method for breaking the cold chain, but there remain several unanswered questions in the literature due to the nascent nature of the field.

Because MOF encapsulation for heightened guest stability only emerged within the last decade, most existing studies focus on model proteins with little or no clinical relevance like bovine serum albumin (BSA). Furthermore, while many groups have shown the resilience of these materials in harsh conditions, recent studies have only examined the timescale of days, leaving the long-term stability of these biocomposites in question. This point is of particular relevance for breaking the cold chain, since vaccine formulations are often expected to be shelf-stable for years. Finally, while many have speculated on the mechanism of heightened thermostability afforded by encapsulation within MOFs (*i.e.*, rigid confinement of the protein prevents unfolding), direct evidence for this has not yet been provided. Our work seeks to address these gaps with two distinct research aims:

1.1 Thermostability and immunogenicity of tetanus vaccine encapsulated in a metal-organic framework

In an effort to conduct studies on a guest with high clinical relevance, we encapsulated tetanus toxoid (TT) vaccine within a zeolitic imidazolate framework (ZIF) to create the biocomposite TT@ZIF. After confirming encapsulation and release from the framework with a variety of crystallographic, spectroscopic, and microscopic methods, we examined the long-term durability of TT@ZIF through accelerated stability studies performed at elevated temperatures of 40°C and 60°C. We analyzed several different formulations including a dry powder, aqueous suspension, and an organic suspension to circumvent the poor water stability of ZIFs. We also subjected TT@ZIF to an extreme temperature of 120°C as well as several freeze/thaw cycles to test its upper thermostability limits. With these experiments, we sought to assess the MOF encapsulation approach on a pertinent vaccine guest as well as provide insights on the question of long-term biocomposite stability using Arrhenius modeling. Finally, we measured immune responses *in vivo* through a murine model to assess the immunogenicity of TT@ZIF formulations.

1.2 Interrogating encapsulated protein structure within metal-organic frameworks

After characterizing TT@ZIF in detail and stress-testing its thermostability, we attempted to provide experimental evidence for the heightened stability mechanism observed in MOF biocomposites. This was achieved through collaboration with the Advanced Photon Source at Argonne National Labs in Lemont, Illinois. By employing *in situ* synchrotron-source small angle x-ray scattering (SAXS) on BSA encapsulated within two isostructural zeolitic imidazolate frameworks (ZIF-8 and ZIF-67), we pioneered a

spectra subtraction approach that elucidated the stability mechanism. Scaled subtraction of the pure MOF spectra from the BSA@ZIF biocomposites' yielded the encapsulated protein spectra, allowing size and structural analysis of still-encapsulated proteins. *In situ* heating of BSA@ZIF during SAXS measurements afforded insights into the action of heightened thermostability, which appeared to rely on rigid confinement of the guest's tertiary structure, preventing unfolding. The subtraction approach defined in this work may be extracted to other inorganic-organic biocomposite systems, and improved understanding of the enhanced stability may enable better rational design of MOF biocomposites.

CHAPTER 2. BACKGROUND

2.1 Vaccines, immunization campaigns, and combatting the cold chain

The world was forever changed by Edward Jenner's discovery of the smallpox vaccine in the late 18th century, which significantly improved life expectancy and spawned the brand new field of vaccine development [1]. In the following centuries, dozens of vaccines entered the market, and in 2014 the total market size of vaccine manufacturers was estimated to be $26.7 billion, likely growing to exceed $35 billion with the advent of the COVID-19 pandemic [2, 3]. And while vaccine distribution has seen great success in post-industrial nations like the USA and Japan, there is a marked lack of vaccine accessibility in the developing world [4]. This discrepancy is partially explained by the necessity of vaccines to be refrigerated from the moment of manufacture until administration, colloquially known as the "cold chain" [5]. This problem is so significant that the World Health Organization (WHO) estimates 50% of all vaccines are lost annually due to incorrect adherence to cold chain protocols [6].

In this section, we first include an overview of several common vaccine types. Next, we provide a brief summary of tetanus infection and its toxoid vaccine, which is of particular interest because we attempt to optimize its thermostability in CHAPTER 3. This is followed by a discussion of the status and associated challenges for immunization campaigns in the developing world. Finally, we provide details on the cold chain, its failure rates, and current methods for vaccine stabilization.

2.1.1 Types of vaccines

Presently, there are several broad categories of commonly used vaccines including live attenuated, inactivated, toxoid, subunit, virus-like particles (VLPs) and, most recently, mRNA [7]. Despite differences in structure and formulation, the general approach of vaccines is roughly the same: introducing a small dose of the antigen for which disease tolerance is desired enables production of pathogen-specific immune responses in the body [8]. By this mechanism, the vaccinated individual generates antibodies and/or cellular responses that can be used to combat foreign antigens at a later time, significantly reducing (or sometimes eliminating) symptoms associated with the disease.

2.1.1.1 Live attenuated vaccines

First introduced by Jenner's work on smallpox in 1798, the live attenuated vaccine is one of the most ubiquitous vaccine types, affording immunization against measles, mumps, rubella (MMR), influenza, and many other harmful diseases [7]. In this vaccination approach, the wild type target virus or bacteria is first isolated and then weakened, usually by repeated cell culturing [9]. This weakened (*i.e.*, attenuated) virus is then used to vaccinate people to generate the desired immune response [10]. While this type of vaccine has seen overwhelming success in the past two centuries, there are non-trivial associated risks such as adverse events following immunization, as seen during administration of the oral polio vaccine [11]. Furthermore, live attenuated vaccines such as MMR are highly temperature-sensitive, rendering distribution in developing nations a serious challenge [12].

2.1.1.2 Inactivated viral vaccines

Because of the relatively high rate of adverse effects associated with live attenuated vaccines such as the oral polio vaccine, scientists often employ inactivated viral vaccines to protect against viral pathogens [13]. In contrast to attenuated vaccines, viral inactivation by heat treatment or addition of formaldehyde completely kills the target virus. This approach lowers the rate of adverse effects upon administration, one common comparison being inactivated poliovirus (IPV) versus the attenuated oral poliovirus (OPV) [14]. While vaccine-associated paralysis only occurs once per several million OPV administrations, IPV is incapable of causing polio in vaccinated individuals. The increased safety associated with inactivated viruses can, however, be accompanied by a reduction in immunity provided. As such, boosters are more frequently required for vaccinations using this approach [9].

2.1.1.3 Toxoid vaccines

For diseases caused by bacterial toxins (such as diphtheria and tetanus), toxoid vaccines are typically employed. The approach for preparing toxoids is fundamentally similar to that used for inactivated vaccines; the bacterial toxin (*i.e.*, tetanus toxin) is first isolated from a culture and then neutralized by heat treatment or addition of formalin [15]. With this method, the toxin is converted to the toxoid form, which is less dangerous for individuals and therefore more suitable for inducing a protective immune response. Naturally, inactivating the toxin protein with thermal and chemical treatments can lead to at least partial loss of immunogenicity, posing a trade-off between safety and vaccine efficacy [16].

2.1.1.4 Subunit vaccines

The safety issues often encountered with live attenuated vaccines may be addressed by administration of subunit vaccines (SUVs), which are composed of only the necessary microbial components (*i.e.,* the antigen) needed to induce the desired immune response [17]. These vaccines are generally safer to use in immunosuppressed patients since they cannot cause the target disease and are associated with a lower rate of side-effects [18]. Although only a few SUVs have entered the market, one greatly successful formulation is for hepatitis B, which is composed primarily of the hepatitis B surface antigen [19]. The relatively small number of commercially successful SUVs despite extensive research efforts may suggest that there are serious challenges associated with their development, such as lowered immunogenicity and understanding which antigen components are responsible for generating an immune response [17].

2.1.1.5 Virus-like particles

A slightly more modern approach to vaccination involves a class of SUVs named virus-like particles [7, 20]. Seeking to counter the lower immunogenicity often associated with standard subunit vaccines, VLPs are formed by the self-assembly of structural viral proteins [21]. These vaccines therefore possess the benefit of having greater immunogenicity than SUVs while also remaining non-infective. Indeed, almost all SUVs on the market are actually VLPs, highlighting the success of this vaccine type. VLPs may also be used to deliver immunizations for several antigens in a single formulation [22]. Despite the numerous advantageous of this approach, VLPs have only existed for a few decades (compared to other vaccines which have been employed successfully for centuries), posing several unanswered questions regarding their efficacy, structure, and mechanisms of action.

2.1.1.6 mRNA vaccines

Due to the COVID-19 pandemic, mRNA vaccines have exploded in popularity and use [23]. This vaccination approach relies on the uptake of mRNA (usually introduced through delivery vehicles such as lipid nanoparticles) into cells, where it is translated into antigens that generate the desired immune response. Notably, these vaccines do not integrate into the genome. This approach possesses a number of benefits, including cell-free manufacturing and the capability of encoding for multiple antigens within a single mRNA vaccine formulation. One of the most important drawbacks for this vaccine type, especially relevant to the work done in this thesis, is the extremely poor thermostability [24]. Some COVID vaccines require storage at temperatures as low as -70°C, posing serious challenges for their rollout and use in developing nations [25].

2.1.2 Tetanus and its toxoid vaccine

Of the various vaccine types discussed so far, the toxoid is the most relevant to our studies as we seek to stabilize tetanus toxoid vaccine in CHAPTER 3. Tetanus is a disease caused by the tetanospasmin toxin produced in the bacterium *Clostridium tetani* [26]. Those suffering from exposure to tetanus toxin may experience spasms and muscle rigidity, commonly resulting in lockjaw. Without medical intervention, the mortality rate of tetanus approaches 100%, underscoring the importance of widespread immunization campaigns against this life-threatening disease [27]. Furthermore, because tetanus infections result from broken skin coming in contact with surfaces containing *Clostridium tetani*, herd immunity cannot protect an exposed, unvaccinated individual, meaning that 100% vaccination coverage is needed [7].

As described in Section 2.1.1.3, the tetanus toxoid vaccine is produced by exposing the toxin (purified from bacterial culture) to formaldehyde, thereby inactivating its pathogenic properties [28]. Typically administered in combination with diphtheria and pertussis vaccines (commonly known as DTaP), the CDC recommends that immunization follows a 5-dose schedule starting at the age of 2 months [29]. Studies on mortality rates for neonatal tetanus show that starting the vaccination schedule earlier in an infant's life is linked to improved outcomes [27]. Even though neonatal deaths attributed to tetanus have reduced by an order of magnitude in recent decades, the disease still disproportionately affects developing nations, motivating the optimized distribution of this life-saving vaccine [30].

2.1.3 Immunization campaigns in developing nations and the cold chain

Although immunization rates for common vaccines such as MMR and DTaP are extremely high (>90%) in the western world, underdeveloped nations still experience relatively high rates of infection and infant mortality from these preventable diseases [31]. The WHO estimates nearly 20 million infants did not receive a single dose of the DTaP vaccine in 2021 [32]. Even more alarming, the WHO suggests that worldwide vaccine coverage declined in the last decade, partially due to the unexpected stress placed on healthcare systems by the COVID-19 pandemic. Of the 25 million children that did not receive a full immunization schedule, the majority reside in just 10 African and southeast Asian countries. The CDC corroborates that global vaccination rates dropped in the last 3 years, correlating increased rates of diphtheria, tetanus and pertussis infections in developing nations to stagnating immunization campaigns, especially in certain regions of Africa [33].

Despite cultural barriers and vaccine hesitancy providing some challenges for more widespread vaccine coverage in regions of Africa, a major obstacle is careful maintenance of the cold chain during vaccine transport and storage [34, 35]. For example, a 2019 study in Ethiopia found that among 60 health institutions, only 46 had functional refrigerators, 29 were storing vaccines at the recommended temperature range, and just 23 had necessary knowledge about cold chain practices [36]. A similar assessment of 273 health institutions in Nigeria reported that only 73% were aware of vaccine handling guidelines, with incorrect handling practices occurring in 13.7% of studied cases [37]. The lack of adequate infrastructure and prevalence of incorrect vaccine storage in developing nations highlights the importance of solutions that do not necessitate constant access to electricity/refrigeration or extensive knowledge of logistical factors affecting vaccine storage conditions. In addition, cold chain adherence has proven to be expensive, with a global market size of several hundred billions of dollars [38].

2.1.4 Current vaccine stabilization approaches

Several approaches for vaccine and protein stabilization have been explored in order to minimize or avoid need for the cold chain. The most common methods include freeze-drying (lyophilization), excipient addition, and immobilization within matrices composed of polymers or silk [39]. Stabilizing vaccines is often necessary because their proteinaceous and biomacromolecule components are subject to unfolding, denaturation, and aggregation when exposed to adverse conditions, namely high temperatures [40]. As such, the various advantageous and drawbacks of each approach are summarized in the subsections below.

2.1.4.1 Freeze-drying (lyophilization)

The most extensively studied (and therefore, common) method for vaccine stabilization is lyophilization [40]. In this process, a liquid vaccine formulation is first frozen and then exposed to vacuum, which removes residual ice and water. This renders the vaccine a solid powder with improved thermostability since water is associated with many degradation and destabilization mechanisms [41]. Freeze-drying has been applied broadly to live attenuated vaccines, improving their shelf-life in normally denaturing conditions; however, there exist a number of drawbacks associated with this method. During the lyophilization process, exposure to freezing temperatures can cause activity loss, especially in live attenuated vaccines. Another issue with this approach is the loss of activity upon reconstitution resulting from aggregation within the solution [39]. The necessity for reconstitution before administration also raises the issue of poor vaccine handling knowledge in developing nations [37]. Lastly, lyophilization is also an expensive, energy-intensive process as it requires freezing samples to temperatures as low as -80°C.

2.1.4.2 Excipient addition

The addition of non-immunogenic stabilizers, known as excipients, to vaccine formulations is another widely employed approach to improving stability [42]. Common excipients include salts (*e.g.*, sodium chloride), surfactants (*e.g.*, polysorbate 80), and sugars and sugar alcohols, such as sucrose and mannitol, respectively [43]. The main challenge associated with excipient addition is the necessity for comprehensive studies on the ideal formulation; each different vaccine formulation will have a different combination of excipients that impart the greatest stabilizing effect, and studying these conditions

requires extensive screening [44]. Additionally, common excipients like gelatin, carboxymethylcellulose, and polyethylene glycols can cause vaccine hypersensitivity in individuals, sometimes resulting in anaphylaxis [45].

2.1.4.3 Stabilization within matrices

A slightly newer, albeit promising, method for vaccine stabilization involves formulation within polymer matrices. Embedding vaccines in microneedle patches (MNPs) represents a well-studied approach for immobilizing vaccines within a matrix to improve its thermostability [46]. The work of Prausnitz *et al*. has demonstrated the feasibility of MNPs to stabilize influenza, measles, and rubella vaccines [47, 48]. This method possesses the benefits of being abstractable to various vaccines, eliminating sharps waste, and removing the necessity for reconstitution before administration; however, producing polymeric MNPs at scale still requires significant infrastructure development and engineering [49].

2.2 Metal-organic frameworks for vaccine stabilization

2.2.1 Metal-organic framework and their biological applications

Metal-organic frameworks (MOFs) represent a class of tunable, ordered, nanoporous materials that have been used in gas separations, CO_2 capture, catalysis, and (most pertinently) drug delivery [50-52]. The expansive range of uses for these materials stems from the highly variable nature of their structure: MOFs are composed of metal clusters coordinatively linked by organic molecule bridges (*i.e.*, ligands), resulting in thousands of feasible metal/ligand combinations [53]. This has yielded over 20,000 distinct

structures, each possessing different physicochemical properties [54]. By modifying the precursors and synthesis conditions, scientists may carefully optimize intrinsic properties of a MOF (such as pore size or solvent stability) for specific applications [55]. Furthermore, some MOFs are easily functionalized via post-synthetic modification (PSM), allowing for the addition of imaging and/or targeting moieties to the framework without compromising its structure [56, 57]. The modifiable nature of these materials has led to the design of theranostic MOF-based drug delivery "vehicles," which combine therapeutics and diagnostics into a single platform [58].

When MOFs were initially synthesized, there was little promise for their use in biology and medicine, mainly because the first notable structures were composed of harmful precursors and suffered from abysmal water stability [59]. This attitude shifted in the mid-2000s with increasing reports of non-toxic MOFs possessing aqueous stability on the order of weeks. In the following years, several groups loaded small molecule drugs, such as doxorubicin and cidofovir, into the large pores of water-stable chromium-based MOFs like MIL-100 and MIL-101 and measured the drug release profiles [60, 61]. The drawback of all these frameworks but one (MIL-53) is the burst release of the cargo, owed largely to the diffusion-mediated transport from drug-loaded structures [62]. For this reason, zero-order degradation of the framework has been suggested as a possible route for sustained release with MOFs, as this would result in a more linear release profile [63, 64].

Another compelling and unique biomedical application for MOFs emerged in 2014, when Lyu *et al.* first demonstrated encapsulation of a PVP-modified protein (cytochrome C) in ZIF-8 with a one-pot synthesis method [65]. The advent of biomimetic mineralization in MOF/biomolecule systems was a significant advancement in the field, as the size of

potential guest species would no longer be limited by the small aperture (1 – 10 Å) of MOF pores. Furthermore, the ability to perform these syntheses in mild conditions (ambient pressure/temperature with only aqueous solvents) is especially favorable for biological systems because most proteins are natively stable in a narrow pH range [66, 67] . Since 2014, a wide variety of guests have been encapsulated through this process, including viruses, enzymes, DNA, proteins, and even live cells [68-71] . Although the primary exploration of these biocomposites has been focused on improving guest stability (*e.g.*, vaccine storage and biospecimen preservation) [64], some groups have also used MOF scaffolds to improve enzyme activity [65]. Others have exploited physicochemical properties of certain frameworks to mediate transport to and from encapsulated guests, thereby controlling biocatalysis rates [72].

2.2.2 Metal-organic framework for vaccine stabilization

Recently, protein-MOF biocomposites have been identified as a possible solution to the cold chain problem; a few MOFs have been shown to enhance protein stability in normally inhospitable conditions by acting as a "shield" [64, 68]. In 2015, a group demonstrated that encapsulating urease and horseradish peroxidase (HRP) inside a MOF shell allowed these guest proteins to retain activity even after being heated to 80 ℃, which would easily denature the unshielded guests [66]. MOFs can self-assemble around proteins by a process known as "biomimetic mineralization," which alludes to the growth of protective, inorganic shells on the soft tissues of species like sea urchins [73]. Zeolitic imidazolate framework 8 (ZIF-8) is a MOF that has drawn special attention for this pursuit due to its remarkable stability and low toxicity [74]. These characteristics, coupled with its

ability to be synthesized at room temperature (RT) in water, make ZIF-8 a promising choice for protein stabilization [66].

A crucial limitation of ZIF-8 for biological systems is its lack of long-term water stability, as the framework gradually degrades by hydrolysis over the scale of several days or weeks [75]. Still, the "Protein@MOF" biocomposite offers a more attractive route for long-term vaccine stabilization than standard freeze-drying methods since the latter approach may cause aggregation/loss of activity upon thawing and requires the added step of reconstitution at the administration site [76]. Additionally, unlike protein encapsulations in mesoporous silicas and similar materials, MOFs more efficiently limit guest leaching and are less particular about guest size as they grow around guests instead of being impregnated by them [69, 72, 77].

2.2.3 Properties of zeolitic imidazolate frameworks -8 and -67

For the goal of protein stabilization, no MOF has attracted greater attention than ZIF-8 due to its stability and synthetic accessibility in biologically agreeable conditions, namely RT water [78]. Long-term aqueous stability can be an important characteristic of MOFs for biomedical pursuits, thus the intrinsic qualities governing this trait merit discussion. While most water stability studies of MOFs have been performed in humid (gaseous) conditions [54], insights into the aqueous (liquid) stability may still be gleaned. Currently, MOF hydrostability is thought to improve with: number of coordination sites in the metal cluster, metal-ligand bond strength, outward facing hydrophobic groups, and minimal defects [79]. For ZIF-8, the latter factor may offer a foothold for optimization.

When ZIF-8 was first synthesized, early claims regarding its water stability were slightly misleading. Yaghi *et al.* reported in 2006 that solvothermal ZIF-8 retained crystallinity indefinitely in RT and boiling water [74]. In 2011, Pan *et al.* analyzed X-ray diffraction (XRD) patterns of RT-synthesized ZIF-8 and suggested that the structure was stable in boiling water for up to five days [80]. Although XRD patterns for ZIF-8 do remain largely unchanged after aging in water for several days, some groups have observed marked morphological changes in the structure with scanning electron microscopy (SEM) during this time frame [75, 81]. In the last decade as more aqueous-based applications of ZIF-8 have been identified, there has been increasing focus on the veracity of these initial stability claims. In a 2019 paper, Zhang *et al*. performed a thorough SEM study on RT-synthesized ZIF-8 and concluded that the crystalline structure was only stable in 20°C water for less than a day [75]. The authors also examined the effect of the ZIF-8:H_2O ratio, suggesting this value to be a key determinant of structural stability (with a higher value resulting in better structural retention).

Much of the disagreement surrounding the true stability of ZIF-8 may be tied to inconsistencies in synthesis methods used to prepare this framework, and to a lesser degree variability in stability testing conditions. A 2018 paper concerning biospecimen preservation with ZIF-8 avoids the hydrostability problem altogether by separating the solid Protein@ZIF-8 composite from its suspension and storing/aging it as a dry powder [82]. While this approach necessitates reconstitution of the dried biocomposite into a liquid at the administration site, it may provide a compelling avenue toward MNP incorporation. Nonetheless, accurate characterization of the water stability of Protein@ZIF materials (and

subsequent optimization) will be a key step toward the widespread feasibility of MOFs for improved guest robustness.

2.2.4 Toxicity considerations for metal-organic frameworks

When investigating MOFs as potential drug carriers in the human body, the natural question regarding the toxicity of these materials arises. While the steady biodegradation of certain frameworks offers a compelling route towards sustained drug release, the rapid decomposition of MOFs (such as ZIF-8) has been linked to substantial loss of cell viability in vitro [83], as high ligand concentrations may be cytotoxic. As a result, groups have begun tuning ZIF-8 drug release platforms to control the degradation rate, thereby improving overall biocompatibility [84]. Assessing the safety of MOF-based drug delivery systems is especially difficult because of synergistic effects between the carrier and the cargo. For example, in 2016 Zheng *et al.* loaded the anticancer drug doxorubicin (DOX) into ZIF-8 pores and observed a greater rate of induced apoptosis from the DOX@ZIF-8 composite than from pure ZIF-8 crystals and free DOX [83]. Thus, the toxicity of Drug@MOF and Protein@MOF composites must be examined on a case-to-case basis as these synergistic effects are still poorly understood.

Interrogating the biocompatibility of MOFs is made more complex by the poor water stability of many frameworks, which necessitates the simultaneous study of the toxicity of the MOF itself alongside that of its degradation products [85]. As such, few comprehensive MOF toxicity studies exist, with no reports of these materials being delivered into a human system. One reasonably thorough 2015 paper compares the *in vivo* (zebrafish embryo) and *in vitro* (HepG2 and MCF7 cells) cytotoxicities of 9 representative

pure MOF compounds [86]. While the findings from this paper are not generalizable to actual MOF drug delivery platforms (since they did not examine combined effects of MOFs and drugs administered together), the authors suggest a strong correlation between *in vivo* and *in vitro* toxicity results. Nevertheless, further investigation into MOF safety is necessary as the effect of crystal size, shape, charge, *etc.* are unknown, and may all play a role in the ultimate biological feasibility of these materials [86].

2.3 Small angle X-ray scattering

One of the most consequential experimental techniques employed in this work is small angle x-ray scattering (SAXS), as in CHAPTER 4 we used this method to elucidate the mechanism of heightened thermostability observed in vaccine-MOF biocomposites. SAXS measurements are often collected at beamlines such as the Advanced Photon Source (Lemont, IL), where synchrotron source radiation allows the collection of high-resolution SAXS data in just a few hours [87]. In this section, we describe the fundamentals of this technique before discussing applications of SAXS for biological molecules (*i.e.*, proteins) as well as the various data analysis methods employed in CHAPTER 4.

2.3.1 Fundamentals of SAXS

SAXS is a technique by which the size, shape, and conformation of proteins may be quantified [88]. In a typical experiment, a 2-D detector is used to measure the scattering of incident x-rays after they have interacted with the 3-D electronic structure of the sample. A scattering vector **q** is taken to represent the elastic scattering of the x-ray by some angle 2θ, and the 2-D data is then reduced to a 1-D intensity profile by integration. A simplified

experimental setup is shown in Figure 2.1, and depicts the geometric relationship between the scattering vector and the incident beam [89].

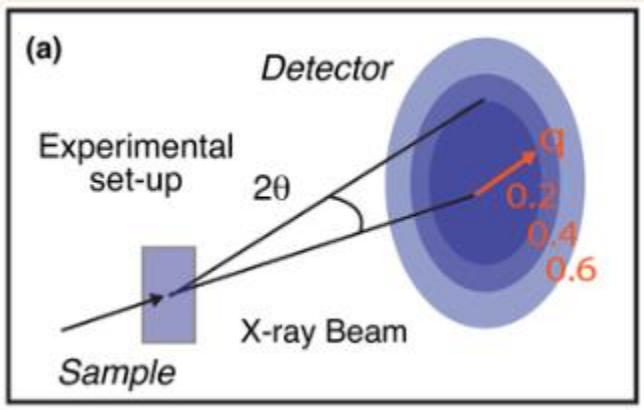

Figure 2.1: Schematic of small angle x-ray scattering setup depicting geometry of the scattering vector "q." Adapted from the work of Brosey, *et al.* [89].

Unlike other scattering techniques such as x-ray diffraction, the intensity of the scattered radiation in SAXS is not expressed as function of the angle 2θ, rather as a trigonometric function of the angle divided by the x-ray wavelength λ. This relationship is shown below:

$$\boldsymbol{q} = \frac{4\pi \sin(\theta)}{\lambda}$$

It is worth noting that the scattering vector is depicted in reciprocal space because the wavelength term appears in the denominator, giving **q** a unit of inverse Angstroms [89]. Once measurements have been taken over the desired **q**-range, the 1-D intensity profile can be integrated using the following relationship:

$$I(q) = 4\pi \int_0^{D_{max}} P(r) \frac{\sin(qr)}{qr} dr$$

Here, *I(q)* is the scattering intensity as a function of the scattering vector, *r* is the distance between electron pairs, D_{max} is the maximum interatomic distance within the sample, and *P(r)* represents the pair distribution function of the macromolecule's electrons within real space [89]. Using these equations, a variety of manipulations can be performed on the intensity profile to ascertain size and structural information about the sample [90].

2.3.2 SAXS analysis and applications to proteins and MOFs

In recent decades, improvements on SAXS analysis/processing techniques and increased access to synchrotron-source SAXS setups have allowed greater insights into the structural study of proteins [91]. One of the most common types of structural information gained from SAXS experiments is the radius of gyration (R_g), which mathematically is the root mean square of the distance of a molecule's components from its center of mass. In practical terms, the R_g value is a rough proxy for the size of a protein measured with SAXS, assuming it is monodisperse [92].

Using various analysis methods, the same conclusions can be reached about the size of a studied protein. A widely accepted (but perhaps simpler) method for calculating R_g is the Guinier approximation, which plots the logarithm of scattering intensity versus the square of the scattering vector **q**, often producing a linear relationship whose slope relates to R_g by the following relationship:

$$\ln[I(q)] = \ln[I(0)] - \frac{R_g^2}{3}q^2$$

Although the Guinier approximation has been employed extensively, its key limitation is that it only examines a very small, low-q region of the overall intensity plot [93]. Another approach for calculating the R_g value of a sample involves the pair-density distribution function *P(r)*, which is a probabilistic depiction of interatomic distances within a sample obtained by manipulating the expression for intensity *I(q)*:

$$P(r) = \frac{r^2}{2\pi^2}\int_0^\infty q^2 I(q)\frac{\sin(qr)}{qr}dr$$

Using analysis suites like BioXTAS RAW, a user may calculate R_g by simply inputting the raw SAXS intensity plots as a function of **q** and specifying structural information such as D_{max} [94]. The software then completes the reduction and displays the *P(r)* as well as the calculated R_g value. Resulting shapes of pair-density distribution functions (PDDFs) can then be inspected visually to glean qualitative insights into the shape and structure of the analyzed protein, as depicted in Figure 2.2 below [95].

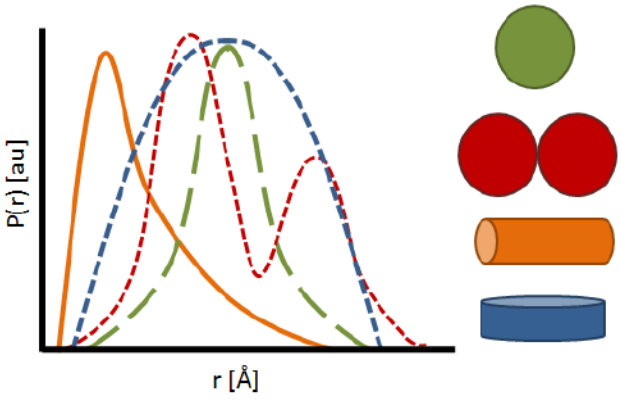

Figure 2.2: Pair-density distribution function (PDDF) examples and associated protein geometries. Adapted from the work of Nyman *et al.* [95].

The last relevant method to the analysis performed in CHAPTER 4 is the Kratky plot, a manipulation performed on the raw SAXS spectra by plotting the product of *I(q)* and $\mathbf{q}^2$ against **q**. Shown in Figure 2.3, this approach reveals information about the folding behavior of a protein in solution, yet another qualitative analysis method that can be linked to quantitative experimental parameters such as temperature or R_g [96].

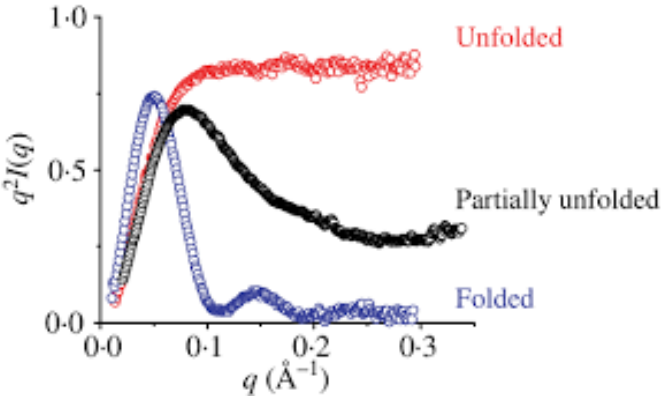

Figure 2.3: Example Kratky plot obtained by plotting $q^2I(q)$ versus the scattering vector q. Adapted from the work of Putnam *et al.* [96].

By combining the qualitative and quantitative information gained by performing the PDDF and Kratky analyses, novel insights on the structure and conformation of protein solutions can be generated. Furthermore, *in situ* SAXS setups allow real-time analysis of structural changes upon chemical addition or thermal exposure [97, 98].

In the last decade, SAXS has also been applied to MOFs in order to characterize pore shape and size (among other structural factors) [99]. By performing experiments while studying the sample with *in situ* SAXS, groups have also been able to track the nucleation and growth of MOF crystals in solution [100]. Past applications of this technique to pure MOFs, some groups have also measured intensity spectra of protein-MOF biocomposites in an attempt to elucidate structural information about encapsulated guests [66, 101].

2.4 Other relevant experimental techniques

Due to the highly interdisciplinary nature of this body of work, several material and protein characterization experiments were conducted to confirm guest encapsulation and release from the framework as well as immunogenic activity retained. These techniques and their relevance to this work are described in the below section.

2.4.1 X-ray diffraction

Powder x-ray diffraction (pXRD) is a constructive scattering technique used to characterize crystalline structures [102]. Because this method is often used to analyze highly ordered materials, the scattering is more accurately considered to be diffraction; therefore, Bragg's law can be used to calculate material parameters such as *d*, the interplanar spacing through the following equation:

$$n\lambda = 2dsin\theta$$

In this relationship, *n* is a scalar integer and λ is the x-ray wavelength. A typical XRD experiment involves preparing the sample as powder and exposing it to monochromatic x-rays at a wide range of angles (typically 5° to 70°). This approach contrasts starkly with SAXS, which only measures scattering at angles lower than 5°.The intensity of the reflected radiation is measured as a function of the angle 2θ and plotted as a diffractogram. The locations and relative sizes of peaks are then compared to databases containing known materials to confirm if the desired materials and crystalline phase were obtained [103]. After confirming the phase, various analysis methods like the Scherrer equation (often used to determine crystallite size) can be used to complement findings

gleaned from observations on particle size from microscopy [104]. In our experiments, pXRD was used to confirm that the crystalline structure of pure MOFs was unmodified by encapsulated of proteins within the framework.

2.4.2 Fourier-transform infrared spectroscopy

Fourier-transform infrared spectroscopy (FTIR) is a non-destructive spectroscopic method used to measure vibrations within molecules, affording insights into the chemical moieties present within a sample [105]. This robust technique can be used to analyze liquid and solid samples based on the selected mode. Most relevant to molecules with asymmetric vibrations, FTIR is used to detect the presence of functional groups (*e.g.*, amides) that have known peaks in the FTIR spectra. In a typical experiment, the prepared sample is exposed to IR radiation, and a detector is used to measure aberrations from the incident beam caused by vibrational modes such as bending and stretching. The absorbance is then plotted as a function of the wavenumber, the reciprocal of wavelength, which serves as a proxy for the wave's energy.

FTIR has been extensively used to study proteins—in particular, their secondary structure [106]. Of specific interest to our studies is the attenuated total reflection (ATR) mode, which allows measurement of solid samples. In CHAPTER 3, ATR-FTIR is used to confirm the encapsulation of proteins within the MOF structure, as the vaccine-MOF biocomposite contains proteinaceous FTIR peaks that are absent in the spectra of the pure MOF. This approach of providing guest incorporation into MOF structures is common in literature [66].

2.4.3 Scanning electron-microscopy

Another indispensable technique used in our work is scanning electron microscopy (SEM), which allows magnifications of up to 130,000x. Viewing samples under SEM can be used to characterize material surfaces, visually inspect representative crystallite size, and confirm findings from other experimental techniques [107]. This method is employed by first passing a primary electron beam through the sample; based on the type of SEM, the secondary and/or backscattered electrons are measured by dedicated detectors. This information is then processed to create a 2-D image of the sample. Because small gas molecules in the air can cause significant deviations in electron scattering, SEM is typically conducted in high vacuum environments, introducing complications for measuring delicate samples [108].

Because SEM relies on the scattering of electrons from the sample, non-conductive materials may require additional preparation before imaging. For non-conductive samples, a common approach to aid visualization with SEM is gold-sputtering, which coats the sample surface with gold particles, thus increasing image quality [109]. In our work the biocomposites were subject to gold-sputtering before imaging as the ZIF species studied was non-conductive. In CHAPTER 3, SEM was used to observe the presence of certain crystallite geometries expected from vaccine-ZIF composites and to validate the efficacy of the rigorous crystallite surface washing protocol.

2.4.4 Confocal laser-scanning microscopy

Confocal laser-scanning microscopy (CLSM) provides several advantages, namely that the out-of-focus light which normally blurs light microscopy images is rejected from the detector, improving resolution in thick samples [110]. Confocal microscopy also

possesses the advantage of allowing imaging "through" samples, whereas a method like SEM only affords surface visualization. Thus, CLSM has found significant applications in the biosciences, where the bulks of tissues and other biological materials must be analyzed rather than just the surface [111].

A useful analysis method in confocal microscopy is the "Z-stack," a process by which a 3-D reconstruction of the sample is created by stacking several images at various depths. By fixing the x- and y- directions of the sample, a confocal user may generate a Z-stack by collecting a series of images at various depths (*i.e.*, multiple focal planes) and then processing these images in a software program [112]. This approach was of particular interest to the work done in CHAPTER 3, as we wanted to confirm that encapsulated guests are randomly distributed through the MOF structure as opposed to localized on the surface or core. Previous groups have employed this approach to similarly confirm the distribution of encapsulated guests [69].

2.4.5 Differential scanning fluorimetry

Above a certain temperature, proteins unfold and aggregate irreversibly in solution; this point is sometime referred to as the "melting point" of a solubilized protein, and can be measured with differential scanning fluorimetry (DSF). The melting temperature (T_m) of a protein is the point at which 50% of the protein is folded and 50% is unfolded [113]. In a DSF experiment, the protein of interest is prepared in a capillary tube and exposed to increasingly high temperatures at a constant ramp rate. The intrinsic fluorescence of tryptophan residues is then exploited to quantify the degree of unfolding. For a normally folded protein, the intrinsic fluorescence of tryptophan is at 330 nm, but as the protein

denatures, this fluorescence shifts up to 350 nm [114]. Thus, as the protein unfolds due to thermal exposure, the fluorescence ratio of the redshifted tryptophan (350 nm) to its native state (330 nm) increases. The inflection point of this fluorescence ratio plotted against temperature is then taken to be the T_m value for that sample.

In our work, DSF was employed to inform the accelerated stability studies undertaken in CHAPTER 3. By performing melting point measurements on a solution of tetanus toxoid vaccine, we were able to select temperatures for the accelerated study that fell below its melting point. Assuming the denaturation of tetanus toxoid followed a similar pathway at all temperatures below T_m, we could then be able abstract the degradation data to lower temperatures through the Arrhenius relationship.

2.4.6 *Enzyme-linked immunosorbent assay*

The experimental method we used to quantify protein stability after encapsulation and release from the MOF structure was an enzyme-linked immunosorbent assay (ELISA). Broadly, ELISA capitalizes on the interaction between antigens and antibodies [115]. The quantity of these interactions can then be compared to a dilution series of known concentration to calculate activity within the sample, typically by colorimetric methods. In this approach, the ability of an antigen to bind to an antibody (or vice-versa) is interpreted as a proxy for immunogenicity, since the method provides confirmation that domains necessary for antigen-antibody interactions are preserved. There are many different forms of ELISA including direct, indirect, sandwich, and competitive [116]. The most relevant to our studies is indirect, competitive ELISA.

In a typical indirect competitive ELISA experiment, samples and standards are first allowed to interact (*i.e.*, compete) with the corresponding antibody. In this step, a sample with high protein activity will bind to the HRP-tagged Anti-tetanus toxoid antibodies, while samples with low activity will not interact. This mixture is then added to plate wells coated with the antigen—in our case, tetanus toxoid. Because we used an indirect assay, low-activity samples will show more color after the substrate is added since the HRP-tagged antibodies did not interact during the competitive step, instead interacting significantly with the plate-bound antigens. Conversely, a sample with high activity will bind all the fluorescent antibodies during the competition step, causing little interaction (and therefore, color) between the antibodies and plate-bound antigen. ELISA was the primary driver of the stability studies conducted in CHAPTER 3.

CHAPTER 3. THERMOSTABILITY AND IMMUNOGENICITY OF TETANUS VACCINE ENCAPSULATED IN A METAL-ORGANIC FRAMEWORK

3.1 Abstract

In developing nations, tropical climates and inconsistent access to electricity render vaccine transport and storage (especially by refrigeration) inefficient due to temperature-induced activity losses. Indeed, failures in this "cold chain" irreversibly damage up to 50% of all vaccines annually. In this work, we thermostabilized Tetanus Toxoid vaccine by encapsulation within zeolitic imidazolate framework-8 and studied its robustness in a variety of harsh storage conditions. Accelerated stability studies at two temperatures suggested that the dried vaccine-ZIF biocomposites retain Tetanus immunogenicity for several months at room temperature. In liquid formulations, suspending the biocomposite in a non-aqueous solvent allowed nearly full stability retention for three months at 40°C, indicating that the ZIF's tendency to degrade in the presence of water is a key factor governing the long-term thermostability of these materials. Additionally, we evaluated the vaccine-ZIF composite's immunological activity with an *in vivo* mouse model, demonstrating that Tetanus encapsulation and release from the framework did not significantly hinder vaccine immunogenicity. Our studies show that encapsulating vaccines within ZIFs may offer a simple, abstractable solution for long-term vaccine storage in harsh conditions, especially in developing nations.

3.2 Introduction

Immunization campaigns in developing nations are known to markedly improve financial, social, and health outcomes [117, 118]. While global vaccination rates for DPT, Polio, and Measles have reached 80 – 90% in the last three decades, there were still 25 million unvaccinated or partially-vaccinated infants in 2021 [4, 32]. The majority of these children live in regions of Africa and Asia, where harsh climates and unreliable electricity sources render long-term vaccine storage (especially by refrigeration) ineffective [119]. Because many vaccines are temperature-sensitive they must often be stored at 4 – 8°C, and short lapses in this refrigeration can cause irreversible damage [5]. Several million doses are lost to failures in this "cold chain" annually, with the World Health Organization estimating that 50% of all vaccines are wasted globally [6, 120].

Lyophilization (freeze-drying) is the most conventional approach for stabilizing temperature-sensitive vaccines [40, 121]. While this method has been studied extensively, there are several drawbacks including high cost, a necessary reconstitution step, and loss of activity upon reconstitution [122-124]. The addition of excipients is another common method for improving vaccine stability, but these components must be carefully screened and tailored for each specific application, which is often cumbersome [125, 126]. In recent years, stabilizing vaccines with polymers matrices, especially in microneedle patches, has emerged as another solution to the cold chain problem [47, 127]. Although microneedles afford remarkable thermostability and remove the necessity for reconstitution before administration, this approach also requires screening excipient combinations and often employs lyophilization during formulation [127, 128]. Moreover, producing polymer

microneedle patches at scale presents non-trivial engineering and logistical challenges [129].

A new approach seeking to avoid the issues surrounding current vaccine stabilization methods employs metal-organic frameworks (MOFs), a class of highly tunable porous materials composed of metal nodes and ligand linkers [53, 130]. Through a self-assembly process called biomimetic mineralization, a variety of proteins, viruses, and cells may be encapsulated within the rigid framework, imparting significant chemical and (most pertinently) thermostability to the entrapped guest [66, 68, 73]. Because many MOFs lack water stability, require harsh synthesis conditions, or are composed of hazardous metals and/or ligands, there are several barriers to safe *in vivo* applications [54, 131, 132]. Consequently, one particular MOF species named zeolitic imidazolate framework-8 (ZIF-8) has emerged as the focus of most biological MOF encapsulation studies [133, 134]. ZIF-8 has drawn significant interest for biomacromolecule stabilization because it can be synthesized under aqueous room temperature conditions, possesses water stability on the order of days, and is composed of the relatively bio-safe Zinc (II) metal center and 2-methyl imidazole ligand [75, 135-138].

While several groups have applied the biomimetic mineralization of ZIF-8 around various biomacromolecules to improve stability, most studies focus on model proteins, viruses, and vaccines such as bovine serum albumin (BSA), tobacco mosaic virus (TMV), or ovalbumin (OVA) [139-142]. Consequently, there is a lack of studies pertaining to vaccine guests with high translational value. Additionally, though many studies have shown the impressive stability enabled by ZIF-8 encapsulation, the vast majority focus on timescales of days, leaving the question of long-term ZIF-8 biocomposite stability

unanswered [82, 137]. A recent study by Singh *et al.* sought to address both of these gaps by encapsulating a lyophilized live viral vaccine (Newcastle Disease Virus) within ZIF-8, demonstrating their formulation retained ~50% viral stability at 37°C for three months [143]. Although this work represents an important step forward in understanding the thermostability limits of MOF-encapsulated vaccines, the authors employed both freeze-drying and excipient addition in their formulation, leaving the long-term stability of as-synthesized MOF biocomposites in question. Furthermore, this study did not examine composite stability in the liquid state, nor did it measure *in vivo* responses to the formulation.

Our study was designed to test the upper thermostability limits of TT@ZIF, a biocomposite created by encapsulating Tetanus Toxoid vaccine in ZIF-8. Spectroscopic, crystallographic, and microscopic techniques were used to first confirm the encapsulation of TT within the framework and the resulting composite material. Accelerated stability studies were then conducted at 40°C and 60°C on dried TT@ZIF powder as well as two different liquid suspensions for 3 months. We also examined biocomposite thermostability over several freeze/thaw cycles and at an extreme temperature of 120°C. After determining retained TT stability with an enzyme immunoassay, we validated the immunogenicity of encapsulated/released TT through an *in vivo* mouse model and predicted shelf-life using the Arrhenius relationship. The overall goal of this work was to characterize the long-term thermostability of a clinically relevant vaccine-MOF composite in a variety of harsh storage conditions, ultimately validating vaccine-ZIF materials as a viable approach for breaking the cold chain.

3.3 Materials and methods

3.3.1 Materials

Tetanus Toxoid (formalin-inactivated) vaccine (Serum Institute of India, Pune, India), 100x Anti-Tetanus Toxoid HRP conjugate Antibody (Alpha Diagnostic International, San Antonio, TX, USA), KPL SureBlue TMB Microwell Substrate (Seracare, Milford, MA, USA), KPL TMB BlueSTOP (Seracare), Zinc (II) Acetate Dihydrate (≥ 98%, Sigma-Aldrich, St. Louis, MO, USA), Zinc (II) Nitrate Hexahydrate (98%, Sigma-Aldrich), 2-methyl imidazole (≥ 98%, TCI, Tokyo, Japan), Triethylamine (98%, Sigma-Aldrich), Propylene Glycol (>99%, Sigma-Aldrich), Ethanol (90%, Sigma-Aldrich), 10x Phosphate-Buffered Saline (>99%, Growcells, Irvine, CA, USA), Ethylenedinitrilotetraacetic acid (99%, Sigma-Aldrich), Immersol (Carl Zeiss, Oberkochen, Germany), Drierite (Lab grade, Alfa Aesar, Haverhill, MA, USA). Deionized (DI) water was supplied by an in-house system (Thermo Fisher, Waltham, MA, USA). Tycho NT.6 Capillaries (NanoTemper Technologies, München, Germany) were used for differential scanning fluorimetry experiments.

3.3.2 Synthesis of MOF and biocomposite

3.3.2.1 Room-temperature synthesis of ZIF-8

Synthesis procedure was followed from the work of Gross *et al.* [136]. ZIF-8 structures with a 1:16:16 ratio of Metal : Ligand : TEA were prepared by first dissolving 0.733 g zinc (II) nitrate (2.46 mmol) in 50 mL DI water. Then, a solution of 3.244 g HMe-Im (39.5 mmol) and 4.00 g TEA (39.52 mmol) in 50 mL DI water was stirred until dissolved. The zinc salt solution was added to the HMe-Im/TEA solution, and the resulting mixture was stirred for 10 min. This mixture was then separated via centrifugation (3.0

RCF, 10 min), decanted, and suspended in DI water for 12 h. This centrifugation process was repeated for a second water wash, and after 12 h, the ZIF suspension was centrifuged again, and the solid was collected. Solid ZIF crystals were finally dried in vacuum for 2 h at 150℃.

3.3.2.2 Room-temperature synthesis of TT@ZIF-8

Synthesis procedure was adapted from the work of Liang *et al.* [66]. TT@ZIF structures were synthesized by preparing 20 mL each of a 160 mmol ligand solution of 2-methyl imidazole (HMe-Im), and a 40 mmol solution of zinc (II) acetate. 1 mL of the TT vaccine stock (3,480 Lf or roughly 10mg) was added to the HMe-Im solution a few minutes before addition of the zinc solution. Upon addition of the metal, solid crystallites appeared instantly and were agitated for 1 minute; the combined solution was then left overnight. The same procedure was followed to synthesize fluorescent-TT@ZIF (fTT@ZIF). Resulting biocomposite crystals were separated from solution by centrifugation (3.0 RCF, 10 minutes) and then washed, sonicated, and centrifuged twice each with water and ethanol. The resulting pellet was dried at ambient conditions for 1-2 days before massing; the average yield was ~80 mg of TT@ZIF.

3.3.3 Assessment of biocomposite structure

3.3.3.1 Confirming crystallinity with powder x-ray diffraction (pXRD)

MOF crystal structure was confirmed with pXRD. Measurements were performed on the XPert Pro Alpha-1 diffractometer with X'Celerator detector using Cu $K\alpha_1$ radiation (λ=1.540598 Å) (Malvern Panalytical, Malvern, United Kingdom). A 2θ range of 5° to 70°

was measured using a step size of 0.0167° 2θ and a time per step of 10.16 seconds. Scherrer analysis of crystal size was conducted in the HighScore Plus program (Malvern Panalytical).

3.3.3.2 Assessing of TT incorporation with Fourier-transform infrared spectroscopy (FTIR)

FTIR measurements were done on a Nicolet iS10 FTIR spectrometer with the Smart iTX diamond attenuated total reflection (ATR) accessory (Thermo Fisher). Pure MOFs, biocomposites, and lyophilized proteins were all analyzed as dry powders. We performed 64 scans with a resolution of 2 cm^{-1}.

3.3.3.3 Visualizing of crystallite surface with scanning electron microscopy (SEM)

Since the zinc-based ZIF is non-conductive, all samples were prepared by gold sputtering (Hummer 6 sputterer, Ladd Research, Williston, VT) for 3-4 minutes before visualization by scanning electron microscopy (SU8230, Hitachi, Tokyo, Japan). Samples were observed at magnifications ranging from 5,000x to 50,000x zoom at voltages ranging from 5.0 kV to 10.0 kV, and with a working distance of 9060.61 µm.

3.3.3.4 Visualizing of TT distribution within ZIF structure with confocal microscopy

1 mL of TT stock was first tagged following the protocol of the Alexa Fluor 488 protein labeling kit (Thermo Fisher) [144]. After synthesizing fTT@ZIF (see section 3.3.2), the powder was prepared for confocal imaging by suspension in Immersol. Confocal images were taken on a Zeiss LSM 700 (Carl Zeiss) with an objective lens of 63x. For z-stacked images, an interval of 0.200 µm was used for appropriate resolution imaging of ~1 µm

fTT@ZIF crystallites. Image processing and analysis was conducted in ZEN lite (Carl Zeiss).

3.3.4 Measuring melting point of Tetanus Toxoid vaccine

The melting temperature (T_m) of the stock Tetanus Toxoid was measured with differential scanning fluorimetry (DSF) on a Prometheus NT.48 (NanoTemper Technologies). The stock vaccine solution was diluted to a concentration of 10 µM before measurement, and a ramp rate of 1°C/min was used over a temperature range of 20°C to 90°C. Samples were measured in triplicate to confirm the T_m value.

3.3.5 Preparation of biocomposites and Tetanus Toxoid for stability studies

3.3.5.1 Dried and suspended biocomposite samples

Dried TT@ZIF-8 was packaged in glass vials in ambient conditions before sealing the vials in aluminum pouches containing color-indicating Drierite. Upon removal of vials from pouches, the Drierite mostly retained its blue color, suggesting the lack of significant moisture. Suspensions of TT@ZIF were prepared at a concentration of 1 mg/mL in two solvents: water and a 4:1 mixture of propylene glycol (PG) and ethanol (Et). After packaging, liquid samples were placed in a sand bath during thermal exposure to mitigate temperature fluctuations.

3.3.5.2 Freeze/thaw samples

A 0.5 mg/mL suspension of TT@ZIF in water was stored in a -80°C freezer for 20 min before removal and placement in a room-temperature water bath for 15 minutes. This process was cycled up to 5 times before measuring stability with ELISA.

3.3.5.3 Tetanus Toxoid

For liquid-phase accelerated aging experiments, the TT stock was diluted to 1 µg/mL and aliquoted in glass vials. The exact composition of the stock solution was measured in a previous study from our group [145]. For solid-phase aging experiments, the TT stock was first diluted to 1 mg/mL before placing in a -80°C freezer. The frozen vaccine was then lyophilized in a Freeze Drying System (Labconco, Kansas City, MO) with a vacuum of 0.700 mbar.

3.3.6 Measurement of encapsulated/released TT concentration

3.3.6.1 Dissolution of ZIF structure

After exposure to high temperature for the desired time, ZIF structures were exfoliated using a procedure adapted from Li *et al.* [146]. A 0.1 M solution of EDTA (pH 6.9 – 7.0) was added to the TT@ZIF powder in an approximate molar ratio of 3:2 EDTA:TT@ZIF. Practically, this amounted to adding 62 µL of the EDTA solution per 1 mg of TT@ZIF powder. EDTA was added directly to liquid suspensions, and solid samples were solvated in water at a concentration of 1 mg/mL before immediate addition of EDTA. Samples were left to exfoliate for 24 hours before measuring retained Tetanus activity.

3.3.6.2 Quantifying Tetanus Toxoid activity

Activity of TT was measured with direct, competitive Enzyme-linked immunosorbent assay (ELISA). After coating plates with TT antigen, exfoliated samples and standards were diluted to the appropriate concentration range (30 – 2000 ng/mL). These samples were then mixed in an equal ratio with Anti-TT HRP Antibody and incubated at 37°C for 1 hour. After adding the sample-antibody mixtures, the plate was incubated overnight at 4°C. After addition of TMB substrate and stop solution, concentrations were measured with an iMark Microplate Absorbance Reader (Bio-Rad, Hercules, CA, USA) at a wavelength of 620 nm.

3.3.6.3 Calculating encapsulation/release efficiency of TT within ZIF-8

Using ELISA, the concentration of unencapsulated TT was measured by collecting the supernatant for each wash cycle on the freshly-prepared crystallites. These values were then examined alongside the amount of TT released from the ZIF after exfoliation to close the following mass balance:

$$TT_{total} = TT_{[H_2O\ washes]} + TT_{[EtOH\ washes]} + TT_{[surface]} + TT_{[encapsulated]}$$

3.3.7 *Arrhenius modelling to predict shelf-life*

Linear regressions were first performed on the data presented in Figure 4.5, accounting for errors in stability measurements. These fits allowed forecasting of the days to failure, defined as losing 20% stability. The number of days to failure (a proxy for the reaction rate) at 40˚C and 60˚C were used to generate an Arrhenius relationship, which was then used to predict stabilities at lower temperatures.

Error was propagated through two functions—the linear regression and the Arrhenius fit. Variance in calculations for days to failure was generated by creating several linear fits for the data (based on the errors in the stability measurements) and analyzing the statistical distribution. The corresponding days to failure from these various fits were then fed into a variety of possible Arrhenius equations (which varied based on the initial input of days to failure at 40˚C and 60˚C). We then reported the means and standard deviations of the outputs of the Arrhenius model. In this way, the error of the stability measurements was propagated throughout both calculations.

3.3.8 In vivo procedures

3.3.8.1 Animals

Female and male BALB/c mice were housed in a biosafety level 1 (BSL-1) facility at the Physiological Research Lab (PRL) at Georgia Tech. IACUC and PRL regulations were followed during all experimental protocols to maximize experimenter and animal safety [147]. Each of the five experimental groups contained $n = 5$ individual mice.

3.3.8.2 Immunizations, blood collection, and quantification of serum antibody levels

All TT@ZIF and control injections were completed intramuscularly with a dose of 5 μg TT and an injection volume of 100 μL. Because all but one experimental group was suspended in a 4:1 mixture of PG:Et, we first ensured that this injection volume was suitable for animal safety according to previous studies [148]. Post-injection, blood was drawn by tail vein laceration every 2 weeks for 4 weeks before measuring serum antibody levels of anti-TT IgG with ELISA.

3.4 Results and Discussion

3.4.1 Characterizing TT@ZIF biocomposite structure

Because we are the first group to report Tetanus Toxoid (TT) encapsulation within MOFs, biocomposites were first characterized with pXRD and FTIR to confirm the material structure and presence of TT within the ZIF scaffold (Figure 3.1).

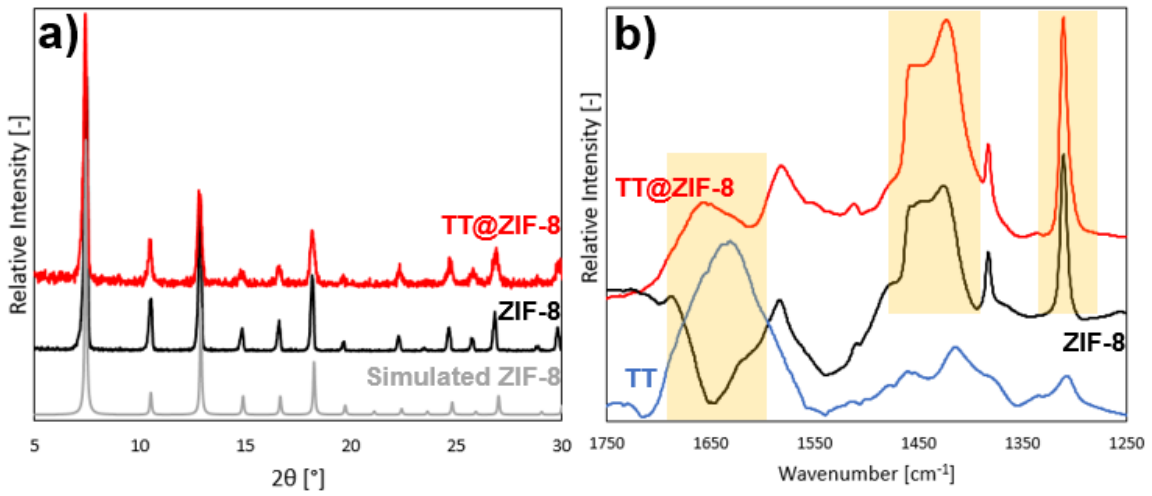

Figure 3.1: Crystallographic and spectroscopic characterization of TT@ZIF biocomposite, pure ZIF, and lyophilized TT. Representative pXRD spectra of (a) TT@ZIF biocomposite (red), pure ZIF-8 structure (black), and simulated ZIF-8 structure (gray). Representative FTIR spectra of (b) TT@ZIF biocomposite (red), pure ZIF-8 structure (black), and lyophilized TT vaccine (blue).

Diffractograms shown in (Figure 3.1a) show that the synthesized ZIF-8 structure is in excellent agreement with previously simulated crystallographic data for the ZIF-8 sodalite topology [74]. The presence of sharp peaks at 2θ values of 7.50°, 10.5°, and 13.0° suggest that the pure ZIF was successfully synthesized. The biocomposite diffractogram also matched the peak locations and relative intensities shown in previous studies, but clearly has a lower signal-to-noise ratio likely owed to disruption of the ZIF's long range

order by the large (150 kDa) TT molecules embedded within the framework. Despite this difference, we concluded these pXRD results demonstrate that encapsulating TT within ZIF-8 did not significantly alter the crystalline structure of the framework.

After confirming the crystallinity of TT@ZIF, the chemical effects of TT incorporation into the framework were studied using attenuated total reflection FTIR (Figure 3.1b). The lyophilized TT vaccine contained one especially relevant feature in the studied wavenumber range: a broad Amide I peak from 1700 – 1550 cm^{-1} owed to interactions between acyl groups (R—C=O) and nitrogen atoms [149]. The lyophilized TT spectrogram also contained a much smaller peak in the Amide III region (1350 – 1250 cm^{-1}), which is in firm agreement with a previous study on lyophilized Tetanus vaccine [123, 150]. The prominent Amide I peak observed in TT is notably missing from the pure ZIF spectrogram since the MOF is composed only of zinc metal centers and HMe-Im ligands. While ZIF-8 did show a sharp peak at 1310 cm^{-1} appearing to match the protein, this is not owed to any proteinaceous behavior, rather the C—N stretching mode from the aromatic amine structure of the HMe-Im ligand. The primary characteristic feature of ZIF-8, however, was the plateau ranging from 1460 – 1390 cm^{-1} caused by C—H bending from the ligand, which was absent from the TT curve. There appears to be a negative peak in the ZIF-8 spectra centered at 1650 cm^{-1}, however this is likely an artefact of background subtraction as previous literature reports do not show this behavior [66]. As expected, the TT@ZIF spectrogram contained both the Amide I peak from the proteinaceous guest as well as the characteristic ZIF-8 plateau and strong C—N stretching peak. The Amide I peak shifted upwards slightly in the biocomposite, possibly due to changes in the local environment; this would further support the hypothesis that the guest is predominantly

encapsulated within the structure as opposed to being surface bound. It is also possible that this apparent peak shift is simply an additive effect of the "negative" 1650 cm^{-1} peak seen in ZIF-8 and the pure TT Amide I peak. Thus, further FTIR background analysis is necessary to strongly conclude whether TT incorporation into the MOF structure results in genuine peak shifts owed to local environment differences. All peaks and resulting analyses for the ZIF and protein-ZIF composite agreed with previous similar studies on other encapsulated guests such as BSA and glucose oxidase [66, 151].

3.4.2 Visualizing TT@ZIF biocomposites

Microscopy studies were also conducted on the biocomposites in order to assess distribution of Tetanus within the ZIF structure as well as average crystallite size (Figure 3.2).

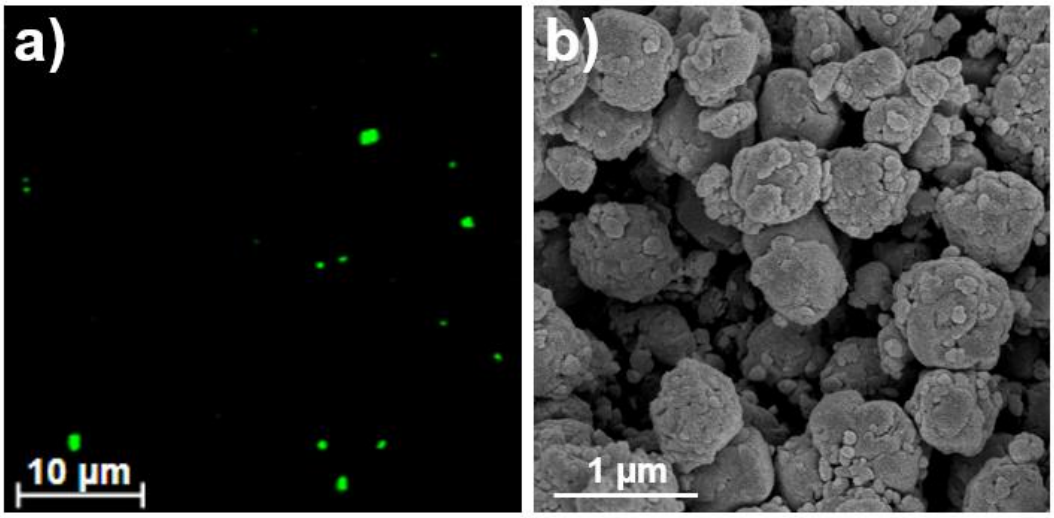

Figure 3.2: Representative microscopy images of TT@ZIF biocomposite: (a) confocal microscopy for fluorescent-TT@ZIF with 63x objective lens and (b) SEM of as-synthesized TT@ZIF under 25,000x magnification.

Although the FTIR results provided strong evidence of encapsulation due to a rigorous surface wash procedure and the Amide I peak observed in the biocomposite, visualization of the fluorescently-tagged biocomposite (fTT@ZIF-8) with confocal microscopy confirmed that TT is randomly distributed throughout the ZIF crystallites instead of localized on the surface or core. Each green dot in Figure 3.2a represented a single crystallite or aggregate, depending on its size. The size of a single crystallite appeared by visual inspection to be consistent with the higher-resolution images generated from SEM experiments. Collecting a Z-stack image of the fluorescent crystallites (Figures A.1.1, A.1.2) further underscored that Tetanus molecules were present throughout the biocomposite structure. This finding is consistent with a previous study on fluorescently-tagged proteins encapsulated within ZIF-8 [69].

The SEM image shown in Figure 3.2 depicts a wide range of crystallite sizes with edge lengths ranging from 50 nm to 700 nm. Images taken with several magnifications up to 50,000x (Figure A.1.3) confirm that Figure 3.2b was representative of the biocomposite. Notably, the TT@ZIF crystallites did not appear to assume the sharp, rhombic dodecahedra geometry often associated with ZIF-8 biocomposites [66, 69, 152]. When BSA@ZIF was synthesized under the exact same conditions as TT@ZIF, the crystallite shapes appeared significantly more regular (Figure A.1.4). Smaller, intergrown crystals appear on the surface of the TT@ZIF crystallites more frequently than they did for BSA@ZIF, causing a wider size distribution. This is possibly explained by the mechanism of ZIF biomimetic mineralization, which is driven by certain acidic amino acid residues on the protein surface aiding nucleation of framework growth around the guest the [153]. Thus, vast differences between TT (150 kDa) and BSA (66 kDa) sizes and primary structures could explain the

variation in crystallite growth/geometry. Previous reports on ZIF biocomposites have shown a wide variety of crystallite geometries dependent on the guest identity [66, 151]. Further SEM studies on TT@ZIF, especially those that rigorously quantify particle size distribution, would be necessary to conclude whether the large, 500 – 700 nm crystallites seen in Figure 3.2b are aggregates or primary particles.

3.4.3 Quantifying TT@ZIF stability in harsh storage conditions

3.4.3.1 Release of TT from ZIF structure

The characterizations reported in sections 3.4.1 and 3.4.2 demonstrate that Tetanus was successfully encapsulated within ZIF-8. Before conducting the thermostability studies, the release of Tetanus from the framework also had to be confirmed. We prepared TT@ZIF at two concentrations in aqueous suspension and measured the TT ELISA response before and after exfoliating the ZIF by addition of an EDTA solution (Figure 3.3).

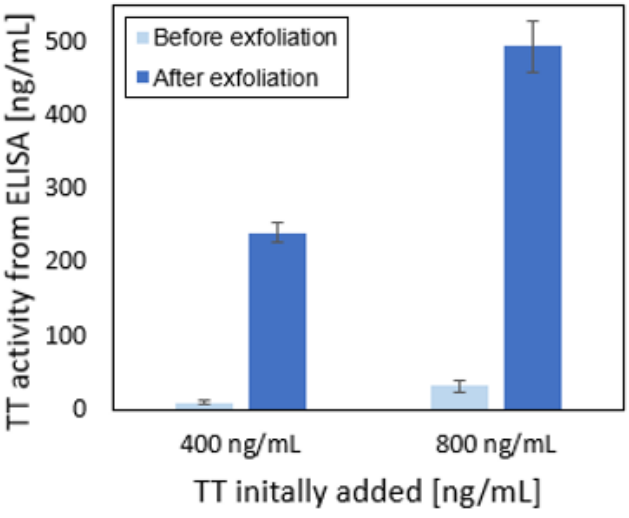

Figure 3.3: Release of Tetanus from two aqueous suspensions of TT@ZIF. Bars depict TT activity before (light blue) and after (dark blue) addition of exfoliating agent to

the same samples, and activity was measured by direct competitive ELISA. Data is shown for *n=3* replicates.

Comparing the measured TT activity before and after exfoliation of the ZIF highlights a dramatic difference. The minimal activity shown for non-exfoliated samples is likely due to residual TT on the crystallite surface not removed during the washing steps. The release efficiency can be calculated from Figure 3.3, and is approximately 60%; this result is also consistent with previous exfoliation studies that measured release efficiencies of 60 – 70% [137].

The encapsulation efficiency (and thus, the mass percent of TT in TT@ZIF) was quantified by subtracting amounts of TT in the supernatants from the surface washes and surface bound TT from the initial amount of TT added. When we introduced ~5 mg of TT to the biomimetic mineralization reaction and measured TT concentrations in the washes with ELISA, we found 66 ± 10 µg in the supernatant, 46 ± 0.6 µg in the first water wash, 50 ± 0.7 µg in the second water wash, 158 ± 19 µg in the first ethanol wash, and 358 ± 5 µg in the second ethanol wash: this totals to 680 µg TT. From Figure 3.3, 5 – 10% of the TT not removed in the surface wash remains bound to the surface of the crystallites. Adding this value (324 ± 153 µg) to the TT removed during surface washing suggested that approximately 1 mg was not incorporated into TT@ZIF biocomposite. Because the reaction yield was ~40 mg and approximately 4 mg TT was successfully encapsulated, we concluded that TT@ZIF is roughly 10% TT by mass.

3.4.3.2 Accelerated stability studies for TT@ZIF

We assessed the long-term stability (and thus, the shelf-life) of TT@ZIF composites at elevated temperatures of 40°C and 60°C. These temperatures were selected

to be consistent with widely accepted accelerated study conditions while exploiting the high-temperature stability of ZIF-8 [154, 155]. Both of these elevated temperatures also fall below the melting point (T_m = 68.6°C) of Tetanus Toxoid as measured by DSF—a result in agreement with a previous study (Figure A.1.5) [156]. This design enables extrapolation of stability data to lower temperatures *via* the Arrhenius relationship [157].

Samples were packaged both as dry powders and in two different liquid suspensions: water and a 4:1 mixture of propylene glycol and ethanol. The non-aqueous solvent was selected on the basis of biosafety, ZIF stability in the solvent, appropriate density for crystallite suspension, and lack of solvent interference with ELISA [74, 148]. The accelerated stability results are shown in Figure 3.4 below, and all raw ELISA data are listed in Appendix Tables A.2.1 – A.2.4.

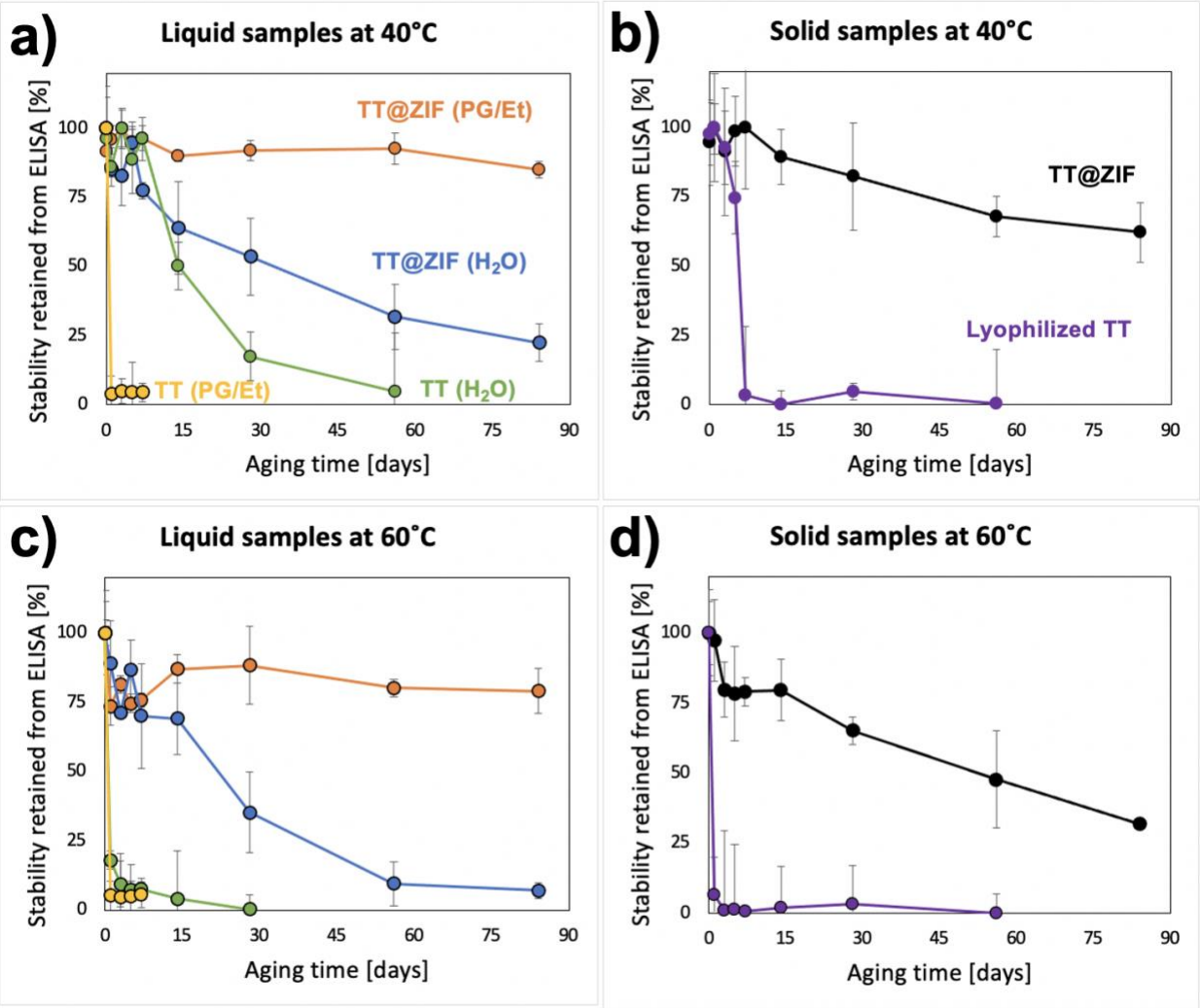

Figure 3.4: Accelerated stability studies for TT@ZIF at two temperatures: (a, b) 40°C and (c, d) 60°C. Curves are shown for TT@ZIF in PG/Et (orange), TT@ZIF in H_2O (blue), TT vaccine in H_2O (green), TT vaccine in PG/Et (yellow), dried TT@ZIF powder (black), and lyophilized TT vaccine (purple). Labels are the same for (a,b) and (c,d). Activity was measured by direct competitive ELISA. Data are shown for *n=3* replicates.

Stability results for TT vaccine in water at are consistent with a previous study that showed full activity loss at 45°C within 6 weeks [158]. At a slightly lower temperature of 40°C (Figure 3.4a), full activity loss occurred after 8 weeks. At a higher temperature of 60°C (Figure 3.4c), the degradation was much more rapid, losing full activity after just 2 weeks. For TT dissolved in the PG/Et solution, complete activity loss occurred after just 1

day at both studied temperatures (Figure 3.4a, 3.4c). Lyophilized TT fully degraded after 1 week at 40°C (Figure 3.4b) and just 2 days at 60°C (Figure 3.4d). Again, this result matches accepted literature reports [159]. Paradoxically, lyophilized TT at 40°C retains stability for significantly less time than TT in water at the same temperature; this is likely due to moisture-induced aggregation for the freeze-dried vaccines. Overall, measured activity losses for TT vaccine controls were in good agreement with existing literature reports.

For liquid formulations, suspending biocomposites in the non-aqueous PG/Et solution afforded the greatest stability retention of all samples studied. After 12 weeks at elevated temperatures, these suspensions retained 85% ± 3% stability at 40°C (Figure 3.4a) and 79% ± 8% stability at 60°C (Figure 3.4c). This approach exploited the much higher relative stability of ZIF-8 in organic solvents (*e.g.,* methanol and DMF) as opposed to water [66, 74, 75]. In contrast, the TT@ZIF samples suspended in water steadily lost activity over the studied period as the ZIF structure was hydrolyzed, causing the release of encapsulated TT into the solvent bulk where it was denatured in days or weeks depending on the temperature. Over the 12-week period, TT@ZIF in water only retained 22% ± 7% activity at 40°C (Figure 3.4a) and 7% ± 3% at 60°C (Figure 3.4b), suggesting that biocomposite suspension in water is not a viable approach for long-term vaccine storage at elevated temperatures.

Notably, the dried biocomposite samples retained less stability than the non-aqueous liquid suspensions at both temperatures. After 12 weeks, dried TT@ZIF powder retained 62% ± 11% (Figure 3.4b) at 40°C and 32% ± 2% at 60°C (Figure 3.4d). While this stabilization represents a marked improvement when compared to the lyophilized

vaccine, it emphasizes the substantial effect of water (even residual moisture) on ZIF-8 degradation. Thus, packaging dried TT@ZIF in a fully inert/dry environment may result in drastically improved biocomposite stability.

We also examined dried TT@ZIF stability at an extreme temperature of 120°C and through 5 freeze/thaw cycles of the aqueous suspension (Figure 3.5). Raw ELISA data is listed in Appendix tables A.2.5 and A.2.6.

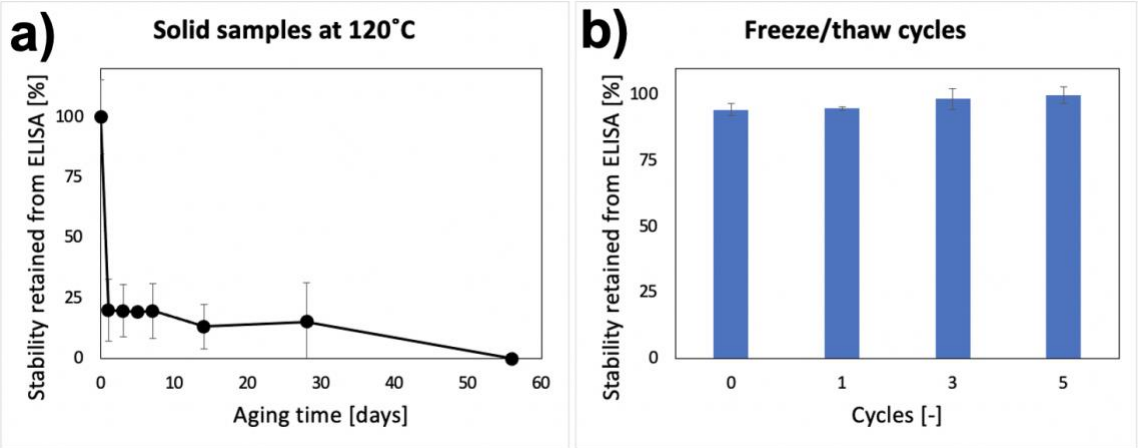

Figure 3.5: TT@ZIF stability in extreme temperatures of (a) 120°C and (b) up to five freeze/thaw cycles. Activity was measured by direct competitive ELISA. Data are shown for *n=3* replicates.

While the biocomposite retained 15% ± 16% stability for 1 month at 120°C (Figure 3.5a), full activity loss was observed within 8 weeks. By this time, the original white TT@ZIF powder had carbonized and turned a blackish brown color, indicating significant chemical changes and degradation of the framework. The rapid initial stability loss seen in Figure 3.5a is not seen in the accelerated stability studies conducted at 40˚C and 60˚C; we speculated that because the 120˚C experiment was far above the melting point of TT, the degradation may have proceeded by another mechanism. TT@ZIF was also suspended in

water and subjected to several freeze/thaw cycles (Figure 3.5b). Full activity was retained after 5 cycles, suggesting that while the aqueous formulation is not ideal for long-term storage at high temperatures, it can retain stability at very low temperatures.

3.4.3.3 Predicting shelf-life of TT@ZIF formulations

Using the Arrhenius relationship, which states that the rate of a reaction is exponentially proportional to its temperature, we extrapolated the accelerated stability data collected at 40°C and 60°C to lower, commonly-used storage temperatures outlined by the International Conference on Harmonization (ICH) [154]. These guidelines suggest several climactic zones with temperatures ranging from 5°C to 30°C, which are meant to mimic real-world storage conditions in the developing world. Alongside stability predictions at the recommended temperatures, we also included the data from our accelerated stability studies (highlighted in orange). The Arrhenius modeling results are summarized in Table 3.1 below.

Table 3.1: Using the Arrhenius equation to calculate period of stability retention (80%) for dried TT@ZIF, TT@ZIF suspended in H_2O, and TT@ZIF suspended in PG/Et. Stabilities (in days) were predicted for four temperatures outlined by the ICH and are reported as means plus standard deviations.

Formulation	Dried TT@ZIF	TT@ZIF (H_2O)	TT@ZIF (PG/Et)
Temperature	80% stability retention (days, mean ± SD)	80% stability retention (days, mean ± SD)	80% stability retention (days, mean ± SD)
5°C	552 ± 214	40 ± 24	1078 ± 815
21°C	148 ± 31	17 ± 5	379 ± 159
25°C	109 ± 19	14 ± 3	302 ± 103
30°C	76 ± 10	11 ± 2	232 ± 57
40°C	38 ± 2	7 ± 1	145 ± 18
60°C	11 ± 1	4 ± 1	125 ± 242

The ICH recommends that vaccine formulations retain 80 – 90% stability for one year at the temperatures reported in Table 3.1. These predictions suggest that neither the dried TT@ZIF nor the aqueous TT@ZIF formulations are suitable for retaining shelf-life on this timescale. The non-aqueous suspension of TT@ZIF, however, would appear to enable one year of acceptable shelf-stability at many of the suggested storage conditions. Thus, we conclude from this analysis that a suspension of TT@ZIF in PG/Et is the only formulation studied in this work to meet industrially accepted standards for long-term vaccine storage, though optimizations on packaging dried TT@ZIF may improve its feasibility.

3.4.4 In vivo responses to TT@ZIF

To further validate the translational feasibility of vaccine-ZIF materials, we conducted a double-blind experiment in BALB/c mice to measure the *in vivo* responses to TT@ZIF biocomposites and various controls. We studied five experimental groups with $n = 5$ individuals each. All groups were injected subcutaneously on day 0, and the anti-TT IgG serum levels were measured by ELISA after 2 and 4 weeks.

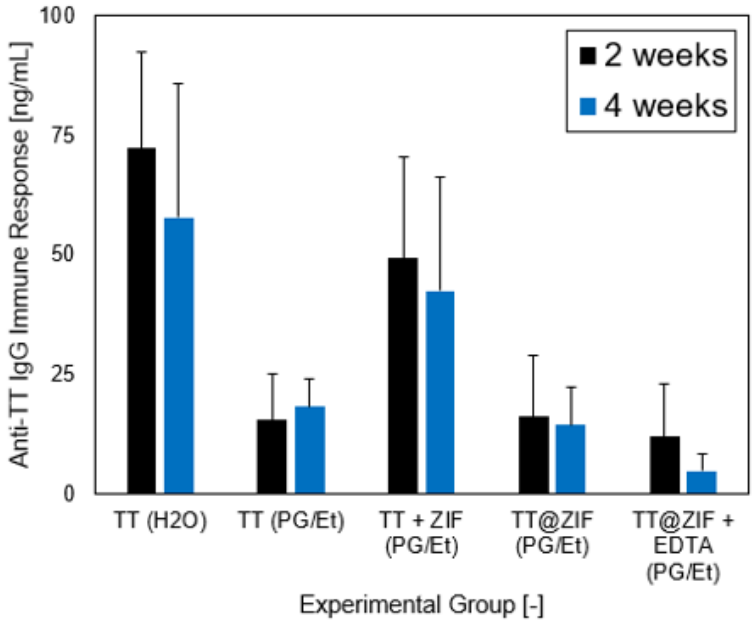

Figure 3.6: Anti-TT serum antibody levels measured with ELISA two and four weeks post-injection subcutaneously. Data are shown for *n=5* mice for each experimental group: (1) TT vaccine in water, (2) TT vaccine in propylene glycol and ethanol (PG/Et) mixture, (3) TT vaccine and pure ZIF mixture in PG/Et, (4) still-encapsulated TT@ZIF in PG/Et, and (5) unencapsulated TT@ZIF + EDTA in PG/Et.

There was a clear negative effect on immune response caused by injecting the tetanus vaccine in the PG/Et solvent versus water, as noted by comparing groups 1 and 2. This may be due to the relatively high viscosity of PG, which possibly interferes with transport processes at the physical administration site. Immune responses were similar for TT, TT@ZIF, and exfoliated TT@ZIF (groups 2, 4, and 5, respectively) all solvated in PG/Et. This observation suggests that exfoliation before vaccine administration may not be necessary, as phagocytosis and uptake by acidic vesicles such as lysosomes may degrade biocomposites and release the guest molecules *in vivo.* Of samples solvated in PG/Et, the highest immune response was seen for a mixture of TT and pure ZIF (group 3). When compared to group 2, this suggests that intact ZIF crystallites (~100 nm) may act as an adjuvant, perhaps increasing rates of cellular uptake. The hypothesized adjuvant effect of

the ZIF seemed to partially counteract the negative effects associated with injecting the PG/Et mixture, seen by comparing groups 1, 2, and 3. The larger TT@ZIF particles (~700 nm) did not appear to benefit from this effect, perhaps suggesting that they were cleared by macrophages before they were able to dissolute, release the encapsulated TT, and cause generation of the desired anti-TT antibodies. When comparing immune responses between 2 and 4 weeks, all studied experimental groups showed similar or lower serum antibody levels at the later time point.

3.5 Conclusions

In this study, Tetanus Toxoid vaccine was encapsulated within the ZIF-8 structure and characterized with various microscopic, crystallographic, and spectroscopic techniques to confirm the presence of TT@ZIF. The vaccine-ZIF composite was then formulated in liquid and solid conditions and exposed to a variety of harsh storage conditions including elevated temperatures and freeze/thaw cycles. These accelerated stability studies were then used to predict shelf-lives at industrially accepted storage temperatures defined by the ICH. Finally, TT@ZIF was introduced to a live animal model to study immunogenic responses *in vivo*. Through these experiments, we built upon previous studies on thermostability of MOFs and further validated this approach's feasibility for long-term storage (months – years) and breaking the cold chain [137, 143].

Characterization of TT@ZIF through pXRD, FTIR, SEM, and confocal microscopy provided strong evidence that TT was encapsulated throughout the ZIF structure. Comparing the diffractograms for ZIF-8 and TT@ZIF (Figure 3.1a) suggested that incorporating TT into the MOF did not significantly alter the pure ZIF structure or

crystallinity. FTIR spectrograms showed that the TT@ZIF biocomposite contained both the characteristic proteinaceous peaks (Amide I and III) seen in TT as well as the characteristic ZIF plateau and peak owed to the methyl group and aromatic amine, respectively, composing the HMe-Im ligand (Figure 3.1b). Fluorescently-tagged TT was encapsulated within the ZIF and examined with confocal microscopy, allowing visual confirmation of TT's random and complete distribution through the biocomposite (Figure 3.2a). Crystallite size (50 – 700 μm) and shape were observed with SEM, where the rhombic dodecahedron shape characteristic of ZIF-8 biocomposites was notably not observed due to the growth of many smaller crystals on surfaces of the largest crystallites (Figure 3.2b). The methods used to confirm guest encapsulation were in strong agreement with previous studies on other biomacromolecule guests [66, 69, 137, 143].

After confirming a TT release efficiency of ~60% from the ZIF with ELISA, biocomposites were subject to accelerated stability studies at 40°C and 60°C for 12 weeks, enabling stability prediction at lower temperatures through the Arrhenius relationship. The best results were obtained by suspending TT@ZIF in a mixture of propylene glycol and ethanol (PG/Et), which afforded remarkable stability retention (85% ± 3% at 40°C and 79% ± 8% at 60°C) after 3 months of thermal exposure (Figures 3.4a, 3.4c). Interestingly, the dried TT@ZIF samples were much less stable than the non-aqueous liquid formulation (32% ± 2% stability retained after 3-month exposure to 60°C, Figure 3.4d), suggesting that even the presence of residual moisture considerably affects dry biocomposite stability. At an extreme temperature of 120°C, TT@ZIF lost full stability within 2 months (Figure 3.5a), yet experienced no stability losses when exposed to 5 freeze/thaw cycles (Figure 3.5b). Extrapolation of these accelerated stability studies *via* the Arrhenius relationship suggested

that TT@ZIF suspended in the non-aqueous PG/Et solvent would meet ICH stability guidelines at temperatures below 25°C, highlighting the translational viability of these biocomposites for long-term vaccine storage.

Finally, the immunogenicity of TT@ZIF was evaluated in a murine model. The *in vivo* data showed that immune responses 4 weeks post-injection were hindered by the PG/Et solvent mixture when compared to the aqueous tetanus vaccine formulation, suggesting that while PG/Et is an excellent solvent for storage, further solvents must be explored before widespread *in vivo* applications. Nonetheless, these data suggested that exfoliation of the ZIF structure is not necessary to produce an immune response, and that intact ZIF crystallites may actually have an adjuvant effect due to their size (100 – 200 nm).

In conclusion, this work further validates the translational value of vaccine-ZIF biocomposites by demonstrating the remarkable long-term thermostability of the clinically relevant Tetanus Toxoid vaccine—especially in a non-aqueous, bio-safe liquid formulation. Strong *in vivo* immune responses to TT@ZIF formulations provided additional confidence that encapsulation and release from the framework did not hinder immunogenicity, and that cellular uptake of MOF particles may actually act as an adjuvant, improving immunogenicity.

CHAPTER 4. INTERROGATING ENCAPSULATED PROTEIN STRUCTURE WITHIN METAL-ORGANIC FRAMEWORKS

4.1 Abstract

Encapsulating biomacromolecules within metal-organic frameworks (MOFs) has been shown to confer significant thermostability to entrapped guests. It has been hypothesized that confinement of guest molecules within a rigid MOF scaffold is responsible for heightened stability, but no direct evidence of this mechanism has been presented. Here, we introduce for the first time small angle x-ray scattering (SAXS) as a novel technique for solving the structure of bovine serum albumin (BSA) while still encapsulated inside two zeolitic imidazolate frameworks (ZIF-67 and ZIF-8). By subtracting the scaled SAXS spectrum of the ZIF from that of the biocomposite BSA@ZIF, we obtained the confirmation and radius of gyration of encapsulated BSA through Guinier, Kratky, and pair distance distribution function analyses. Furthermore, this approach was demonstrated upon a physical mixture of BSA and ZIF, suggesting that successful subtraction is not evidence of encapsulation. We also found that encapsulated BSA retains its size and folded state when exposed to 70°C (a normally denaturing temperature), suggesting entrapment within MOF cavities prevents protein unfolding, and thus denaturation.

4.2 Introduction

Engineering protein stability is an important and persistent challenge in living systems [160]. From engineering enzyme robustness to reducing the rate of cold-chain

failures during vaccine transport, many subfields would benefit from a simple, abstractable platform that renders proteins more stable [161, 162]. Metal-organic frameworks (MOFs)—a class of highly porous materials used for separations, catalysis, and drug delivery applications—may offer one such solution [50-52, 163]. In recent years, MOFs have emerged as a possible solution for enhancing biomacromolecule stability through an encapsulation process known as biomimetic mineralization. With this approach, prior studies have demonstrated the retention of protein and virus stability after exposure to normally denaturing temperatures as high as 80°C [64, 164].

Heightened stability of a guest molecule (*e.g.*, protein) as a result of confinement within a porous host structure has also been observed in other biocomposites such as mesoporous silicas [165, 166]. Notably, due to the size of BSA (~6 nm diameter) and the ZIF pore size (~1 nm diameter), guest encapsulation occurs within larger cavities formed by MOF growth around the guest, not confinement within a single MOF pore [66]. For both MOFs and silicas, quantifying guest structure—while still encapsulated—would be advantageous, as this may impart clarity on the (still unconfirmed) mechanism of stability [164]. However, there have been no such reports in the literature, likely because biocomposite guest stability is conventionally measured upon guest release from the porous framework (*e.g.*, through exfoliation by ionic buffers, acids, and/or chelating agents) [146, 167]. Thus, there currently exists an inability to assess the size and conformation of encapsulated guests; bridging this gap would allow greater understanding of a variety of biocomposite systems formed from ordered porous materials and proteins, enzymes and other biomacromolecules.

In this study, we employed small-angle x-ray scattering (SAXS) to solve this problem. SAXS is an established technique for analyzing nanoparticles and biological macromolecules in solution [168, 169]. When coupled with synchrotron-source radiation, SAXS becomes a robust method for resolving the size, structure, and oligomeric state of proteins [87, 170-172]. Furthermore, this method can be used to observe a protein's structural changes in real-time, allowing the study of protein stability *in situ* [173, 174]. SAXS data analysis techniques like the Guinier and Kratky plots are generally employed to reveal the protein's radius of gyration and degree of folding, respectively [175, 176]. Furthermore, the most used SAXS analysis tool is the pair distance distribution function (PDDF), a frequency plot of interatomic distances mathematically derived from the raw intensity plot [177]. Interpretation of the PDDF can allow assessment of the protein's geometry and tertiary structure [178].

Guided by prior studies of unencapsulated proteins, we demonstrate here that synchrotron-source SAXS measurements on protein-MOF biocomposites may allow structural analysis of still-encapsulated guest molecules for the first time. We achieved this by scaling the pure MOF SAXS spectra by a scalar value and subtracting it from the raw intensity plot of the MOF biocomposite (Figure 4.1). In this approach, the scaling subtraction factor may be determined analytically using physical characteristics of the biocomposite system, or empirically by inspection of the raw SAXS spectra.

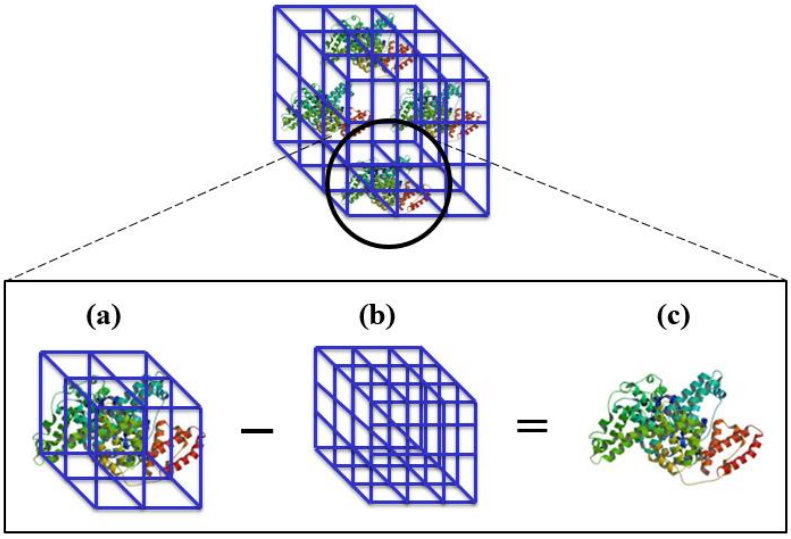

Figure 4.1: Visual depiction of scaled spectra subtraction approach; (a) BSA@MOF biocomposite, (b) pure MOF, and (c) encapsulated protein. Before employing this spectra subtraction approach, solvent background subtraction is completed for both the biocomposite and pure MOF. Note that SAXS spectra are measured in reciprocal space ($Å^{-1}$), so this scheme is included solely as a visualization method.

In conventional SAXS experiments, background subtraction of the solvent from the protein solution is necessary for meaningful data analysis [179]. While this approach works well in two-component systems where both volume fractions are known, we employed an empirical approach in our scaled spectra subtraction because the biocomposite system has three components: the protein, the MOF structure, and the solvent with unknown fractions in the scattering volume. If we assume that scattering from the biocomposite is a linear combination of the protein, the MOF, and the solvent components, we can use scaled subtraction to calculate encapsulated protein spectra in a method comparable to standard background subtraction. The standard SAXS analysis techniques (Guinier, Kratky, and PDDF) can then be performed on the calculated encapsulated protein's spectra.

The biocomposites reported here were composed of bovine serum albumin (BSA) encapsulated within two zeolitic imidazolate frameworks (ZIFs) named ZIF-67 and ZIF-8.

These frameworks are in a subfamily of MOFs composed of the ligand 2-methyl imidazole and either cobalt or zinc as the metal center, forming the isostructural ZIF-67 or ZIF-8, respectively [180, 181]. BSA was selected as the guest species due to its ubiquity and well-characterized denaturation behavior [182]. ZIF-67 was selected as the host due to its stability in water and accessibility by room-temperature, aqueous synthesis—both with and without the guest molecule present [136, 183]. This is notable, as typical MOF syntheses involve temperatures and/or solvents that would damage a proteinaceous guest [131].

By performing SAXS measurements on the synthesized biocomposites (BSA@ZIF-67 and BSA@ZIF-8) and then comparing these results to physical mixtures of pure MOF species and BSA, we determined the ideal conditions for our spectra subtraction approach. We then conducted SAXS measurements during *in situ* heating experiments past the denaturation temperature of BSA using a specialized sample holder, which demonstrated BSA stability resulting from MOF encapsulation.

4.3 Materials and methods

4.3.1 Materials

Bovine Serum Albumin (≥ 96%, Sigma-Aldrich, St. Louis, MO, USA), Triethylamine (TEA, 98%, Sigma-Aldrich), Ethanol (90%, Sigma-Aldrich), HEPES (4-(2-hydroxyethyl)-1-piperazineethanesulfonic acid) (99.5%, Sigma-Aldrich), Zinc (II) Acetate Dihydrate (≥ 98%, Sigma-Aldrich), Zinc (II) Nitrate Hexahydrate (98%, Sigma-Aldrich), Cobalt (II) Nitrate Hexahydrate (≥ 97.7%, Alfa Aesar, Ward Hill, MA, USA), 2-methyl imidazole (≥ 98%, TCI, Tokyo, Japan). Deionized (DI) water was supplied by an in-house system (Thermo Fisher, Waltham, MA, USA).

4.3.2 Preparation of pure MOFs, biocomposites, and mixtures

4.3.2.1 Room-temperature synthesis of pure ZIF-67 and ZIF-8

Synthesis procedures were adapted from those reported by Gross *et al.* [136]. ZIF-67 structures with a 1:16:16 ratio of metal : ligand : TEA were prepared by first dissolving 0.717 g cobalt (II) nitrate (2.46 mmol) in 50 mL DI water. Then, a solution of 3.244 g HMe-Im (39.5 mmol) and 4.00 g TEA (39.52 mmol) in 50 mL DI water was stirred until dissolved. In the case of ZIF-8, the cobalt salt was substituted for 0.733 g zinc (II) nitrate (2.46 mmol). The cobalt or zinc solution was added to the HMe-Im/TEA solution, and the resulting mixture was stirred for 10 min. This mixture was then separated via centrifugation (3.0 RCF, 10 min), decanted, and suspended in DI water for 12 h. This centrifugation process was repeated for a second water wash, and after 12 h, the ZIF suspension was centrifuged again, and the solid was collected. Solid ZIF crystals were finally dried in vacuum for 2 h at 150°C as described previously [136].

4.3.2.2 Room-temperature synthesis of BSA@ZIF-8 and BSA@ZIF-67

BSA@ZIF structures were prepared by first adding 40 mg of BSA to a solution of HMe-Im (160 mmol) in 20 mL DI water. A solution of cobalt (II) nitrate (40 mmol) or zinc (II) acetate (40 mmol) was then prepared in 20 mL DI water, and the solution was combined with the BSA solution and agitated to ensure thorough mixing as described in the work of Liang *et al.* [164]. The resulting mixture was aged overnight, separated *via* centrifugation (3.0 RCF, 10 min), and the supernatant was decanted. To remove residual BSA from the MOF crystals, the samples were washed four times: twice with water and twice with ethanol. Each wash cycle was completed by first adding 5 mL of wash solution to the MOF

crystals and then agitating the solution until the crystals were fully suspended. The mixture was then sonicated for 10 min, centrifuged, and decanted before adding the next wash solution. After the final centrifugation, the sample was decanted and dried in ambient air (20 – 25°C, 30 – 60% relative humidity) for 48 h.

Encapsulation efficiency (and therefore the BSA:MOF ratio) was quantified by taking samples post-centrifugation of the supernatant prior to decanting. These samples were analyzed using a BCA assay, which determined a consistent BSA encapsulation efficiency of ~80%.

4.3.2.3 Preparation of physical mixtures of BSA and MOF

Physical mixtures of lyophilized BSA and pure MOF components were prepared in BSA:MOF mass ratios of 1:9 (10% BSA) and 1:4 (20% BSA) by combining both powders and mixing thoroughly before suspending in 100 mM HEPES buffer in capillary tubes.

4.3.3 Confirming and quantifying degree of encapsulation

4.3.3.1 X-ray diffraction to confirm crystalline structure

Powder x-ray diffraction (pXRD) was used to confirm the structure of MOF crystals. For ZIF-8 samples, this was performed using a XPert Pro Alpha-1 diffractometer with X'Celerator detector using Cu $K\alpha_1$ radiation (λ=1.54184 Å) (Malvern Panalytical, Malvern, United Kingdom), as described previously [184].

For ZIF-67 samples, a PANalytical Empyrean diffractometer with PIXcel^{3D} detector using Cu $K\alpha_1$ radiation (λ=1.54184 Å) (Malvern) was used to reduce the effect

background fluorescence and improve diffractogram visualization due to the presence of cobalt in the MOF. Biocomposites were ground into a powder with mortar and pestle before analysis. All scans were prepared on a zero-background holder and performed in room temperature ambient air.

4.3.3.2 FTIR to assess structural incorporation

Fourier-transform infrared spectroscopy (FTIR) measurements were done on a Nicolet iS10 FTIR spectrometer with the Smart iTX diamond attenuated total reflection (ATR) accessory (Thermo Fisher, Waltham, MA, USA). Pure MOFs, biocomposites, and lyophilized proteins were all analyzed as dry powders.

4.3.3.3 SEM for visualization of crystallites

Crystals were prepared by gold sputtering (Hummer 6 sputterer, Ladd Research, Williston, VT) for 5 minutes before visualization by scanning electron microscopy (SU8230, Hitachi, Tokyo, Japan). Samples were observed at magnifications ranging from 5,000x to 30,000x zoom at a voltage of 10.0 kV.

4.3.3.4 BCA assay to quantify encapsulation efficiency

A BCA kit (Thermo Fisher Pierce, Waltham, MA) was used to measure un-encapsulated BSA concentration in supernatant after centrifugation during biocomposite synthesis [47]. Encapsulation efficiency was quantified by measuring the concentration of un-encapsulated BSA present in the post-centrifugation supernatant (1 mL) taken directly after centrifugation for the first water wash and the first ethanol wash after biocomposite

synthesis. This concentration was used to determine the amount of protein encapsulated and validate the success of the washing protocol.

4.3.4 SAXS analysis

4.3.4.1 SAXS with and without *in situ* heating

Solid samples were loaded into 1.5 mm O.D. quartz capillary tubes (Charles Supper Company, Westborough, MA, USA), and then suspended by pipetting 100 mM HEPES buffer into the capillaries and agitating to improve homogeneity within the scattering volume. Liquid samples were pipetted directly into the capillaries.

SAXS measurements were done by loading the capillary tubes on a capillary tube holder either with or without temperature control. All measurements were done with 20 keV x-rays with wavelength (λ) 0.62 Å at 15-ID-D station of NSF's ChemMatCARS (Sector 15) Advanced Photon Source. The scattered x-rays were measured with Pilatus 3X 300 K area detector with 1 mm silicon chip and sample-to-detector distance of 3.67 m. The images from the area detector were reduced to one-dimensional q vs I curves by azimuthal integration, where $q = \frac{4\pi}{\lambda}\sin\frac{\theta}{2}$ is the reciprocal lattice vector and θ is the scattering angle. The ambient temperature SAXS measurements were done at ~23°C and the high temperature measurements were done at 70°C.

4.3.4.2 Background Subtraction

Accurate subtraction of pure MOF spectra from the biocomposite to calculate encapsulated protein spectra was highly dependent on carefully selecting the scaling

subtraction factor, α. After importing the biocomposite, native protein, and pure MOF spectra into Excel (Microsoft, Redmond, WA, USA), the solvent background scattering was subtracted by established methods [185]. We then scaled the pure MOF spectra by some α ranging from 1 – 20. The initial α value was informed by the protein mass ratio within that specific biocomposite (~25%), but almost always had to be empirically adjusted due to variations in the density of the suspension, heterogeneity within the scattering volume, variable thickness of the capillary tubes, *etc*. The scaled pure MOF spectra was then subtracted from the biocomposite to yield the encapsulated protein spectra, and the α value was iterated to minimize the sum-squared error between the native and calculated protein spectra. Once the calculated raw protein spectra matched the native raw protein spectra (in absolute value), we continued analysis by PDDF, Guinier, and Kratky. Close agreement between the encapsulated and native protein spectra for raw SAXS intensity, Guinier analysis, and PDDF suggests successful and accurate subtraction.

4.3.4.3 Pair distribution function and Guinier Analysis with SasView

After performing background and/or MOF subtraction in Excel, the datasets were then inputted into SasView (www.sasview.org), an open-source analysis program used to generate pair distribution functions and Guinier fits. When inverting SAXS spectra into PDDFs, a Q-range of 0.05 $Å^{-1}$ – 0.25 $Å^{-1}$ was considered with a maximum interatomic distance of 100 Å. For fitting, regularization constants ranging from $1x10^{15}$ – $1x10^{19}$ were used. After analysis, all datasets were once more exported into Excel to create manuscript figures.

4.4 Results

4.4.1 Confirming BSA encapsulation within ZIF structure

Before analysis with SAXS, the synthesized biocomposites were characterized with XRD, FTIR, and SEM to confirm that BSA had been successfully embedded into the ZIF framework and that this structural incorporation did not disrupt the long-range order or general morphology of the ZIF host material (Figure 4.2).

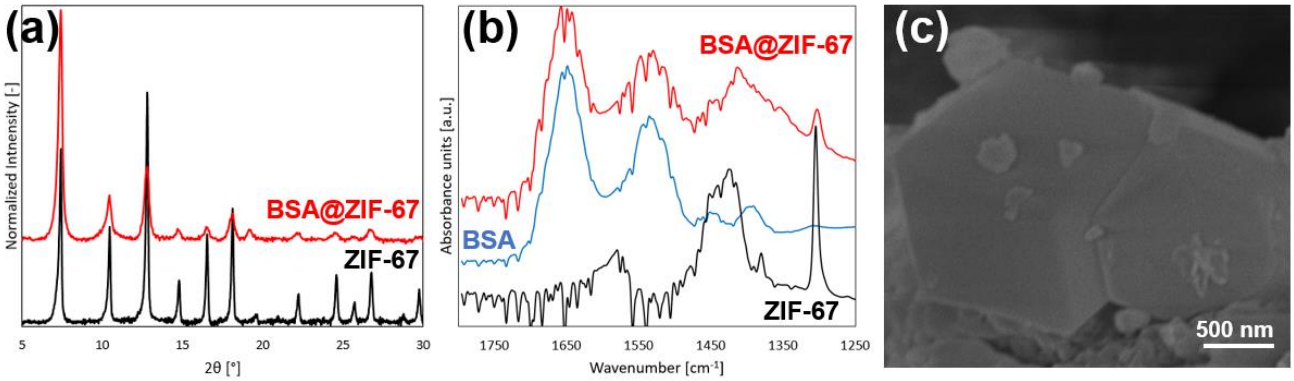

Figure 4.2: Characterization of BSA@ZIF-67 biocomposites. Representative XRD spectra of (a) BSA@ZIF-67 showing biocomposite (red) and MOF (black). Representative FTIR spectra of (b) BSA@ZIF-67, showing biocomposite (red), lyophilized BSA (blue), and MOF (black). Representative SEM image of (c) BSA@ZIF-67 crystallite with ~1 µm edge length.

Diffractograms for both the biocomposites (BSA@ZIF-8, BSA@ZIF-67) and pure MOFs (ZIF-8, ZIF-67) were similar to each other and showed strong agreement with the simulated pattern (Figure 4.2a, B.1.1a), as well as those previously reported in literature for ZIF-8 and ZIF-67 [186, 187]. The biocomposite patterns are nearly identical to those of the pure ZIF, except for a slight decrease in the apparent signal-to-noise ratio. This behavior has been observed in other biocomposites formed from proteins and MOFs [164, 188], and is likely caused by heterogeneous (*i.e.*, anisotropic) incorporation of BSA within the host framework resulting in mild disruption of the constructive scattering. Nonetheless,

these crystallography results provide compelling evidence that the long-range order of the host scaffold was not significantly compromised by protein encapsulation.

FTIR spectrograms of pure ZIF MOFs contain a characteristic plateau from 1475 cm^{-1} – 1400 cm^{-1} wavenumbers caused by the methyl bending mode from the HMe-Im ligands [189] (Figure 4.2b, B.1.1b). For the lyophilized BSA spectrogram, there are two proteinaceous peaks centered at 1650 cm^{-1} and 1550 cm^{-1}; these result from the protein's C=O and N–O stretching modes, respectively. Notably, the pure ZIF-8 and ZIF-67 spectra do not contain either of these proteinaceous peaks, as the framework lacks carbonyl and nitro groups. Finally, the biocomposites BSA@ZIF-8 and BSA@ZIF-67 spectrograms contain the carbonyl/nitro peaks of the protein as well as the characteristic plateau of the pure MOF. Because the two proteinaceous peaks experience a mild upward shift in wavenumber (~25 cm^{-1}) when seen in the biocomposite, there is likely a weak interaction between the protein and the MOF, suggesting that surface-bound BSA is not responsible for those peaks. Additionally, because the crystallites were washed rigorously with both water and ethanol before analysis, we expect that the proteinaceous peaks in the biocomposite are a result of protein encapsulation in the MOF.

SEM imaging shows MOF biocomposite crystals, which exhibit a characteristic rhombic dodecahedron geometry with an edge length of ~1 μm; this is expected of ZIF-8 and ZIF-67 crystallites, as reported extensively in literature [190]. The biocomposite crystallites have smooth surfaces showing no evidence of surface-bound proteins, which further suggests that the wash protocol was successful, confirming BSA encapsulation within the framework (Figure 4.2c, B.1.1c). Further evidence of encapsulation can be gathered by comparing BSA@ZIF crystallite and pure ZIF crystallite size (Figure B.1.2).

Crystallites of pure ZIF-67 (Figure B.1.2a) and ZIF-8 (Figure B.1.2b) are much smaller (100 – 200 nm) than the synthesized biocomposites, suggesting that guest proteins have a pronounced effect on crystal growth.

The mass percent of BSA in the biocomposites can be estimated using known literature values. Previous reports have suggested that encapsulation efficiencies of proteins into ZIF structures varies from 80 – 100%. We added 40 mg BSA to the biomimetic mineralization reaction, which yielded a biocomposite mass of ~160 mg. Assuming 32 – 40 mg of the initially added BSA was incorporated into the ZIF, we estimate that the BSA@ZIF materials are 20 – 25% protein by mass.

4.4.2 Subtraction approach reveals SAXS spectra of encapsulated BSA within biocomposites

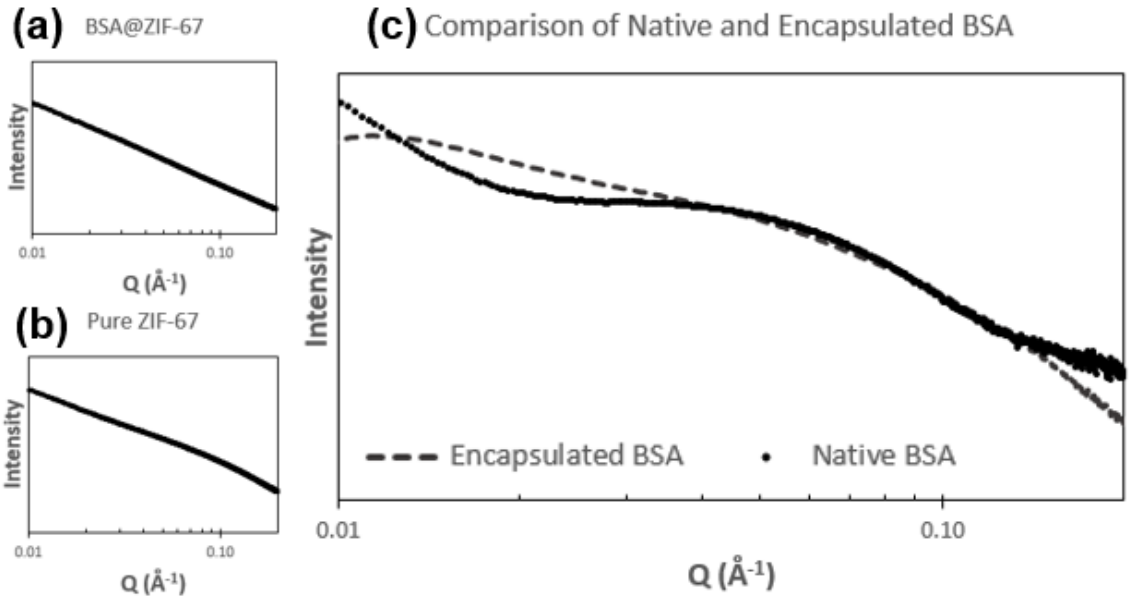

Figure 4.3: Representative SAXS intensity spectra showing scaled spectra subtraction to reveal encapsulated BSA in ZIF-67 biocomposite. Log-log scale graphs are shown for (a) BSA@ZIF-67, (b) ZIF-67, and (c) native or encapsulated BSA. Spectra for

encapsulated BSA (graph c) were generated by subtracting the ZIF-67 (graph b) spectrum from the BSA@ZIF-67 (graph a) spectrum, and compared to native BSA that was never encapsulated in MOF. Before subtracting MOF spectra from biocomposite spectra, solvent background subtraction was completed for all spectra. ZIF-8 and ZIF-67 spectra were subtracted from their corresponding biocomposite spectra using scaling subtraction factors of 5 and 20, respectively. Q-range is shown from 0.01 $Å^{-1}$ – 0.20 $Å^{-1}$. BSA@ZIF-8 and BSA@ZIF-67 were prepared at BSA:MOF ratios of 3:1 in HEPES buffer. The native BSA was prepared at a concentration of 4 mg/mL in HEPES buffer.

The SAXS spectra for the biocomposites (BSA@ZIF-8, BSA@ZIF-67) and the pure MOFs (ZIF-8, ZIF-67) are nearly indiscernible by visual inspection; this is owed largely to the MOF dominating the scattering in the Q-range shown (Figure 4.3a-c, B.1.3a-c). There were, nonetheless, differences between the biocomposite and pure-MOF spectra, which were revealed by subtracting the pure MOF spectrum from the biocomposite spectrum (Figure 4.3c, B.1.3c). The calculated "Encapsulated BSA" spectra are in sufficient agreement with the "Native BSA" spectra, suggesting that the scaled spectra subtraction approach can provide reasonable results. The biggest variation in the encapsulated and native BSA SAXS spectra is seen in the Q-range of 0.01 $Å^{-1}$ – 0.03 $Å^{-1}$, and is likely explained by differences in BSA aggregation behavior in solution versus when confined in the MOF. Successful subtraction to calculate encapsulated protein spectra in both ZIF-67 and ZIF-8 suggests that this approach is not dependent on a specific MOF, perhaps enabling analysis of other similar biocomposite systems. That said, the two MOFs species reported here were isostructural, so further study of MOF biocomposites would be necessary to validate this claim.

We next used these subtracted spectra to generate pair distance distribution functions (PDDFs), which provide a more quantitative representation of the encapsulated

protein's size and geometry compared to SAXS spectra and allow calculation of protein molecule radius of gyration (R_g). (Figure 4.4).

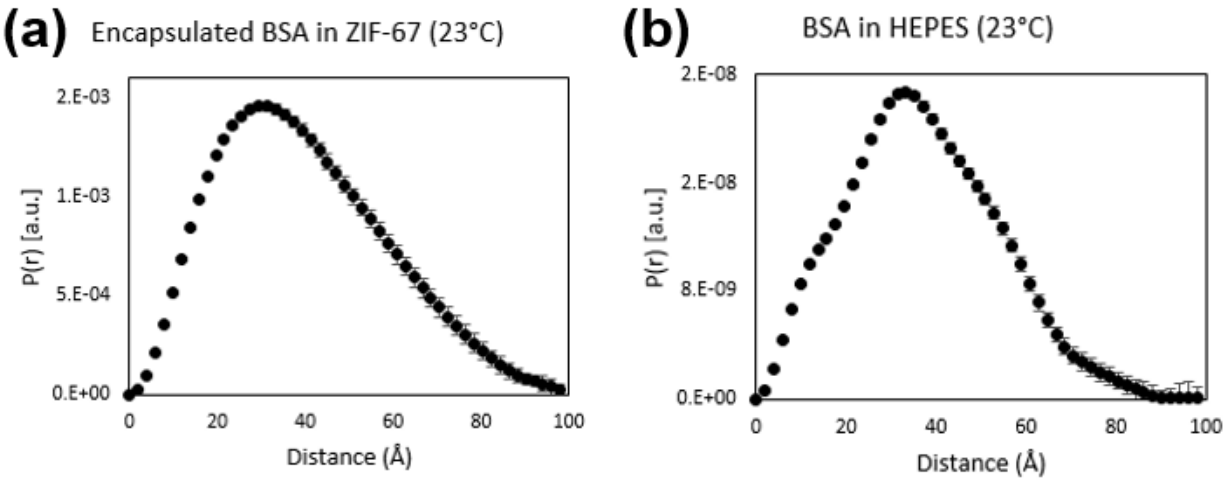

Figure 4.4: Representative PDDFs for BSA@ZIF-67 and BSA at 23°C. PDDFs shown for (a) calculated spectra of BSA encapsulated in ZIF-67 and (b) 4 mg/mL native BSA in HEPES buffer. R_g values calculated from PDDFs were 31.0 Å for encapsulated BSA and 28.8 Å for native BSA. Counterpart SAXS spectra are shown in Figure 4.3c.

The PDDFs for encapsulated and native BSA are in good agreement with each other and indicate that BSA assumed the expected globular (spherical) confirmation, as suggested by the bell-shaped curve shown in the PDDF [191]. The R_g values calculated from the PDDFs were all near 30 Å, and were in agreement with previous literature studies on free-standing BSA [192, 193]. This was true for calculated spectra of BSA encapsulated in ZIF-67 (Figure 4.4a) and ZIF-8 (Figure B.1.4). We also performed Guinier fits on the native and encapsulated BSA@ZIF-67 data, which further improved our confidence in the successful subtraction (Figure B.1.5). These graphs had similar shapes for the encapsulated and native BSA. Altogether, these findings provide confidence that the scaled spectra subtraction method can accurately calculate the encapsulated protein spectra and R_g values, allowing *in situ* SAXS-based analysis of embedded guests for the first time.

4.4.3 Subtraction approach applied to physical mixture of protein and MOF

The scaled spectra subtraction approach should similarly work to isolate the SAXS signal from lyophilized BSA in a physical mixture with pure MOF suspended together in buffer (Figure 4.5).

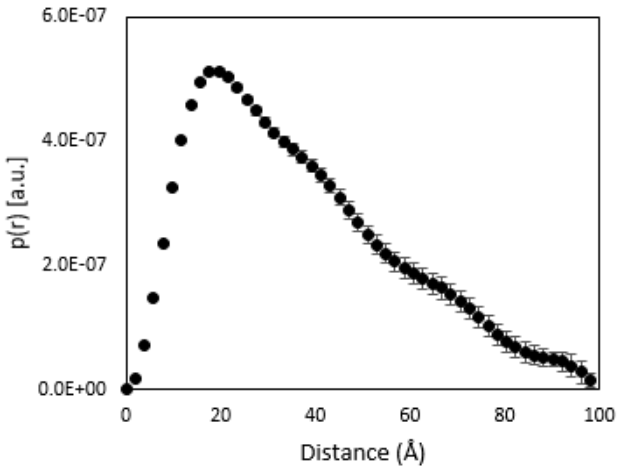

Figure 4.5: Representative PDDF from calculated spectra of a physical mixture of BSA and ZIF-67 prepared at a BSA:MOF ratio of 1:4 (20% BSA). Predicted R_g value from PDDF was 29.9 Å.

This expectation appeared generally to be correct, as the calculated PDDF from a mixture of BSA and ZIF-67 produced a characteristic shape expected for a protein, although with a somewhat flattened shape consistent with a cylindrical protein conformation rather than the more-rounded shape associated with globular proteins [191]. The difference could be explained by aggregation in solution or an insufficiently high protein mass ratio in the mixture. The predicted R_g value was 29.9 Å, in good agreement with the expected value [193]. This partially successful subtraction on a mixture of BSA and pure MOF suggests that this cannot be taken as evidence of encapsulation; for that, other experimental techniques such as FTIR and SEM must be employed.

It is also worth noting that this experiment used a BSA:MOF ratio of 1:4 (20% BSA), which provided sufficient signal from the protein to generate a calculated spectrum in agreement with pure BSA spectra. When we conducted a similar experiment using a mixture of BSA and ZIF-67 with a BSA:MOF ratio of just 1:9 (10% BSA), the pure BSA PDDF was poorly reproduced and the data had large error bars (Figure B.1.6), suggesting that there must be a minimum amount of protein in the sample such that its scattering is not "drowned out" by the MOF scattering contribution.

4.4.4 Subtraction approach during in situ heating of biocomposites

Development of the scaled spectra subtraction approach was motivated by the need to assess size and conformation of encapsulated protein as a measure of protein stability. We therefore subjected BSA to a thermal stress of 70°C for 3 h, both as native BSA and as a BSA@ZIF-67 biocomposite (Figure 4.6).

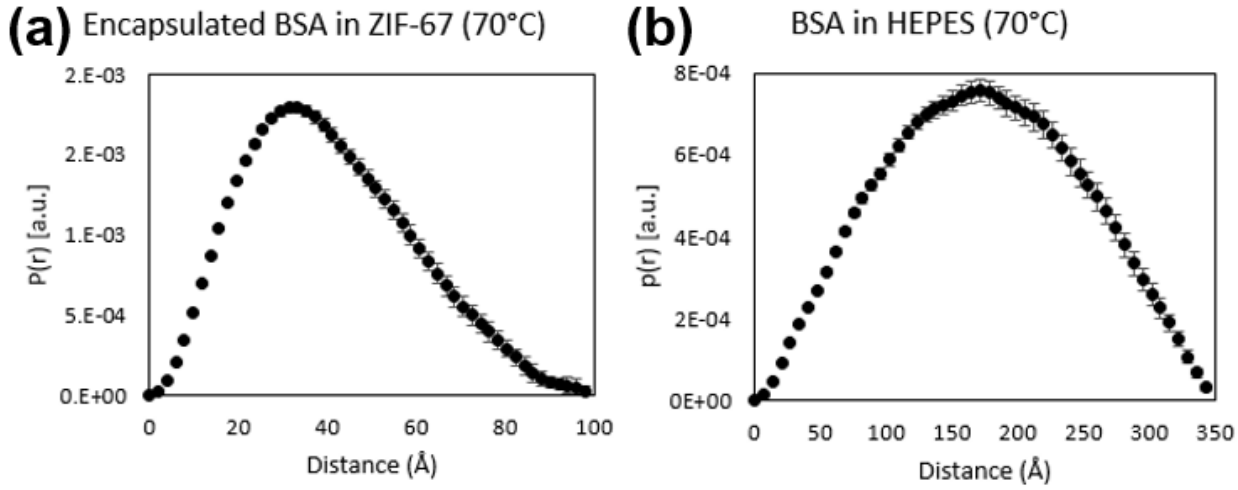

Figure 4.6: Representative PDDFs for BSA heated to 70°C. PDDFs from calculated spectra of (a) BSA@ZIF-67 and (b) BSA in HEPES buffer at a concentration of 4 mg/mL heated to 70°C for 3 h. Calculated R_g values were (a) 31.6 Å and (b) 133.0 Å. Corresponding PDDFs at 23°C are shown in Figure 4.4.

Comparison of BSA@ZIF-67 at 70°C and 23°C (Figure 4.6a and Figure 4.4a) showed no meaningful change in the PDDF of the encapsulated protein, indicating a stable protein conformation. R_g of BSA@ZIF-67 at 70°C was 31.6 Å, which varied only slightly from R_g of the biocomposite at 23°C (31.0 Å). These findings suggest that tight confinement of the protein guest within MOF cavities prevented its unfolding, and is at least partially responsible for increased thermostability caused by encapsulation [194].

In contrast, comparison of native BSA at these two temperatures (Figure 4.6b and Figure 4.4b) showed a marked change in the PDDFs, indicating dramatic changes to protein conformation. This is not surprising, as the denaturation temperature of BSA in solution is known to be 65°C [182]. Extended exposure to denaturing temperatures is expected to lead to loss of globular confirmation and protein aggregation, as evidenced both by PDDF broadening for the denatured BSA as well as visual inspection of the capillary tubes during *in situ* heating (data not shown). Additionally, the R_g value at 70°C increased to 133.0 Å, which was much greater than the value at 23°C (31.0 Å). This behavior is consistent with protein unfolding and aggregation as well as previous SAXS studies on the denaturation of BSA at 70°C [193].

To further assess the thermostability of BSA@ZIF-67, we conducted Kratky analysis of the calculated SAXS spectra, which provides a qualitative way to assess the nature of protein folding by plotting the SAXS intensity I(q) multiplied by Q^2 versus Q. In this approach depicted in Figure 4.7, Kratky plots of unknown samples are referenced against known Kratky plot shapes to assess the folded nature of proteins [96].

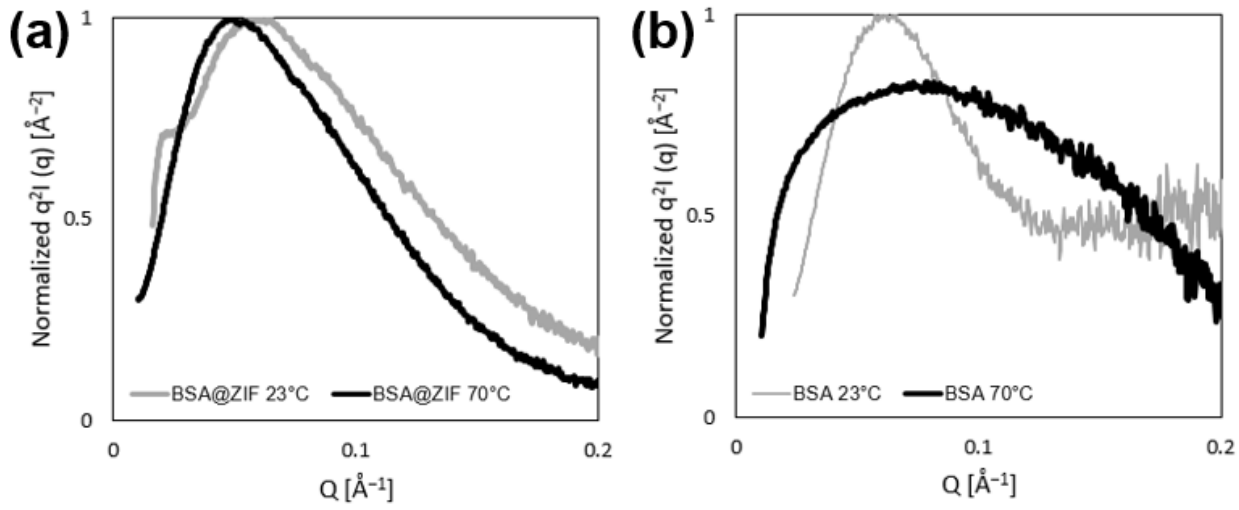

Figure 4.7: Representative Kratky plots of encapsulated and native BSA at 23°C and 70°C. Kratky plots from calculated spectra of (a) BSA@ZIF-67 as a dry powder and (b) native BSA in HEPES buffer at a concentration of 4 mg/mL heated to 70°C for 3 h. Corresponding PDDFs at 23°C are shown in Figure 4.4 and at 70°C are shown in Figure 4.6.

The Kratky plots for BSA@ZIF-67 at 23°C and 70°C show again that at both ambient and denaturing temperatures, the encapsulated BSA protein remained folded within the MOF cavities, as both curves exhibit the characteristic "folded" confirmation characteristic of Kratky plots [96] (Figure 4.7a). The Kratky plots also confirm that exposing BSA to elevated temperature led to extensive unfolding, manifesting as loss of the characteristic peak associated with folded proteins (Figure 4.7b). Thus, the combined insights from PDDF and Kratky analyses indicate that tight confinement of proteins within MOF cavities is associated with heightened thermostability that avoids protein conformational changes leading to denaturation.

4.5 Discussion and Conclusion

This study made advances in two areas: introduction of a new method to analyze encapsulated proteins *in situ* by SAXS and understanding of the protein stabilization mechanism by MOF encapsulation. First, we developed a method to calculate the SAXS spectra of a proteinaceous guest encapsulated within a MOF scaffold based on the expectation that the biocomposite scattering is an additive combination of the scatterings from the protein, MOF, and solvent. Using this approach, we were able to generate calculated SAXS spectra, as well as corresponding PDDFs, Guinier fits and Kratky plots, for BSA encapsulated in ZIF-67 and ZIF-8 that showed good agreement with native BSA SAXS results. We also considered the presence of dimers in the MOF biocomposites by studying a wider range of D_{max} values for the PDDFs (data not shown). Although we typically considered a maximum interatomic distance of 100 Å in this work, we also generated PDDFs with D_{max} values of 150 – 200 Å; if there were dimers present within MOF cavities, we would expect to see a secondary peak around 70 Å due to BSA dimers as noted in previous studies [182]. Because this secondary dimer peak was not observed in any of the MOF biocomposites, we ultimately concluded that BSA monomers almost exclusively occupied the cavities within ZIF structures.

We additionally showed that the subtraction approach yielded similar results for physical mixtures of BSA and ZIF-67, indicating that possible interactions between the encapsulated protein guest and the MOF host did not alter the SAXS spectra in meaningful ways. The fact that our approach worked for a mixture of BSA and ZIF suggests that successful subtraction cannot be taken as evidence of encapsulation; for this, material characterization techniques like FTIR and XRD should be employed. Consequently, we

would expect the BSA present in the mixture of BSA and ZIF-67 to denature when exposed to 70°C for 3 hours.

Accurate subtraction of the MOF spectrum to calculate encapsulated protein spectra was highly dependent on carefully selecting the scaling subtraction factor, α. In our analysis, we determined α through graphical and visual methods. This method to determine α provided a rough optimization that could be improved upon by more rigorous statistical methods and possibly by first-principle calculations that account for variation in experimental conditions. Although we adopted a trial-and-error approach for determining $\boldsymbol{\alpha}$ in this work, we also propose a mathematical basis for this scaling subtraction factor in Appendix B.2.

This work represents an important contribution to the field of MOF biocomposites. For the first time, the scaled spectra subtraction method enabled us to assess the size, shape, and folding of encapsulated proteins while they are still encapsulated with the MOF matrix. The ability to employ this approach during *in situ* heating also provided insight into the action of heightened guest thermostability afforded by MOF encapsulation, which has been hypothesized, but not shown, to be associated with physical immobilization of the protein to prevent changes to protein structure [64, 164]. By directly observing that encapsulated guests retained their size (evidenced by R_g consistent with native BSA) and conformation (shown by globular PDDF shapes) during exposure to elevated temperatures, our data indicate that tight confinement of guest molecules within roughly guest-sized MOF cavities is associated with, and may be largely responsible for, retaining protein structure and stability. The experimental evidence provided here discounts other possible explanations for heightened stability resulting from MOF incorporation, such as guest confirmational

changes upon encapsulation which are reversed upon liberation from the framework. Our SAXS studies clearly show that globular, folded protein structure is retained before and during MOF encapsulation.

Because the subtraction approach was demonstrated successfully for BSA encapsulated in two isostructural MOF species, our findings may have implications for a variety of fields employing biocomposites made from various proteins encapsulated in MOFs or other host structures. Our data indicate that so long as the biocomposite scattering is an additive combination of the pure MOF and protein spectra (*i.e.*, no significant protein-MOF interaction affects the SAXS spectra), the approach described here could be broadly applicable to similar host-guest systems. Greater insight into the stabilization mechanism associated with protein encapsulation may improve the rational design of MOF biocomposites used in vaccine storage, enzymatic reactions and other applications, benefitting global populations, researchers, and industrial processes [195].

In conclusion, this study introduced a new method that enabled calculation of SAXS spectra associated with protein encapsulated in MOF host matrices measured *in situ*. The method was based on scaled subtraction of the spectrum of pure MOF from the spectrum of the biocomposite to yield the spectral contribution of the protein. The approach was shown to be valid for BSA encapsulated in ZIF-8 and ZIF-67. BSA@ZIF-67 biocomposites and physical mixtures of BSA and ZIF-67 produced similar SAXS spectra, suggesting that successful subtraction is not evidence of encapsulation. Finally, the scaled spectra subtraction approach was used to show that BSA conformation when encapsulated in ZIF-67 was unchanged during heating to 70°C for 3 h, while pure BSA without MOF encapsulation was fully denatured and unfolded. This finding suggests that protein

thermostability by MOF encapsulation may be due to physical entrapment of the protein that prevents conformational changes. The findings of this study could enable future *in situ* SAXS analyses performed on proteins or other compounds encapsulated in MOFs (as well as other host matrices) to advance fundamental research and translation into applications involving protein encapsulation and stabilization.

CHAPTER 5. DISCUSSION

In CHAPTERS 3 and 4, we provided evidence for: (1) the feasibility of metal-organic framework (MOF) encapsulation for long-term vaccine storage to address the cold chain problem and (2) the action of increased guest stability afforded by guest confinement within MOF structures. In this section, we will compare our results to the broader literature landscape and discuss the implications of our findings. For our studies on the stabilization of Tetanus Toxoid (TT) within zeolitic imidazolate framework-8 (ZIF-8), this discussion centers around improvements to literature reports and the real-world translatability of MOF encapsulation to break the cold chain. The discussion surrounding our experiments to elucidate the mechanism of enhanced thermostability focuses on comparing our findings to other hypotheses in the literature, as well as identifying additional biocomposite systems which may benefit from the spectra subtraction approach we introduced in CHAPTER 4.

5.1 Addressing literature gaps on MOFs for vaccine storage

As mentioned in CHAPTER 2, MOF encapsulation to enhance biological molecule stability is a relatively new field that emerged within the last decade. Thus, there were several gaps in the literature we sought to address in this body of work. Until now, most related studies focused on guests of low clinical relevance, only considered MOF biocomposite stability on the order of days, and did not examine the possibility of liquid formulations of vaccine-MOF biocomposites. One recent study that assessed some of these gaps was conducted by Singh *et al.* in 2022 [194]. In this work, the authors successfully encapsulated Newcastle disease virus (NDV) within ZIF-8 and measured the thermostability of the NDV@ZIF-8 biocomposite over 12 weeks at a maximum

temperature of 37°C. While this was perhaps the first group to measure MOF biocomposite stability on the scale of months, they only examined solid formulations (that included lyophilization) and did not predict the long-term stability of their materials. Because vaccines are often expected to be shelf-stable for 6 to 12 months, the 12-week study done by Singh *et al.* left some doubt about the feasibility of MOF biocomposites for real-world vaccine storage applications [196]. Additionally, while this group's encapsulation of the live virus NDV was an impressive proof of concept for the plethora of guests stabilized by MOF encapsulation, this disease primarily affects avian populations, significantly lowering its translational relevance [197].

Our work expanded the scope of knowledge within the field as we demonstrated MOF encapsulation as a viable method for long-term storage of Tetanus Toxoid, a vaccine of high clinical importance, especially in the developing world [198]. We also studied aqueous and organic suspensions of the TT@ZIF biocomposite, finding that suspension in a mixture of propylene glycol and ethanol yielded better stability results than the dried TT@ZIF powder, perhaps enabling shelf-lives of one year at temperatures below 25°C. The method of suspending ZIF biocomposites in non-aqueous solvents to avoid degradation by ambient moisture may serve as a general approach for improving vaccine-MOF stability, as well as eliminate an extra solvation step at the hypothetical site of administration.

5.2 **Feasibility of vaccine-MOF composites for breaking the cold chain**

As with all novel technologies, there are several obstacles associated with translating an idea from the benchtop to the real world. In this section, we discuss possible barriers for

employing MOFs to eliminate the need for refrigeration during vaccine transport. We also compare the MOF encapsulation approach to several widely accepted vaccine stabilization methods described in CHAPTER 2.

5.2.1 Producing TT@ZIF at a global scale

According to the World Health Organization, there were 18.2 million infants in 2021 who did not receive a single dose of the DTaP (diphtheria, tetanus, and pertussis) vaccine [32]. For TT specifically, the CDC recommends children receive five doses in the first 6 years of life [199]. To fully cover each of the unvaccinated infants from last year, 91 million doses would be necessary over the next 6 years. Assuming a single dose of TT is 10 μg and the TT@ZIF biocomposite is roughly 10% vaccine by mass, 9.1 kg of the TT@ZIF biocomposite would be needed to address the TT vaccine needs of unvaccinated infants from 2021 alone [200]. While the pure ZIF-8 can already be produced at a rate of nearly 1 kilogram per hour, scaled-up manufacture of ZIF-based biocomposites is a lingering engineering challenge [201].

In 2020, Carraro *et al.* designed an apparatus that produced ZIF-8 biocomposites (using bovine serum albumin as a model guest) through a continuous flow reactor [202]. Although this work represented a significant step towards scaled-up production of MOF biocomposite materials, the maximum production rate achieved in this study was 2.1 grams per hour. In preparing vaccine-MOF formulations for real-world applications, synthesizing the biocomposites is only the first step. After the crystals are formed, they must be surface washed several times with water, ethanol, and sometimes a surfactant. This processes may

be difficult to achieve at scale, and might therefore pose a significant barrier for vaccine-MOF production to meet global demand.

5.2.2 Safety considerations

Due to nascent nature of MOF encapsulations for vaccine storage, the safety and toxicity of these materials in living systems are not well-understood. While some studies have examined the toxicity effects of pure MOFs on cell cultures and some animal models [86, 203], there are very few literature reports of MOF biocomposites introduced to live animals. In 2019, Luzuriaga *et al.* encapsulated tobacco mosaic virus (TMV) in ZIF-8 and injected 4 BALB/c mice with the TMV@ZIF biocomposite, observing no negative health effects as a result of biocomposite administration [64]. While this is an encouraging initial report for the translational feasibility of these materials, more-extensive safety studies are needed. The problem of MOF toxicity is further complicated by synergistic cytotoxic effects observed when administering pure MOFs alongside other drugs [83]. Thus, the only way to answer the question of MOF biocomposite safety in living systems is to prepare various biocomposites and test their toxicity *in vivo,* beginning with murine models.

5.2.3 Advantages over conventional vaccine stabilization methods

In CHAPTER 2, several drawbacks associated with conventional vaccine stabilization approaches were discussed. Our work has contributed to the increasing literature evidence that vaccine stabilization with MOFs could assuage several of the issues surrounding these widely accepted stabilization methods. Lyophilization is one such approach that is expensive, energy intensive, produced in a batch process, and requires reconstitution (hence, great medical expertise) at the healthcare facility [37]. In contrast,

MOF biocomposites can be manufactured from relatively cheap and widely available precursors at room temperature. Recent studies have also shown that protein-MOF materials can be produced in a continuous process, although thorough washing of the crystallite surfaces might introduce a batch step [202]. Furthermore, because we found an organic solvent suspension to be the most stable storage condition, these materials may be formulated as liquids, removing the need for reconstitution at the site. Initial studies on delivering intact vaccine-MOF nanoparticles suggest that the MOF structure need not be exfoliated before injection to produce an immune response [64], perhaps eliminating the need for any further modifications to the vaccine at the administration site, likely improving health outcomes.

When compared to addition of excipients that must be tailored for each new stable vaccine formulation, vaccine-MOF materials adopt a more one-size-fits-all approach, as several different guests including proteins, viruses, and cells have been encapsulated [68]. A 2018 study by Maddigan *et al.* suggested the main criteria that determines spontaneous ZIF-8 framework around the guest is its surface zeta potential; this provides a simple method to predict which guests are amenable to encapsulation within MOFs, perhaps saving significant time and effort in formulating stable vaccines [153]. Other methods for vaccine stabilization such as polymeric microneedles, while promising in their ability to avoid reconstitution and reduce sharps waste, need substantial logistical and engineering developments before widespread implementation [49]. Preliminary studies on scaled-up manufacture of MOF biocomposites suggest that there might be comparatively fewer barriers to large-scale production [202].

5.3 Assessing literature hypotheses on thermostability mechanism

One of the major contributions of our work was to elucidate the mechanism of enhanced thermostability resulting from encapsulation within the ZIF structure. In the past, groups have speculated that tight confinement of guest molecules within the MOF is responsible for the improved stability. In 2015, Liang *et al.* performed small angle x-ray scattering measurements on room-temperature BSA@ZIF-8, suggesting that the cavity size was 10% greater than the guest BSA [66]. We provided strong additional evidence for this hypothesis by interrogating the structure, size, and folded state of still-encapsulated bovine serum albumin within ZIF-8 at ambient and normally denaturing (70°C) temperatures. This experiment revealed that encapsulated proteins did not unfold upon thermal exposure, likely because the cavities formed in the MOF structure by guest incorporation did not physically allow this. While the studies by Liang *et al.* may have anticipated this result, our data provides concrete evidence that the MOF structure prevents protein unfolding. Our findings are consistent with prior literature showing that immobilized enzymes are stabilized in other inorganic matrices by the same mechanism [204].

5.4 Applying spectra subtraction approach to other biocomposite systems

Since our work demonstrated that subtracting the SAXS spectra of pure ZIF from the BSA@ZIF spectra yielded the encapsulated BSA spectra for both ZIF-8 and ZIF-67, we speculated that this same approach could be employed on other biocomposite systems such as biomacromolecules embedded within mesoporous silicas. Nonetheless, there is a chance the subtraction approach is specific to ZIF structures, especially because ZIF-8 and ZIF-67 are isostructural, varying only in the identity of their metal center (zinc or cobalt, respectively) [205]. Nonetheless, with the variety of new guests being incorporated into ZIF-8, as well as the recent synthesis of vaccine-MOF composites from frameworks other

than ZIF-8, this approach applied to other systems may yield interesting insights [194]. One important parameter that could need optimizing before employing this approach to different host-guest pairs is the protein-to-MOF ratio. Our SAXS studies on BSA@ZIF materials have given reason to speculate that the mass ratio of protein within a biocomposite sample must be sufficiently high to enable subtraction such that the MOF scattering does not "drown out" the scattering from the protein. The BSA@ZIF materials analyzed in CHAPTER 4 were approximately 25% BSA by mass, which appeared to provide a sufficient amount of protein for analysis by MOF spectra subtraction.

CHAPTER 6. CONCLUSION

In the first part of CHAPTER 3, we applied the approach of metal-organic framework (MOF) encapsulation to assess the long-term thermostability of tetanus toxoid (TT) vaccine trapped within a zeolitic imidazole framework (ZIF). We first confirmed that TT was successfully encapsulated within the ZIF structure through a variety of material characterization methods. X-ray diffraction showed that crystallinity of the pure ZIF was not considerably affected by guest incorporation, while Fourier transform infrared spectroscopy provided strong evidence of encapsulation, as peak shifts due to guest-framework interactions were observed after rigorously washing the crystallite surfaces. We observed that TT was distributed throughout the crystallite bulk with confocal microscopy, and visualized the TT@ZIF surface with scanning electron microscopy, revealing an average crystallite size of ~600 μm and a wide distribution of crystallite sizes (50 – 700 μm). After confirming encapsulation, enzyme-linked immunosorbent assay of TT released from the TT@ZIF biocomposite measured a release efficiency of approximately 60%.

In the second part of CHAPTER 3, thermostability of TT@ZIF was measured in a variety of solid and liquid formulations through accelerated stability studies at 40°C and 60°C. Because of the ZIF's tendency to degrade in aqueous (or even mildly humid) conditions, the best stability results were found for TT@ZIF particles suspended in an organic solvent. By solvating in a 4:1 mixture of propylene glycol and ethanol, TT@ZIF particles retained 85% ± 3% and 79% ± 8% activity after three months of storage at 40°C and 60°C, respectively. This represented a marked improvement over unencapsulated vaccines subject to the same conditions, which lost full activity after just one day at 60°C.

Dried TT@ZIF powder provided the next best results, affording 62% ± 11% activity and 32% ± 2% after three months of storage at 40°C and 60°C. In the same experiments, lyophilized TT lost full activity within one week. Of all studied biocomposite samples, the worst stability results were obtained for TT@ZIF suspended in water, which retained only 22% ± 7% (at 40°C) and 7% ± 3% (at 60°C) activity after three months. This was likely due to hydrolysis of the ZIF structure, which released TT into the bulk water where it was quickly denatured. The accelerated stability studies were extrapolated to lower, clinically-relevant temperatures (ranging from 5°C – 30°C) through the Arrhenius equation, suggesting that the non-aqueous suspension of TT@ZIF would retain shelf stability for at least 1 year at temperatures below 25°C. Furthermore, a 4-week *in vivo* study in a murine model suggested that TT@ZIF provides reasonable immune responses. Although the non-aqueous solvent appeared to have an immunosuppressive effect, the intact pure MOF particles appeared to provide an adjuvant effect, suggesting that framework dissolution before injection may not be necessary.

In CHAPTER 4, we provided evidence for the action of heightened thermostability imparted by MOF encapsulation using *in situ* small angle x-ray scattering (SAXS). In these experiments, a model protein guest (bovine serum albumin, BSA) was encapsulated in ZIF-8 and the isostructural ZIF-67. We characterized BSA@ZIF-8 and BSA@ZIF-67 with the same methods employed in CHAPTER 3, concluding that guest encapsulation was achieved. In collaboration with Argonne National Labs, we developed a new technique that exploited subtracting the pure ZIF spectra from the BSA@ZIF composite spectra to yield the spectra of the encapsulated protein. This enabled size and structural resolution of the still-encapsulated BSA molecules, especially when exposed to a normally denaturing

temperature of 70°C *in situ.* By observing the nearly identical size, shape, and degree of folding for encapsulated BSA at both ambient and elevated temperatures, we concluded that rigid confinement of the protein within MOF cavities prevents protein unfolding, enables retention of tertiary structure, and can thus explain the observed heightened thermostability.

The findings presented in this work represent a significant step forward in validating the translational viability of vaccine-MOF biocomposites. To our knowledge, we have demonstrated the encapsulation and long-term thermostability of a clinically relevant vaccine guest for the first time. Our studies suggest that suspending TT@ZIF in organic solvents can significantly improve ZIF (and therefore, vaccine) stability. This highly thermostable liquid formulation has a variety of benefits for real-world immunization efforts, as no reconstitution step or knowledge about cold chain storage and handling practices would be necessary at the site of administration. Furthermore, our SAXS experiments provided strong evidence to support the hypothesis that improved guest stability through MOF encapsulation relies on locking the guest's 3-D structure in place.

Overall, our research suggests that MOF encapsulation is a feasible approach for long-term vaccine storage and breaking the cold chain, providing numerous benefits over standard stabilization approaches. Furthermore, the insights gleaned into the stabilization mechanism within these biocomposites may be abstracted to other similar systems, serving as a foothold for additional optimization.

CHAPTER 7. FUTURE DIRECTIONS

Metal-organic framework (MOF) encapsulation of biological molecules to enhance their thermostability is a burgeoning and recently discovered field. As such, there are several additional avenues that may be pursued to widen the scope of the findings from this work and further prove the translational viability of this method for breaking the cold chain. In this section, we will consider both the short-term and long-term outlooks for the research done in CHAPTERS 3 and 4.

7.1 Thermostability and Immunogenicity of vaccine-MOF biocomposites

In CHAPTER 3, we encapsulated tetanus toxoid (TT) within a zeolitic imidazolate framework (ZIF) and demonstrated its remarkable long-term thermostability in a variety of conditions, ultimately finding that liquid suspension in a mixture of propylene glycol and ethanol afforded the greatest activity retention (~90% after 3 months at 40˚C). Using our work as a starting point, a variety of optimizations and future studies could be designed. For this aim, additional studies in the short-term (*i.e.*, within 6 months) would center around screening other organic solvents for TT@ZIF suspension, linking TT activity losses to crystallite degradation observed with scanning electron microscopy (SEM) and x-ray diffraction (XRD), and an *in vivo* study in a murine model to assess the immunogenic responses of live animals to TT@ZIF formulations. Long-term future studies could involve incorporating other components of the DTaP vaccine into ZIF structures as well as casting vaccine-ZIF materials into polymeric microneedles.

7.1.1 Immediate follow-up studies on TT@ZIF biocomposites

7.1.1.1 Screening other organic solvents for TT@ZIF suspension

Our accelerated stability studies suggested that the long-term stability of TT@ZIF crystallites is negatively affected by the presence of residual moisture in the packaging, even when stored with desiccant. Consequently, the best stability results were achieved by suspending TT@ZIF in a mixture of propylene glycol (PG) and ethanol (Et), reducing the rate of ZIF-8 framework degradation by hydrolysis. This organic solvent was chosen based on several criteria including biocompatibility, a non-damaging environment for ZIF, appropriate density to form a stable suspension, and lack of interference with immunoassay measurements.

While the organic suspension we employed in CHAPTER 3 achieved the goal of retaining thermostability, initial *in vivo* studies showed that injection of TT solvated in a PG/Et mixture provided lower immune responses than TT solvated in phosphate-buffered saline (PBS). While it is unclear what caused this lowered immune response, we speculated that the high-viscosity organic solvent interfered with transport processes and local initiation of immune responses in the subcutaneous space, perhaps reducing cellular uptake and thus, production of anti-TT antibodies. As such, an organic solvent that meets the aforementioned criteria while still allowing an immune response comparable to PBS-solvated TT would represent a key step forward in translating vaccine-MOF biocomposites. The ideal organic solvent would therefore retain remarkable TT@ZIF thermostability (as PG/Et did) while concurrently inducing a strong immune response *in vivo*.

7.1.1.2 Linking TT activity loss to ZIF degradation

Our studies on TT@ZIF activity losses in a variety of harsh conditions afforded insights into the upper-bound thermostability limits of vaccine-ZIF biocomposites. Linking the activity losses measured by enzyme-linked immunosorbent assay (ELISA) to physical changes in the TT@ZIF crystallites observed with SEM would provide further evidence that the intact, rigid MOF structure is necessary for guest stabilization. In this proposed experiment, TT@ZIF biocomposites would be observed with SEM before and after thermal exposure, and we would expect to see significant degradation of the ZIF structure for samples that lost significant activity. Conversely, we would expect to see minimal changes to the biocomposite crystallite morphology in formulations that allowed full stability retention. There is precedence for linking structural and stability losses with TEM in the literature, demonstrated by the work of Singh *et al.* [194].

Additional evidence of framework degradation could be observed with XRD, where loss of the sharp ZIF peaks due to structural changes may be correlated with activity losses. Literature precedence for this experiment also exists in a study by Liang *et al.* which reported encapsulation of horseradish peroxidase (HRP) in ZIF-8 [66]. In this work, the authors presented evidence of structural retention by taking XRD measurements of HRP@ZIF-8 exposed to harsh conditions, observing no appreciable changes in the diffractogram. In general, performing material characterizations on biocomposites after thermal exposure would yield insights into the relationship between activity loss and structural retention.

7.1.1.3 Measuring *in vivo* responses to TT@ZIF

Although our ELISA studies provide strong *in vitro* evidence for the thermostabilizing effects of MOF encapsulation on tetanus, measuring *in vivo* responses to TT@ZIF formulations is paramount for demonstrating the translational feasibility of this approach. In 2019, Luzuriaga *et al.* measured immunogenic responses to a ZIF-8 biocomposite encapsulating tobacco mosaic virus (TMV) [64]. In this experiment, the authors injected 4 BALB/c mice with both TMV and TMV@ZIF and measured immune responses. That study found that no negative health effects were observed in the mice, and TMV@ZIF gave approximately the same immune response as TMV over 35 days.

A natural follow-up experiment to the *in vivo* studies on TT@ZIF we present in this work would be to administer thermally exposed TT@ZIF to a murine model. This would confirm that the retained *in vitro* thermostability observed with ELISA translates to a live animal model. Controlled release and booster effects of TT@ZIF may also be studied, which may have strong translational implications for toxoid and inactivated virus vaccines, as these often require several boosters during the early childhood years.

7.1.2 Long-term follow-up studies on TT@ZIF biocomposites

7.1.2.1 Encapsulating numerous guests within ZIF-8

The tetanus toxoid vaccine is frequently administered in conjunction with the Diphtheria and Pertussis Toxoid vaccines in a formulation called DTaP. Consequently, embedding two or all three of these clinically relevant vaccines into a single ZIF-8 structure may possess translational benefits. Recently, Man *et al.* employed epitaxial growth on ZIF-8 biocomposites to create multi-enzyme@ZIF materials [206]. In this study, the authors reported encapsulation of both glucose oxidase (GOx) and horseradish peroxidase (HRP)

in a single phase. Their approach was to first synthesize GOx@ZIF-8, then epitaxially grow HRP@ZIF-8 around these crystallites to form GOx@ZIF-8@HRP@ZIF-8 biocomposites.

A similar approach may be used to create biocomposites like Tetanus@ZIF-8@Pertussis@ZIF-8, perhaps enabling encapsulation of all three DTaP toxoid vaccine components into a single ZIF structure. Of course, because the epitaxially grown MOF biocomposites would possess a different structure, release kinetics, and *in vivo* effects, further studies would need to be performed on these multi-toxoid@ZIF materials. Another approach for studying the stabilization of all DTaP vaccine components within ZIF structures would be to encapsulate each of the three toxoids in a different ZIF-8 structure and study the *in vivo* effects of delivering all vaccine-ZIF composites at the same time. This would avoid having several antigens within a single cell, perhaps improving immune responses.

7.1.2.2 Microneedle patch design with vaccine-ZIF materials

To leverage the remarkable thermostability of TT@ZIF biocomposites, they would conventionally still need to be administered *via* subcutaneous injection, which invariably produces hazardous sharps waste. This problem may be assuaged by embedding TT@ZIF particles into polymeric microneedle patches (MNPs) before administration. Such an approach would exploit the thermostability of MOF biocomposites while enabling more widespread vaccine access. There is literature precedence for this idea; Jung *et al.* embedded curcumin and ZIF-8 particles into polymeric microneedles, exploiting the low pH of the insertion site to degrade ZIF-8 and release curcumin upon administration of the MNP [207]. Although this work has strong translational implications, they demonstrated

their method on a small-molecule model drug and relied on physiological conditions to degrade the ZIF-8 framework. This leaves the feasibility of this method's application to MOF biocomposites formed by the encapsulation of large biomacromolecules in question.

A follow-up study relating to the work we presented here would be to embed Vaccine@ZIF particles in polymeric microneedles and avoid relying on physical conditions to degrade the ZIF by incorporating EDTA (the exfoliating agent) into the MNP. This would allow the study of clinically relevant biomolecules encapsulated within ZIF-8 and then embedded into MNPs. Furthermore, the dissolution rate of Vaccine@ZIF once administered *via* MNP may be tuned by varying the amount and/or molarity of EDTA incorporated into the MNP. The scope of expertise in the Prausnitz Lab is particularly well-suited for this proposed study.

7.2 **Interrogating the structures of MOF-encapsulated guests**

In CHAPTER 4, we employed scaled subtraction of small angle x-ray scattering (SAXS) spectra to reveal the structure of still-encapsulated bovine serum albumin (BSA) in both the ZIF-67 and ZIF-8 frameworks. From these experiments, we concluded that guest confinement within nearly conformally-sized MOF cavities prevented protein unfolding (and thus, activity loss) even when exposed to normally denaturing temperatures *in situ*. As this subtraction method may be potentially abstracted to other inorganic-organic biocomposite systems (*e.g.*, mesoporous silicas), there are various follow-up studies that could be conducted based on our work. In the short-term, these experiments would center around employing this method on TT@ZIF and other ZIF-based biocomposites. In the long-term, studies on the effect of guest size and surface charge versus MOF cavity size

may be performed to shed further insights into the nature of guest encapsulation within MOF biocomposites.

7.2.1 Immediate follow-up studies employing SAXS spectra subtraction

Because the SAXS experiments conducted in our work focused on BSA, a model protein, our findings would benefit from applying this approach to the clinically useful TT@ZIF biocomposites we studied in CHAPTER 3. This follow-up study would closely follow the results presented in CHAPTER 4, where the pure ZIF spectra would be scaled and then subtracted from the TT@ZIF spectra to reveal the encapsulated Tetanus Toxoid spectra. The calculated spectra of encapsulated TT would then be compared to the SAXS spectra of free-standing TT. Upon thermal exposure *in situ* for a few hours, we would expect to see denaturation of the free TT with SAXS, while the encapsulated TT spectra would remain unchanged. Presumably, TT encapsulated in ZIFs would be stabilized by the same mechanism as BSA, but there may be variations due to the size differences between BSA (~66 kDa) and TT (~150 kDa).

Further validating the subtraction approach on other ZIF-guest pairs would also shed insights on the robustness of this method; presently, we cannot confidently state that this method can be broadly applied to similar biocomposite systems. In the literature, SAXS studies on MOFs typically examine nucleation and growth behavior, with less emphasis on assessing the structure of the guest molecules [100, 208]. Therefore, *in situ* SAXS studies on ZIF biocomposites composed of several different guests would validate this method and increase its usefulness.

7.2.2 Long-term follow-up studies employing SAXS spectra subtraction

The prevailing hypothesis for the enhanced thermostability afforded by MOF encapsulation is that conformal growth of the framework around a guest molecule prevents unfolding and aggregation. The data we present in CHAPTER 4 supported this hypothesis, but we only examined one guest—BSA. Our studies do not rule out the possibility that guests of different sizes and surface charges are encapsulated (and therefore stabilized) by slightly different mechanisms. Indeed, the work of Liang *et al.* found that the ZIF cavities formed by incorporation of BSA (~66 kDa) were only 17% bigger than the native BSA molecule, whereas ZIF cavities formed around Urease (~600 kDa) were 30% bigger [66]. These results suggest that size and surface properties of guest molecules may impact the tightness of their confinement within ZIF structures.

Therefore, a possible long-term study based on the results presented in our work would center around a series of ZIF biocomposites formed from guests of several different sizes, for example: insulin (~6 kDa), Diphtheria Toxoid (~58 kDa), Pertussis Toxoid (~105 kDa), and Tetanus Toxoid (~150 kDa). This experiment would elucidate the efficacy of the subtraction approach on other biocomposites as well as the effect of guest size on the resulting MOF cavity size, generating further insights into the enhanced thermostability mechanism. As the surface zeta potential has already been identified in literature as an important driver for MOF nucleation and growth around proteinaceous guests, careful studies on the surface charge should also be conducted alongside these SAXS experiments [153]. The effect of surface charge on the degree of conformal MOF encapsulation could then be examined by preparing ZIF biocomposite of various guests with comparable surface charges but varied sizes.

APPENDIX A. SUPPLEMENTARY MATERIALS FOR CHAPTER 3

A.1 Supplementary figure for CHAPTER 3

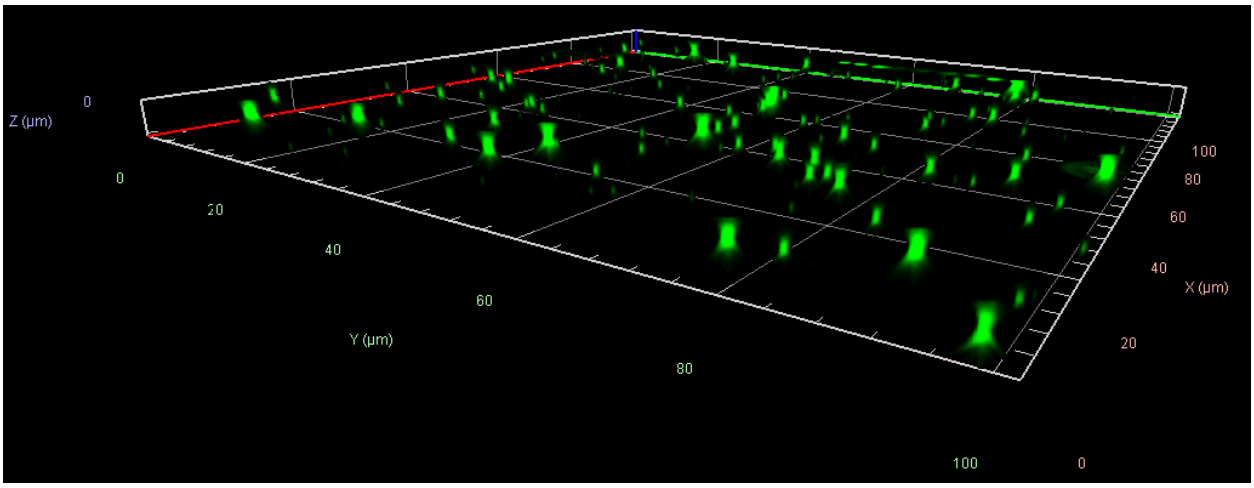

Figure A.1.1: Z-stack image of confocal microscopy on fTT@ZIF crystallites, where Z-axis represents a height of 4 µm.

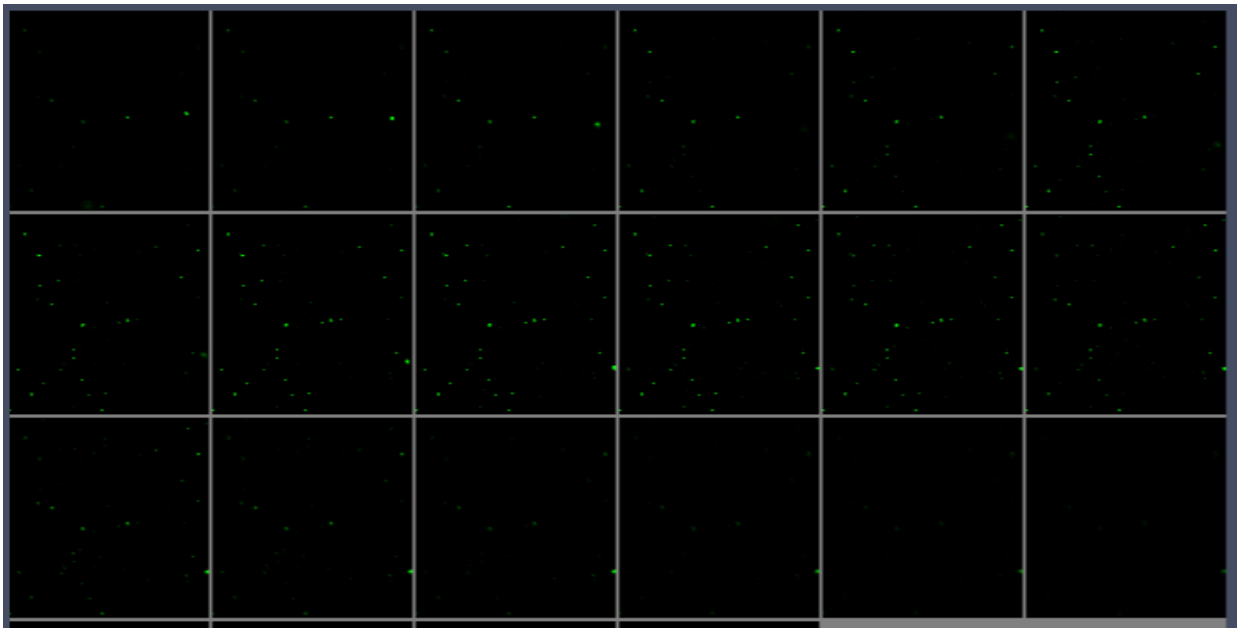

Figure A.1.2: Series of confocal images used to generate fTT@ZIF Z-stack. Each image is spaced 200 µm apart to afford appropriate resolution for 0.5 – 1 µm crystallites.

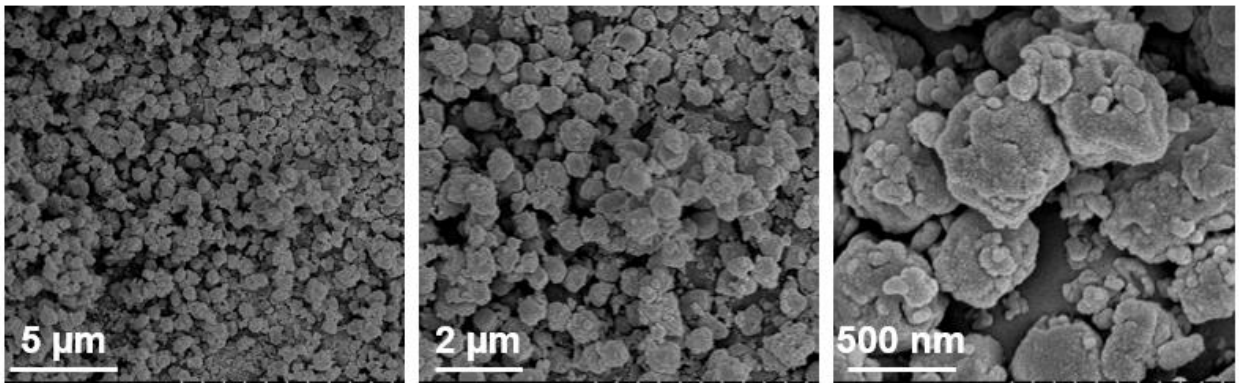

Figure A.1.3: Series of SEM images depicting TT@ZIF crystallites at magnifications of (a) 5,000x, (b) 10,000x, and (c) 50,000x.

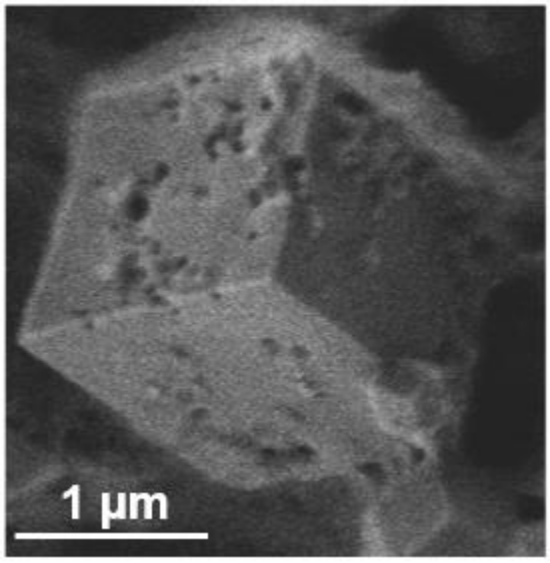

Figure A.1.4: SEM image (30,000x magnification) depicting a single BSA@ZIF-8 crystallite synthesized under the same conditions as Tetanus biocomposites reported here.

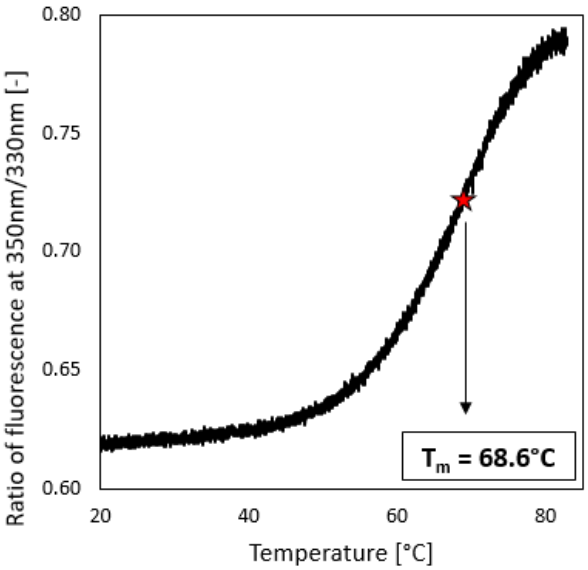

Figure A.1.5: Differential scanning fluorimetry for 10 µM Tetanus Toxoid vaccine. Measured in triplicate with a ramp rate of 1°C/min.

A.2 Raw ELISA data for Figures 3.4 and 3.5

Table A.2.1: Raw ELISA data for liquid samples at 40˚C (Figure 3.4a). Concentrations are shown in units of ng/mL, and each repeat depicts the average reading from 3 ELISA wells.

Days		0	1	3	5	7	14	28	56	84
TT@ZIF (PG/Et)	Rep. 1 (ng/mL)	184.600	189.801	221.784	191.735	194.470	188.130	187.963	182.884	177.513
	Rep. 2 (ng/mL)	202.288	206.056	216.195	198.029	192.497	193.890	191.072	204.111	184.566
	Rep. 3 (ng/mL)	191.652	209.007	193.211	209.704	220.563	186.593	201.640	197.425	174.490
	Mean	192.847	201.622	210.397	199.823	202.510	189.538	193.558	194.807	178.856
	SD	8.905	10.342	15.143	9.118	15.666	3.847	7.169	10.853	5.171

Days		0	1	3	5	7	14	28	56	84
TT@ZIF (H2O)	Rep. 1 (ng/mL)	372.243	392.730	417.884	413.734	360.739	238.141	202.683	124.376	93.585
	Rep. 2 (ng/mL)	502.750	385.426	344.711	402.022	342.391	333.915	255.835	155.715	106.432
	Rep. 3 (ng/mL)	476.144	371.969	355.600	463.674	343.670	292.869	265.160	151.188	103.662
	Mean	450.379	383.375	372.732	426.477	348.933	288.308	241.226	143.760	101.226
	SD	68.963	10.531	39.480	32.741	10.244	48.049	33.704	16.939	6.761

Days		0	1	3	5	7	14	28	56	84
TT (H2O)	Rep. 1 (ng/mL)	2062.116	-	2201.387	2021.520	1963.965	1045.887	389.383	76.902	-
	Rep. 2 (ng/mL)	1971.678	1719.358	-	-	2093.463	1155.099	380.680	118.688	-
	Rep. 3 (ng/mL)	2049.196	1899.216	2007.140	1704.969	-	972.020	329.502	98.538	-
	Mean	2027.663	1809.287	2104.264	1863.245	2028.714	1057.669	366.522	98.043	-
	SD	48.913	127.179	137.353	223.835	91.569	92.106	32.354	20.897	-

Days		0	1	3	5	7	14	28	56	84
TT (PG/Et)	Rep. 1 (ng/mL)	1246.081	50.913	66.656	60.097	62.252	-	-	-	-
	Rep. 2 (ng/mL)	1539.732	49.227	69.561	69.561	64.501	-	-	-	-
	Rep. 3 (ng/mL)	1317.510	55.692	63.470	56.442	60.378	-	-	-	-
	Mean	1367.774	51.944	66.562	62.033	62.377	-	-	-	-
	SD	153.142	3.354	3.047	6.770	2.064	-	-	-	-

Table A.2.2: Raw ELISA data for solid samples at 40˚C (Figure 3.4b). Concentrations are shown in units of ng/mL, and each repeat depicts the average reading from 3 ELISA wells.

Days		0	1	3	5	7	14	28	56	84
TT@ZIF	Rep. 1 (ng/mL)	372.243	446.786	530.733	432.760	366.482	393.943	315.047	343.482	259.368
	Rep. 2 (ng/mL)	502.750	451.179	329.690	538.511	576.395	408.633	394.372	297.704	311.094
	Rep. 3 (ng/mL)	476.144	523.367	443.982	438.105	485.071	473.922	466.858	313.489	317.005
	Mean	450.379	473.777	434.802	469.792	475.982	425.499	392.093	318.225	295.822
	SD	68.963	43.002	100.835	59.573	105.251	42.574	75.931	23.254	31.708

Days		0	1	3	5	7	14	28	56	84
Lyoph. TT	Rep. 1 (ng/mL)	-	1523.250	1197.968	894.690	34.123	0.000	11.243	2.896	-
	Rep. 2 (ng/mL)	1127.904	1047.162	993.077	1073.289	42.252	0.000	57.204	0.000	-
	Rep. 3 (ng/mL)	1322.184	1194.173	1294.118	841.032	55.669	9.093	59.701	1.188	-
	Mean	1225.044	1254.862	1161.721	936.337	44.015	3.031	42.716	1.361	-
	SD	137.377	243.778	153.759	121.601	10.881	5.250	27.285	1.456	-

Table A.2.3: Raw ELISA data for liquid samples at 60˚C (Figure 3.4c). Concentrations are shown in units of ng/mL, and each repeat depicts the average reading from 3 ELISA wells.

Days		0	1	3	5	7	14	28	56	84
TT@ZIF (PG/Et)	Rep. 1 (ng/mL)	184.600	140.073	152.591	149.098	142.257	159.959	174.594	155.056	159.831
	Rep. 2 (ng/mL)	202.288	132.941	162.052	140.655	147.351	165.700	191.244	153.693	158.797
	Rep. 3 (ng/mL)	191.652	152.591	155.939	141.383	149.098	176.853	144.169	-	138.107
	Mean	192.847	141.868	156.861	143.712	146.235	167.504	170.002	154.375	152.245
	SD	8.905	9.947	4.797	4.678	3.554	8.590	23.871	0.964	12.255

Days		0	1	3	5	7	14	28	56	84
TT@ZIF (H2O)	Rep. 1 (ng/mL)	372.243	469.268	326.536	357.937	246.606	265.320	131.626	39.574	32.308
	Rep. 2 (ng/mL)	502.750	379.823	319.875	376.968	349.373	328.583	173.710	42.569	32.497
	Rep. 3 (ng/mL)	476.144	351.276	315.118	437.867	349.373	339.126	168.397	46.380	30.834
	Mean	450.379	400.122	320.510	390.924	315.118	311.010	157.911	42.841	31.879
	SD	68.963	61.560	5.736	41.753	59.333	39.918	22.918	3.411	0.910

Days		0	1	3	5	7	14	28	56	84
TT (H2O)	Rep. 1 (ng/mL)	2062.116	265.368	157.743	113.285	110.233	58.073	2.173	-	-
	Rep. 2 (ng/mL)	1971.678	275.671	136.574	114.438	119.329	52.748	9.351	-	-
	Rep. 3 (ng/mL)	2049.196	283.958	137.929	108.105	116.301	73.090	19.058	-	-
	Mean	2027.663	274.999	144.082	111.943	115.288	61.304	10.194	-	-
	SD	48.913	9.313	11.850	3.373	4.632	10.549	8.474	-	-

Days		0	1	3	5	7	14	28	56	84
TT (PG/Et)	Rep. 1 (ng/mL)	1246.081	75.183	74.434	61.502	80.712	-	-	-	-
	Rep. 2 (ng/mL)	1539.732	68.155	63.189	72.560	74.059	-	-	-	-
	Rep. 3 (ng/mL)	1317.510	69.467	54.568	88.490	75.090	-	-	-	-
	Mean	1367.774	70.935	64.064	74.184	76.620	-	-	-	-
	SD	153.142	3.737	9.962	13.567	3.581	-	-	-	-

Table A.2.4: Raw ELISA data for solid samples at 60˚C (Figure 3.4d). Concentrations are shown in units of ng/mL, and each repeat depicts the average reading from 3 ELISA wells.

Days		0	1	3	5	7	14	28	56	84
TT@ZIF	Rep. 1 (ng/mL)	372.243	366.430	341.561	372.494	344.153	351.660	309.283	228.516	140.566
	Rep. 2 (ng/mL)	502.750	460.457	398.958	400.375	346.827	399.619	288.924	172.385	142.750
	Rep. 3 (ng/mL)	476.144	487.439	335.674	286.152	376.237	322.199	281.510	243.484	145.437
	Mean	450.379	438.108	358.731	353.007	355.739	357.826	293.239	214.795	142.918
	SD	68.963	63.525	34.962	59.552	17.802	39.077	14.381	37.483	2.439

Days		0	1	3	5	7	14	28	56	84
Lyoph. TT	Rep. 1 (ng/mL)	-	70.825	12.130	11.752	6.601	19.441	29.834	-	-
	Rep. 2 (ng/mL)	1127.904	90.201	8.066	16.383	-	25.483	34.892	-	-
	Rep. 3 (ng/mL)	1322.184	73.188	-	-	6.500	20.690	42.497	-	-
	Mean	1225.044	78.071	10.098	14.067	6.550	21.872	35.741	-	-
	SD	137.377	10.571	2.874	3.275	0.071	3.189	6.374	-	-

Table A.2.5: Raw ELISA data for solid samples at 120˚C (Figure 3.5a). Concentrations are shown in units of ng/mL, and each repeat depicts the average reading from 3 ELISA wells.

Days		0	1	3	5	7	14	28	56
TT@ZIF	Rep. 1 (ng/mL)	372.243	103.183	80.048	87.020	89.556	49.233	61.656	0.000
	Rep. 2 (ng/mL)	502.750	81.950	89.556	-	99.538	57.541	81.914	0.000
	Rep. 3 (ng/mL)	476.144	84.802	99.697	-	79.256	46.997	63.699	0.000
	Mean	450.379	89.978	89.767	87.020	89.450	51.257	69.089	0.000
	SD	68.963	11.524	9.826	-	10.142	5.556	11.153	-

Table A.2.6: Raw ELISA data for freeze/thawed samples (Figure 3.5b). Concentrations are shown in units of ng/mL, and each repeat depicts the average reading from 3 ELISA wells.

Cycles		**0**	**1**	**3**	**5**
TT@ZIF (Frozen)	Rep. 1 (ng/mL)	109.919	108.217	116.236	109.707
	Rep. 2 (ng/mL)	104.675	107.803	110.080	114.557
	Rep. 3 (ng/mL)	106.499	106.766	108.588	115.676
	Mean	107.031	107.595	111.635	113.313
	SD	2.662	0.747	4.054	3.173

A.3 SOP for MOF Biocomposite Synthesis, Exfoliation, and ELISA

A.3.1 Synthesis and wash of TT@ZIF Biocomposite

Suppliers and purities for all materials are listed on page 30. To synthesize TT@ZIF, first prepare solutions of the ligand 2-methyl imidazole and the metal zinc (II) acetate dihydrate. The 160 mmol ligand solution is prepared by adding 262.7 mg of the ligand to 20 mL DI H_2O and the 40 mmol metal solution is prepared by adding 175.6 mg of the metal to 20 mL DI H_2O. All solutions are prepared in 50 mL polypropylene centrifuge tubes from Corning (NY, USA). Once the ligand is fully dissolved, add 1 mL of 10 mg/mL Tetanus Toxoid stock solution and agitate gently. After 3 minutes, add metal solution to the ligand/protein solution to start TT@ZIF growth. Solution will immediately turn cloudy; agitate gently for 1 minute and then let reaction rest for 16 hours at room temperature.

After reaction has run, centrifuge the 50 mL Corning tube at 3.0 RCF for 10 minutes and discard supernatant. For surface washing, add 4 mL of DI H_2O to solids and agitate vigorously to fully suspend crystallites. Sonicate the centrifuge tube at room temperature (in Branson 5800 sonication bath) for 10 minutes. Next, centrifuge again at 3.0 RCF for 10 minutes and decant supernatant. Repeat this process once more with 4 mL H_2O, and twice more using 4 mL Reagent Ethanol. Once wash steps are complete, leave TT@ZIF pellet to dry at room temperature for several days to allow full evaporation of solvents. Finally, mass resulting pellet and store with desiccant in fridge to maximize stability.

A.3.2 Exfoliation of ZIF to Release TT

Exfoliation is done with 0.1 M EDTA solution (pH 7.0). To prepare this solution, add 1.461 g of EDTA (MW = 292.24 g/mol) to 50 mL DI H_2O while stirring and measuring pH with a probe; the solution will still be cloudy at this point. Add NaOH pellets (VWR Chemicals BDH) half a pellet at a time until solution turns clear (pH ~ 8.0). Then, use 6 M HCl to adjust pH back down to 7.0. Store in fridge for up to one year.

To exfoliate TT@ZIF, prepare a 1 mg/mL solution of TT@ZIF in DI H_2O in a 7.5 mL borosilicate glass scintillation vial (Qorpak, Clinton, PA, USA). Add 62 µL of the 0.1 M EDTA solution per 1 mg of TT@ZIF (*e.g.*, add 93 µL EDTA to 1.5 mg TT@ZIF in 1.5 mL of water). For best results, allow samples to exfoliate for 24 hours at room temperature and agitate frequently to ensure that all particles are in contact with the liquid. After 24 hours, dilute samples by 50x in 1x PBS-T buffer to measure with ELISA.

A.3.3 Measuring TT concentration with competition ELISA

The ELISA plate (Nunc, Microwell, 96-well Microplate by Thermo Fisher), must first be coated with TT antigen. A 0.05 M Carbonate coating buffer should be prepared by adding 79.5 mg Na_2CO_3 (Sigma-Aldrich) and 146.5 $NaHCO_3$ (Sigma-Aldrich) to 50 mL DI H_2O in a Corning centrifuge tube. Agitate vigorously until fully dissolved. Then, add 2 µL of 10 mg/mL TT stock solution to 10 mL carbonate buffer and use this to coat the plate with 100 µL per well. To allow binding of antigen to the plate surface, allow overnight (12 – 16 hour) incubation at 4˚C. The next day, use SmartWasher 96 Microplate Washer (Accuris, Dublin, Ireland) plate washer to wash plate with 300 µL 1x PBS-T three times. If not immediately adding samples to antigen-coated plate, add 250 µL PBS-T and store at 4˚C.

Next, create a standard dilution series by preparing a 2000 ng/mL solution of TT in PBS-T by diluting the 10 mg/mL TT stock solution 5,000x in PBS-T. This can be achieved by adding 10 µL TT stock to 990 µL PBS-T, then taking 20 µL of this solution and adding it to 980 µL PBS-T. This resulting 2000 ng/mL TT solution is Standard 1. Standards 2 – 7 are prepared by adding 500 µL of the previous standard to 500 µL PBS-T (*i.e.*, Standard 2 is 1000 ng/mL, Standard 3 is 500 ng/mL, *etc.*). Standard 8 should be pure PBS-T. The resulting calibration curve should appear like the image below:

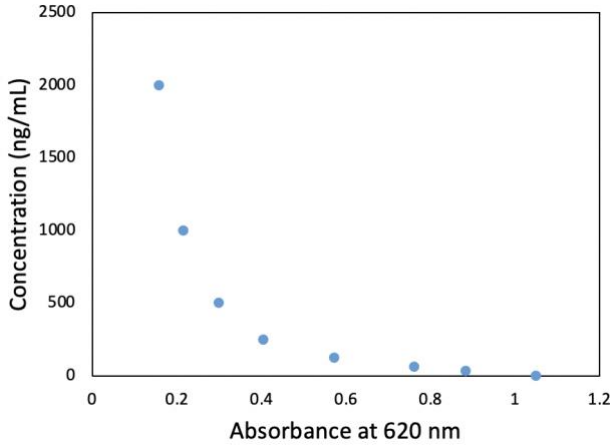

Once standards have been prepared, dilute exfoliated TT@ZIF samples in PBS-T to the appropriate range; most often, this entailed adding 100 µL of the exfoliated solution to 5 mL of PBS-T. Next, dilute 100x Anti-Tetanus Toxoid HRP conjugate Antibody (Alpha Diagnostic International) by 250x in PBS-T. To calculate amount of Antibody solution needed, multiply the total number of plate wells by 55 µL. Prepare the competition step by adding 165 µL of standard or sample solution to 165 µL of the diluted antibody solution into 0.65 mL microcentrifuge tubes (VWR). Vortex each microcentrifuge tube for 5 – 10 seconds to ensure adequate mixing. At the same time, block the antigen-coated plate with 250 µL PBS-T per well. Incubate all microcentrifuge tubes and blocked plates at 37˚C for

1 hour. Then, add 100 µL of the combined antibody + sample/standard solution to each plate well. Allow the plate to incubate at 4˚C for 18 hours.

Once the plate has incubated for a sufficient time, wash the plate 6x with 300 µL PBS-T. Add 100 µL of the KPL SureBlue TMB Microwell Substrate per well and incubate at room temperature in the dark for 20 minutes. If the blue color is not fully developed, place plate in 37˚C incubator for no more than 3 minutes. Once color has developed, add 100 µL of the KPL TMB BlueSTOP solution (Seracare) to each plate well. Finally, measure absorbance at 620 nm with the iMark Microplate Absorbance Reader (Bio-Rad, Hercules, CA, USA) and use calibration curve to calculate sample concentrations.

APPENDIX B. SUPPLEMENTARY MATERIAL FOR CHAPTER 4

B.1 Supplementary figures for Chapter 4

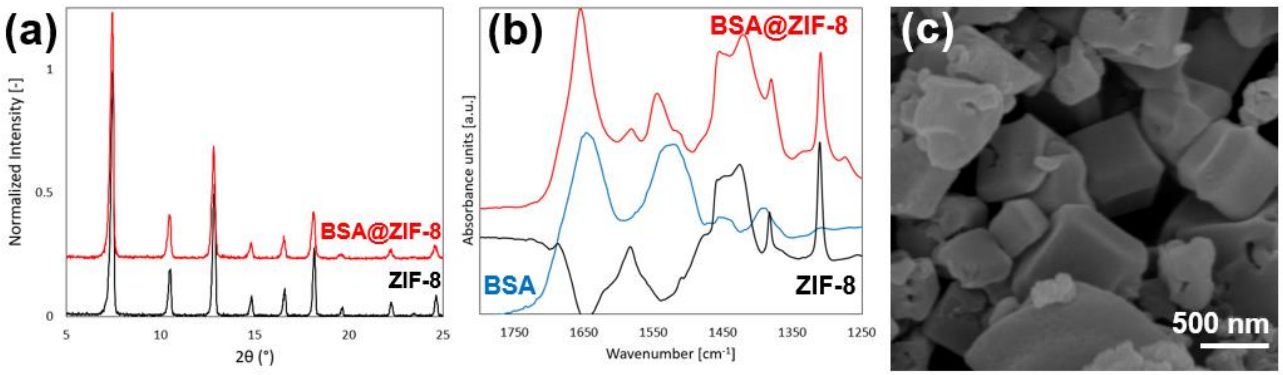

Figure B.1.1: Characterization of BSA@ZIF-8 biocomposites. Representative XRD spectra of (a) BSA@ZIF-8 showing biocomposite (red) and MOF (black). Representative FTIR spectra of (b) BSA@ZIF-8, showing biocomposite (red), lyophilized BSA (blue), and MOF (black). Representative SEM image of (c) rhombic dodecahedra BSA@ZIF-8 crystallites at 30,000x zoom, where scale bar represents 500 nm.

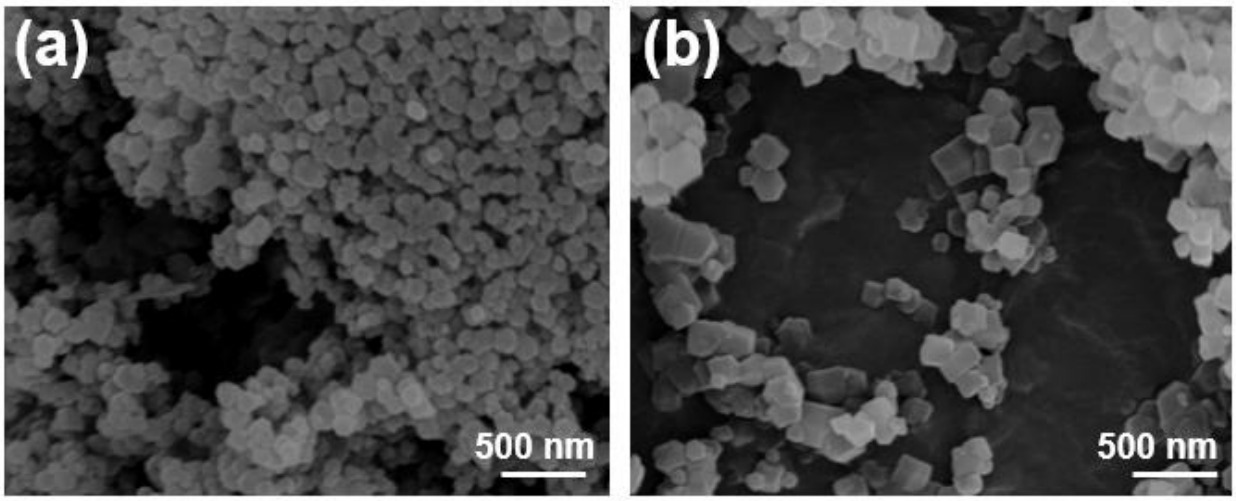

Figure B.1.2: Representative SEM images of (a) pure ZIF-67 crystallites and (b) pure ZIF-8 crystallites. Both images were taken at 30,000x magnification and scale bars represent 500 nm.

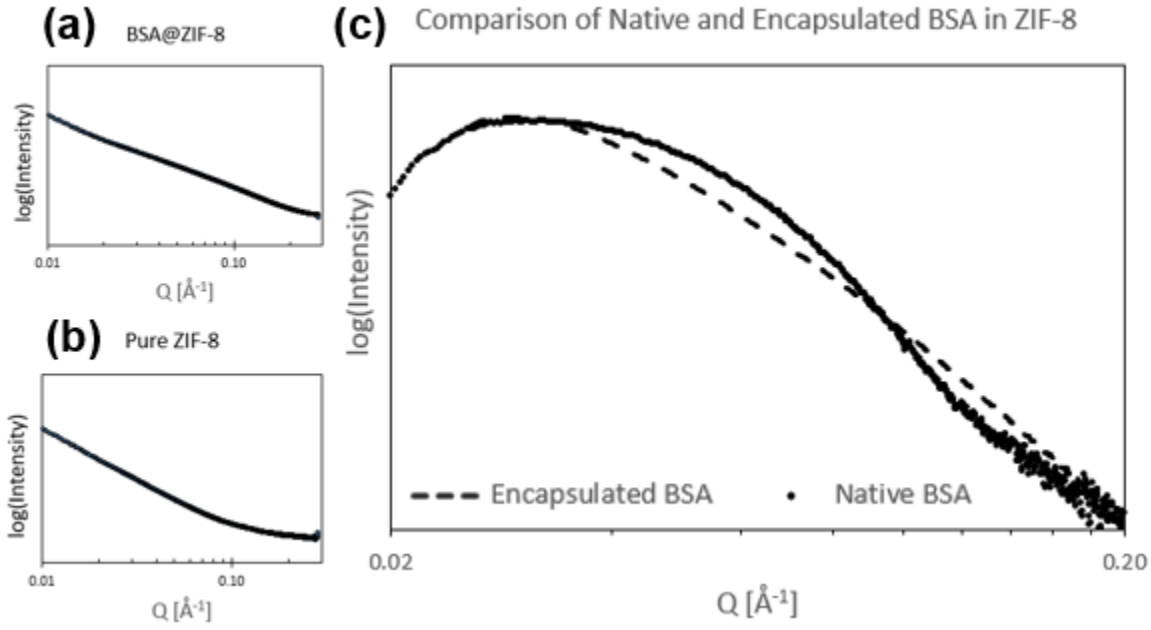

Figure B.1.3: Representative SAXS intensity spectra showing scaled spectra subtraction to reveal encapsulated BSA in ZIF-8 biocomposite. Log-log scale graphs are shown for (a) BSA@ZIF-8, (b) ZIF-8, and (c) native or encapsulated BSA. Spectra for encapsulated BSA (graph c) were generated by subtracting the ZIF-8 (graph b) spectrum from the BSA@ZIF-67 (graph a) spectrum, and compared to native BSA that was never encapsulated in MOF. Q-range is shown from 0.01 $Å^{-1}$ – 0.20 $Å^{-1}$. BSA@ZIF-8 and BSA@ZIF-67 were prepared at BSA:MOF ratios of 4:1 in HEPES buffer. The native BSA was prepared at a concentration of 4 mg/mL in HEPES buffer.

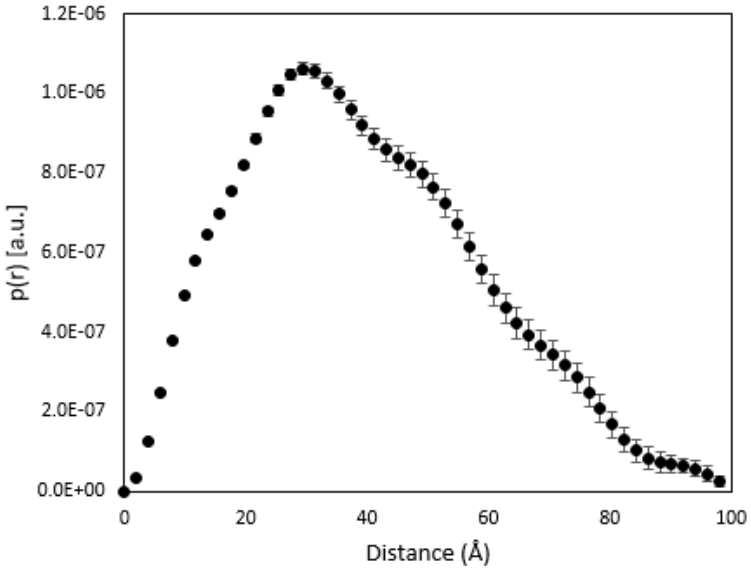

Figure B.1.4: Representative PDDF for calculated spectra of BSA encapsulated in ZIF-8 at 23°C. An R_g value of 31.2 Å was calculated from the PDDF. This represents successful spectra subtraction, as both the PDDF and R_g values match those of native BSA.

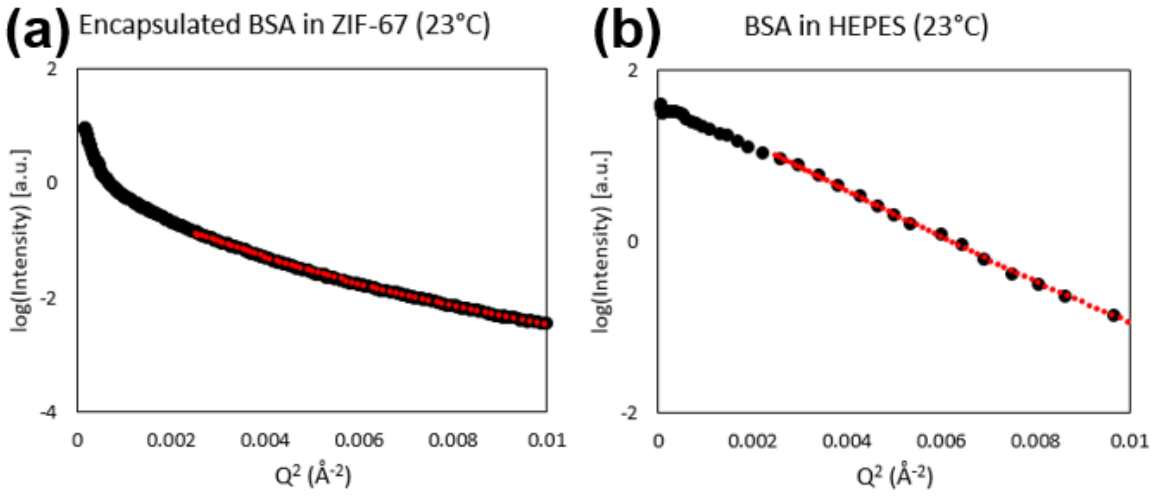

Figure B.1.5: Representative Guinier approximations (red) on SAXS spectra (black) of (a) BSA encapsulated in ZIF-67 and (b) native BSA in HEPES buffer taken at room temperature.

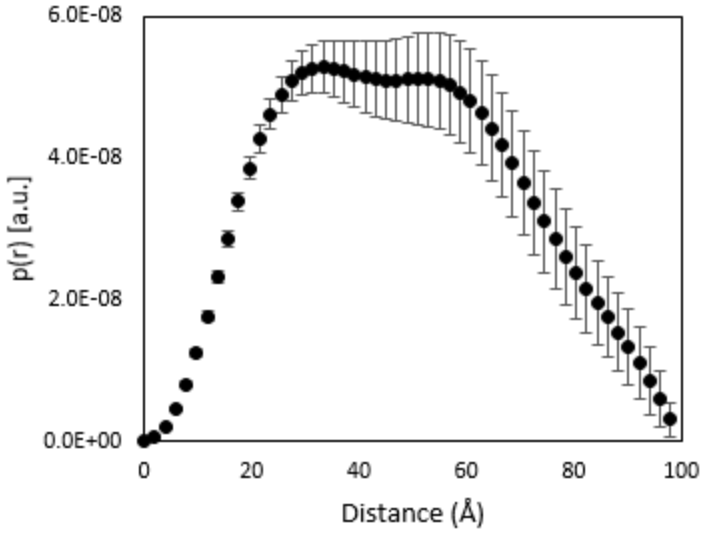

Figure B.1.6: Representative PDDF from calculated spectra of a physical mixture of BSA and ZIF-67 prepared at a BSA:MOF ratio of 1:9 (10% BSA). Predicted R_g value from PDDFs was 37.3 Å. This result is inconsistent with successful subtraction as the globular PDDF shape is not observed, nor is the R_g value consistent with native BSA.

B.2 Mathematical justification for scaling subtraction factor

Although we adopted a trial-and-error approach for determining $\boldsymbol{\alpha}$ in this work, we also propose a mathematical basis for this scaling subtraction factor:

$$I_1 = \phi_1 I_p + \phi_2 I_m + [1 - (\phi_1 + \phi_2)] I_s$$

$$I_2 = \phi_3 I_m + (1 - \phi_3) I_s$$

$$\phi_1 I_p + (1 - \phi_1 - \alpha I_s) = I_1 - \boldsymbol{\alpha} I_2$$

Here, the first equation represents the scattered intensity from proteins within the MOF and the solvent. Here, I_p, I_m, and I_s are the scattered intensity contributions from proteins, MOF, and solvent, respectively, while ϕ_1 and ϕ_2 are the volume fractions of proteins and MOF in the scattering volume of the capillary tube. Similarly, the scattered intensity from the MOF suspended in solvent is determined by the second equation, where

ϕ_3 is the volume fraction of MOF in the scattering volume. By combining the first two equations and performing algebraic manipulation, we arrive at the third equation, from which it is apparent that ϕ_1 is needed to obtain the actual scattering contribution from only the protein.

We do not have information about the volume fraction of the proteins in the scattering volume. Hence, without $\phi_1$we cannot separate the solvent background totally from the scattering contributions from proteins. While the proposed subtraction approach can remove the MOF scattering contribution, it cannot guarantee removal of the solvent scattering. In practice, we consider the solvent contribution to be relatively constant, and therefore treat it as a constant background on all analyses [44, 45]. Nonetheless, we predict that by knowing the volume fraction of each component in the scattering volume, the scaling subtraction factor $\boldsymbol{\alpha}$ could be determined mathematically with the third equation presented here.

APPENDIX C. ANGLED INSERTION OF MICRONEEDLES FOR TARGETED ANTIGEN DELIVERY TO THE EPIDERMIS

C.1 Abstract

Peanut and tree nut allergies account for most food-induced anaphylactic events. The standard allergy immunotherapy approach involves subcutaneous injection, which is challenging because severe adverse reactions can occur when antigens spread systemically. Allergen localization within the epidermis (*i.e.,* the upper 20–100 μm of skin) should significantly reduce systemic uptake, because the epidermis is avascular. Microneedle (MN) patches provide a convenient method for drug delivery to the skin, but they generally target both epidermis and dermis, leading to systemic delivery. In this study, we adapted MN technology for epidermal localization by performing angled insertion of 250 μm–long MNs that limits MN insertion depth mostly to the epidermis. We designed a biplanar insertion device to aid the repeatability of angled insertions into porcine skin ex vivo at specified angles (90°, 45°, and 20°). When compared to 90° insertions, MN application at 20° decreased mean insertion depth from 265 ± 45 μm to 97 ± 15 μm. Image analysis of histological skin sections revealed that acute-angle insertion increased epidermal localization of delivery for antigen-coated MNs from 25% ± 13% to 70% ± 21%. We conclude that angled insertion of MNs can target antigen delivery to epidermis.

C.2 Introduction

Peanut allergies affect 1–2% of adults and 4–8% of children [209-211]. Furthermore, current evidence suggests that the prevalence of food allergies in the Western world has

been increasing over the last few decades [209, 212]. Peanut or tree nut ingestion/contact causes most severe food-induced reactions [211], accounting for more than 24,000 food-induced anaphylactic events in the United States annually [209].

Typical methods for treating peanut allergies include subcutaneous allergen immunotherapy (SCIT) [213] and oral immunotherapy (OIT) [214]. These immunotherapies are based on extended exposure of the immune system to low doses of antigen in order to induce immunological tolerance to the antigen, thereby suppressing allergic responses. SCIT is often cumbersome, as subcutaneous injection (Figure C.1a) of antigens, such as *Arachis hypogaea 2*—the dominant peanut allergen [215]—can cause severe adverse effects in patients [213, 216]. Additionally, young children suffer from needle phobia at a rate of up to 60–70% [217]. While OIT avoids injections, it is still in relatively early development and is hindered by patients' increased risk of anaphylaxis and gastrointestinal discomfort, leading to withdrawal from treatment and, thus, resulting in the rapid reversal of allergen desensitization [214, 218, 219]. In recent years, topical immunotherapies that avoid the issues of needle phobia and gastrointestinal adverse effects have emerged (*e.g.,* Viaskin by DBV Technologies, Bagneux, France), but they generally suffer from poor efficacy and regulatory barriers [220, 221].

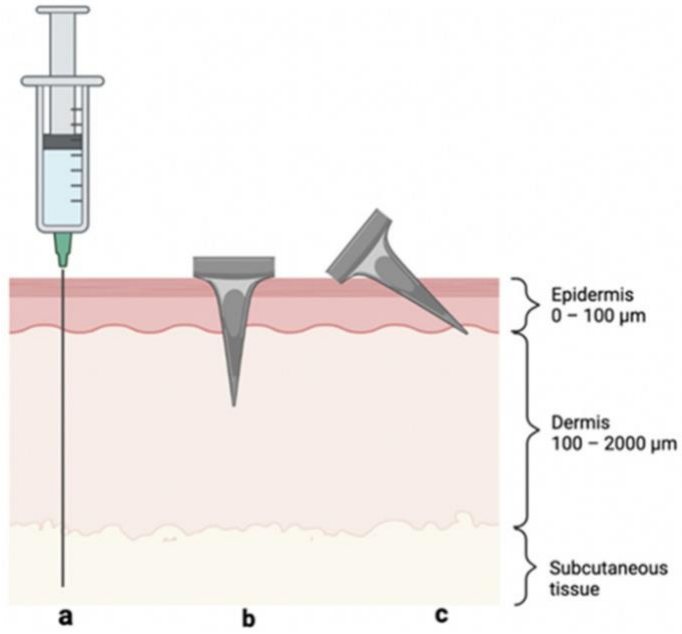

Figure C.1: Visual representation of skin layers and three methods of antigen delivery: (a) hypodermic needle injection to the subcutaneous space, (b) perpendicular (*i.e.*, 90°) MN insertion crossing epidermis and into the dermis, and (c) angled MN insertion targeting the epidermis.

Adverse effects stemming from SCIT are caused by systemic uptake into the bloodstream and rapid antigen clearance by macrophages in the dermis and subcutaneous space. These processes increase the production of IgE antibodies, causing mast cells to flood the system with histamines; in extreme cases, this may result in anaphylaxis. In contrast, delivery to the avascular epidermis reduces systemic uptake, thereby increasing the relative production of IgG_4 antibodies—*i.e.*, those responsible for immune tolerance [222-224]. Consequently, both the safety and efficacy of targeted allergen immunotherapy within the skin may be improved by localizing the antigen in the epidermis, ideally without requiring a hypodermic needle, as this would significantly decrease the rate of systemic uptake, elicit the desired immune response, and address needle-phobia concerns [225] (Figure C.1).

In this study, we proposed that microneedle (MN) patches may provide an effective approach of targeting antigen delivery to the epidermis. MNs are micron-scale needles that enable delivery to the skin without the need for hypodermic needle injection. Since their genesis in the 1990s, methods for fabrication, coating, and application of MNs have emerged, affording drug, vaccine, and allergen delivery [128, 226-229]. For instance, vaccine-coated MN patches were successfully used to prevent the development of airway asthma in mice, suggesting promise for human translation [230]. MN patch administration of drugs for osteoporosis treatment, insulin, and inactivated influenza vaccine, among other therapeutics, has been successfully studied in human clinical trials [231, 232].

MN patches assuage many of the translational barriers associated with SCIT [227]; their size/geometry provides an attractive opportunity for targeting antigen delivery to epidermal thicknesses (~100 μm) [233], and administration in the form of an MN patch bypasses the issue of needle phobia. Until now, most reports of MN patches for drug delivery involve delivery to both the epidermis and dermis (Figure C.1b), and this is undesirable for allergy immunotherapy [234, 235]. Limiting MN penetration depth by using MNs shorter than epidermis thickness is difficult for this application for two reasons: (i) antigen loading on such small MNs may be too low to deliver the required dose and (ii) controlled insertion of such short MNs is difficult to achieve without a specialized high-velocity insertion device [236, 237].

To address these challenges, we introduce angled insertion of MNs to target antigen delivery to the epidermis (Figure C.1c). In this way, we can use moderate-sized MNs (*i.e.*, 250 μm long) that have a limited skin penetration depth due to angled insertion. Because previous epicutaneous (“on the skin”) immunotherapy (EPIT) studies have administered

50–500 µg of antigen topically [238], we decided on a maximum total target dose of 50 µg, which is probably even more than epicutaneous delivery produces in the skin, given the low expected bioavailability of topical protein delivery [239]. By assuming a patch size of 100 MNs, we defined the antigen loading target as 0.5 µg/MN, which should be suitable for inducing allergic tolerance to peanuts [223].

C.3 Materials and methods

C.3.1 Microneedle coating

Solid stainless-steel MN arrays were constructed by using wet-etching photo-lithographically defined needle structures from stainless-steel sheets (Tech Etch, Plymouth, MA or Moonlight Therapeutics, Atlanta, GA, USA). Each MN array consisted of five co-planar MNs, each measuring 250 µm in length. Prior to coating, MNs were treated with oxygen plasma (Plasma Cleaner PDC-32G, Harrick Plasma, Ithaca, NY, USA) to increase the steel surface's hydrophilicity and improve coating-solution adhesion. The aqueous coating solution consisted of 2% (*w*/*v*) medium-viscosity carboxymethylcellulose sodium salt (Sigma-Aldrich, St. Louis, MO, USA) and 0.5% (*w*/*v*) Pluronic F-68 (Sigma-Aldrich). When indicated, the coating solution also contained 2% (*w*/*v*) peanut *Arachis hypogaea* (Greer Laboratories, Lenoir, NC, USA) and/or 0.2% (*w*/*v*) sulforhodamine B sodium salt (Sigma-Aldrich) as a red-fluorescent dye.

The coating solution was prepared by adding 20 mg medium viscosity CMC and 5 mg Pluronic F-68, as well as 10 mg peanut protein and/or 2 mg sulforhodamine B dye in some cases, to 1 mL deionized (DI) water; this solution was then mixed via vortexing and sonication. Next, MN arrays were mounted onto a custom-made automated dip-coating

device [240] through which the MNs were dip-coated in the coating solution, using two-axis robotic control. Each MN in the array was coated 10 times, following a procedure described previously [241]. Arrays were air-dried and stored at ambient conditions (20–25 °C, 30–60% relative humidity) before insertion into skin. The amount of antigen coated onto each MN was determined by dissolving the MN coating in DI water and measuring antigen concentration by bicinchoninic acid assay [242].

C.3.2 Angled Insertion Device

To facilitate insertion of MNs into skin at a controlled angle, we developed a biplanar insertion device with an adjustable angle of elevation that was designed by using computer-aided design (CAD) software (SolidWorks, Vélizy-Villacoublay, France) and fabricated out of poly(lactic acid) (ColorFabb, Belfeld, Netherlands) by a 3D-printer (Ultimaker 3, Zaltbommel, Netherlands). The two faces of the applicator hinged around a bolt; once the desired angle was selected by rotating the angled surface, a nut was tightened around the bolt to fix the device angle in place. A single planar MN array (containing 5 MNs) was taped to the edge of a flat piece of plastic and slid down the angled face for insertion.

We used angled wedges to control the angle of insertion of the MNs into skin during real-time imaging by optical coherence tomography (OCT). We designed these wedges by using CAD software (SolidWorks) and fabricated them by using a Form 3 printer (Formlabs, Somerville, MA, USA). The wedges were made of Grayscale resin (Formlabs). After printing, the wedges were cured in a Form Cure chamber (Formlabs). We inserted the MNs by using forceps to slide the MNs over the wedge and into the skin.

C.3.3 Insertion of Microneedles into Porcine Skin Ex Vivo

Porcine belly skin was obtained from Pel-Freez Biologicals, (Rogers, AR, USA), and the subcutaneous fat layer was removed. The skin surface was dabbed with Kim wipes (to remove excess moisture) and then fixed tautly onto a cutting board to simulate natural skin tension during MN insertion. The MNs were pressed into the skin for 30 s and then removed. Perpendicular insertions (90° angle) were performed by hand.

Angled insertions (45° and 20°) were executed by using the biplanar insertion device with an adjustable angle of elevation. To insert MNs into skin, the MN array was slid down the plane of the insertion device (fixed at the desired angle) to the skin surface, where the MNs penetrated the skin for 30 s. The MNs were then removed from the skin at the same angle.

C.3.4 Histological Analysis

Immediately after insertion, the tissue around the MN array insertion site was excised and prepared for histological sectioning by freezing in liquid nitrogen for 1–2 min in Optimal Cutting Temperature Embedding Medium for Frozen Tissue Specimens (Scigen Scientific, Gardena, CA, USA). The angle of insertion was also marked on the outside of the block for guidance during sectioning before being stored at −20 °C until sectioning. Because small-molecule dye diffusion happens on the timescale of minutes (and the large protein diffuses much slower), we did not expect significant diffusion of the antigen away from the MN insertion site.

Within minutes (or hours at most), histological analysis was conducted to assess MN insertion depth into the skin and image distribution of materials dissolved from the MN coatings in the skin. Samples were sectioned to 10–15 μm thickness by using a Leica 3050 S Cryostat (Wetzlar, Germany), with 3–5 sections being collected for each of the five insertion sites imprinted by each MN array.

Frozen sections were imaged by using a stereo microscope (Olympus SZX16, Tokyo, Japan) with red fluorescence to visualize and quantify the depth of delivery of sulforhodamine. The Autostainer XL (Leica) was used to stain sections with hematoxylin and eosin (H&E), which were then imaged by using the same microscope under bright field to determine the extent of epidermal localization.

C.3.5 Optical Coherence Tomography

MNs inserted into skin were imaged in real time by using OCT (VivoSight Dx, Michelson Diagnostics, Kent, UK) with infrared light (1305 nm) to visualize to skin depths up to 500 μm from the skin surface. The OCT scan was configured to produce 500 slices of a 6 mm × 6 mm section of the skin.

C.3.6 Statistical Analysis

Statistical analysis was performed by using OriginPro 2021b software (Northampton, MA, USA). One-way ANOVA tests were used to evaluate statistical differences between the groups for insertion depth, percent epidermal targeting, and percent peanut antigen localization in the epidermis. Significance was considered for $p < 0.05$.

C.4 Results

C.4.1 Coating Microneedles with Peanut Protein Antigen

The eventual intended application for angled MN insertions in this work is to induce tolerance to peanut and other food allergens. Consequently, we first developed a formulation and method for coating a suitable dose of peanut antigen on MN arrays. Four factors were varied to meet the target antigen loading of 0.5 µg per MN: concentration of peanut protein and CMC in the coating solution, MN length, and number of dip-coating cycles.

The aqueous coating solution consisted of the peanut protein, CMC, and Pluronic F-68. While the Pluronic concentration was kept constant at 0.5% (*w*/*v*), the antigen concentration was varied from 1% to 3% (*w*/*v*), and the CMC concentration from 1% to 2% (*w*/*v*). Increasing protein concentration from 1% to 2% nearly doubled the amount of antigen loading (to ~0.6 µg/MN), but higher concentrations did not significantly improve the loading (Figure C.2a). We did not pursue protein concentrations above ~2%, because they formed a highly viscous, hard-to-mix coating solution that yielded unreliable coating results (data not shown). For CMC, a 2% (*w*/*v*) concentration afforded a greater antigen loading compared to 1% (*w*/*v*), probably because the increased coating solution viscosity kept more coating solution on the MN surface during drying (Figure C2.b).

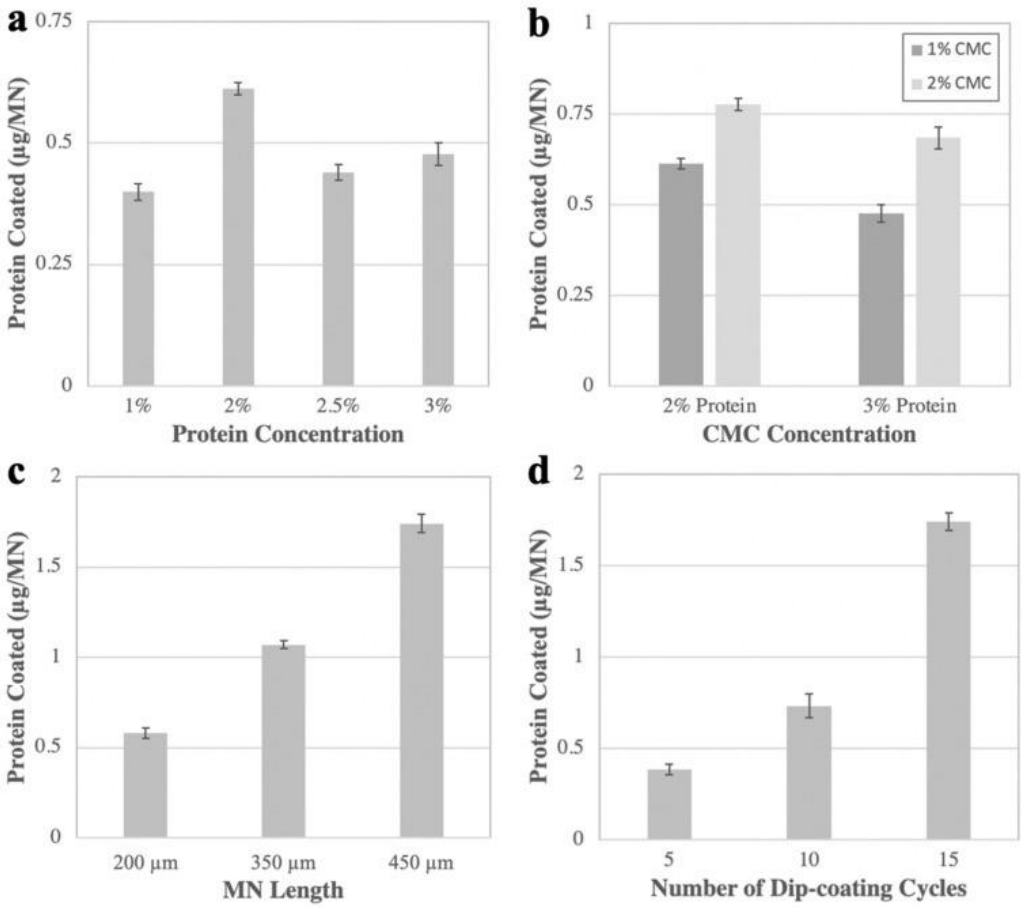

Figure C.2: Optimization of MN coating with peanut protein antigen. The mass of protein coated is shown as a function of (a) protein concentration, (b) CMC concentration (varying from 1% to 2%, (c) MN length, and (d) number of dip-coating cycles. Unless otherwise specified, 450 µm–long MNs underwent 15 coating cycles in a solution of 2% protein, 2% CMC, 0.5% Pluronic acid w/v. Graphs show mean and standard deviation for 6 replicates.

We found that varying MN length from 200 to 450 µm caused a 250% increase in total antigen coating (Figure C.2c). Because longer MNs could be coated with more antigen and 200 µm–long MNs met the loading target of 0.5 µg/MN, we concluded that 250 µm–long MNs would also achieve sufficient loading, as well as expected skin insertion.

We also found that increasing the number of dip-coating cycles from 5 to 15 caused a >200% increase in antigen loading (Figure C.2d). However, we noted that adding more

dip-coating cycles increased the likelihood of antigen coating below the base of the MN (Figure D.1). This is not desirable, because any coating not on the MNs themselves will not enter the skin upon insertion. As such, we employed 10 coating cycles, since this resulted in sufficient antigen loading, while mitigating the frequency of coating past the base.

Our optimized coating method employed a formulation containing 2% (W/V) CMC, 0.5% (W/V) Pluronic F-68, 1% (W/V) peanut antigen, and 0.2% (W/V) sulforhodamine B (to assist coating visualization) that was coated onto 250 µm–long stainless-steel MNs, using 10 dip-coating cycles. Because the target dose was achieved with 1% peanut antigen, we used that concentration instead of higher concentrations; however, as long as changes to the formulation do not hinder the solution's ability to coat uniformly on MN tips (*e.g.*, by becoming too viscous), varying either the CMC or protein amount should not affect epidermal targeting. Although 250 µm MNs were not specifically studied in these coating experiments, we determined that 200 µm MNs were long enough to achieve the target loading, so any MN equal or greater in length would be sufficient from a dosing perspective. When considering insertion, however, 250 µm MNs were superior, as we found that reliable insertion of 200 µm (or shorter) MNs was difficult to achieve. Thus, our final MN array was selected to be long enough to achieve the target dose and insert reliably at shallow angles, while being short enough not to penetrate too far into the dermis.

While polymeric MNs were considered for this study's immunotherapy applications (as they may have enabled greater antigen loading), we ultimately decided against this approach, as higher loading was not necessary past the 0.5 µg/MN target.

Furthermore, polymeric MN patches may lack the rigidity required to insert consistently at a shallow angle, which was facilitated by the strength/sharpness of metal MNs.

C.4.2 Device for Angled Microneedle Insertion into Skin

Our hypothesis is that angled insertion of MNs into the skin enables more superficial delivery that targets antigen deposition in the epidermis compared to perpendicular MN insertion. While perpendicular insertion of MNs into tissue can be performed reliably by hand, angled MN insertions are more difficult to control. We therefore designed and built a biplanar insertion device that enabled control over MN insertion angle into the skin (Figure C.3).

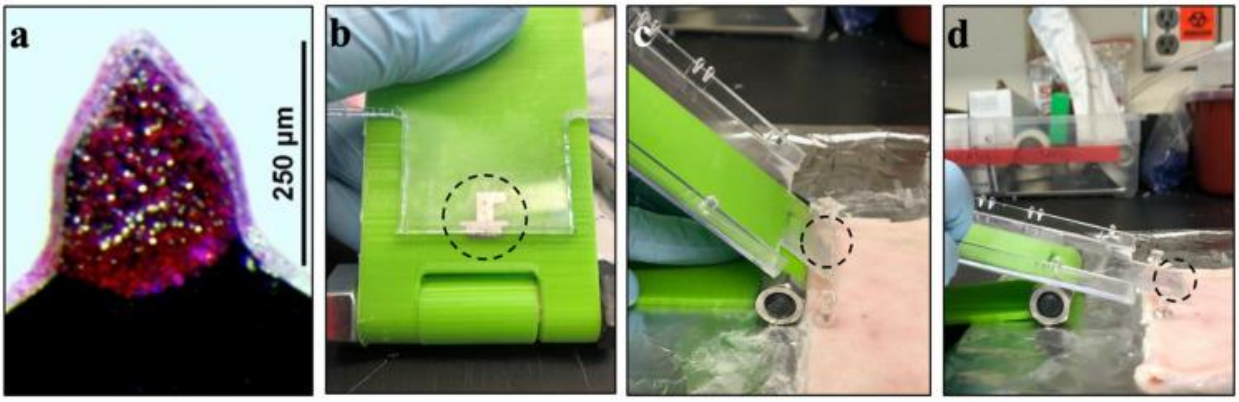

Figure C.3: Device for angled MN insertion. (a) Representative MN coated with peanut protein and sulforhodamine B dye to facilitate imaging; (b) biplanar insertion device with MN array (circled) attached to solid surface that slides at a predetermined angle; and (c,d) device used to insert MN array into pig skin ex vivo at 45° and 20°, respectively.

The insertion device system had three components: the device itself, a plastic substrate, and a single MN array. First, we 3D-printed a biplanar device (*i.e.*, two sheets of plastic connected by a hinge) that could be fixed at a specified angle by tightening a nut and screw at the rotating axis (Figure C.3b). We then mounted a MN array onto the plastic

substrate that could slide on the surface of the insertion device, thereby bringing the MN array to the skin surface at the predefined angle (Figure C.3c,d). Although only three insertion angles are reported in this work, this device afforded angular control from 90° to 5°, with respect to the tissue surface.

C.4.3 Microneedle Insertion Depth into Skin after Angled Insertion

To limit MN insertion depth primarily to the epidermis (20–100 μm thick in humans [233], we combined two strategies. First, we used short MNs of 250 μm length. We did not use MNs shorter than 250 μm, because we found that shorter MNs did not reliably insert into skin, but often just deformed the skin surface without penetration (data not shown). Second, we inserted the MNs at an angle. In this study, we used angles of 90°, 45°, and 20°. By geometry, these MNs are expected to insert 250 μm, 177 μm, and 85 μm into the skin (*i.e.*, insertion depth (D) equals MN length (L) times the sin of the insertion angle (θ), $D = L \sin \theta$).

Histological analysis of MN insertions showed that MN insertion depth decreased with decreasing insertion angle (one-way ANOVA, $p < 0.001$) (Figure C.4). As expected for perpendicular insertion, the mean depth was 265 ± 45 μm, which is not significantly different from the MN length of 250 μm (within 95% confidence interval of 230–300 μm, Figure C.4a). After perpendicular insertion, deformation of the skin surface was evident, with the MN insertion site located at the base of a valley on the skin surface, which is consistent with prior reports [243].

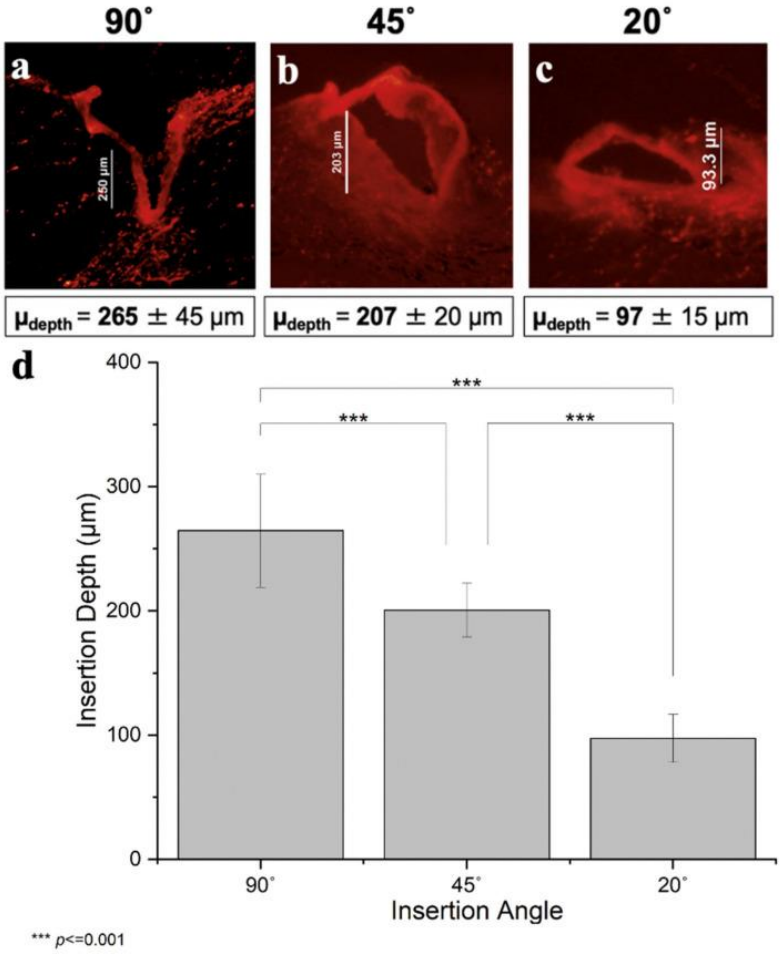

Figure C.4: Microneedle insertion depth into skin after angled insertion. MNs measuring 250 µm in length were inserted at various angles into porcine skin ex vivo. Representative images of histological skin sections after insertion of MNs coated with red-fluorescent sulforhodamine dye at angles of (a) 90°, (b) 45°, and (c) 20°. Insertion depth was determined by measuring the distance from the skin surface to the tip of MN penetration into skin at the greatest depth seen in serial sections at each insertion site. (d) Mean and standard deviation of insertion depth after angled MN insertion for 9 replicates.

The decrease in insertion depth caused by an insertion angle of 45° yielded an average depth of 207 ± 20 µm (Figure C.4b). Although this is consistent with the expectation that angled insertions reduced insertion depth, this insertion depth is not sufficient for epidermal targeting. Moreover, the reduction in insertion depth was not as great as that predicted by the simple geometric calculation of 177 µm (outside the 95%

confidence interval of 184–217 μm). It is not clear why this calculated value was not predictive, but it probably has to do with the non-rigid nature of skin tissue that does not conform to the shape of a perfect right triangle.

Further decreasing the insertion angle to 20° lowered insertion depth to 97 ± 15 μm (Figure C.4c), which is in the range of human epidermal thickness (~100 μm), thus suggesting a viable way to increase the extent of epidermal targeting with MNs. In addition, this insertion depth is not significantly different from the calculated depth of 85 μm (within 95% confidence interval of 83–112 μm). Fluorescence images of all nine replicates for each of the three angles reported can be found in Figures D.2 – D.4.

We also considered the degree of variability of insertion depth and found that the coefficient of variation was ~10% after 90° and 45° insertion and was ~15% after 20° insertion (Figure C.4d). Sources of variability may be due to MNs sometimes "jumping" across the tissue or sometimes bending due to imperfect rigidity of the MNs, causing less uniform delivery. We noted that these effects were more prevalent during insertion at very acute angles, and this may explain the greater variability after 20° insertion. Other sources of variability include irregularities in the skin, pushing MNs too hard during insertion, performing perpendicular insertions by hand, and imperfect estimation of insertion depths from histological images. Nonetheless, variation was relatively small and suggests the ability to achieve targeted depth of insertion with good reliability.

C.4.4 Efficiency of Epidermal Targeting by Angled Microneedle Insertion

Although controlling MN insertion depth was this study's primary goal, the scope of this work also included assessing the degree of epidermal targeting. We did this by

staining the skin with H&E to identify the epidermis as a dark purple layer, while staining the dermis a pink/salmon color. In this way, the degree of epidermal localization was determined as the insertion site's interfacial contact length with the purple-stained regions divided by the total perimeter of the insertion site within the tissue (Figure D.5). While direct measurement of epidermal delivery would be ideal, this necessitates separating the stratum corneum, epidermis, and dermis layers through interventions, such as incubating skin with enzymes or heating skin to 50–60 °C. This could introduce artefacts, such as increased dye diffusion, likely inefficient dye/protein extraction efficiency, and mechanical disruption of the tissue. Consequently, we selected an imaging-based method that provides a reasonable estimate of the degree of epidermal targeting instead.

We found that decreasing the insertion angle significantly increased epidermal targeting (one-way ANOVA, $p < 0.001$; see Figure C.5 and Table D.1). Perpendicular insertion only afforded 25% ± 13% localization in the epidermis (Figure C.5a), whereas reducing the insertion angle to 45° improved this localization nearly twofold (42% ± 13%, Figure C.5b). Acute angle insertion at 20° further increased epidermal targeting to 70% ± 21% (Figure C.5c). H&E-stained images of all nine replicates for each of the three angles reported can be found in Figure D.6 – D.8.

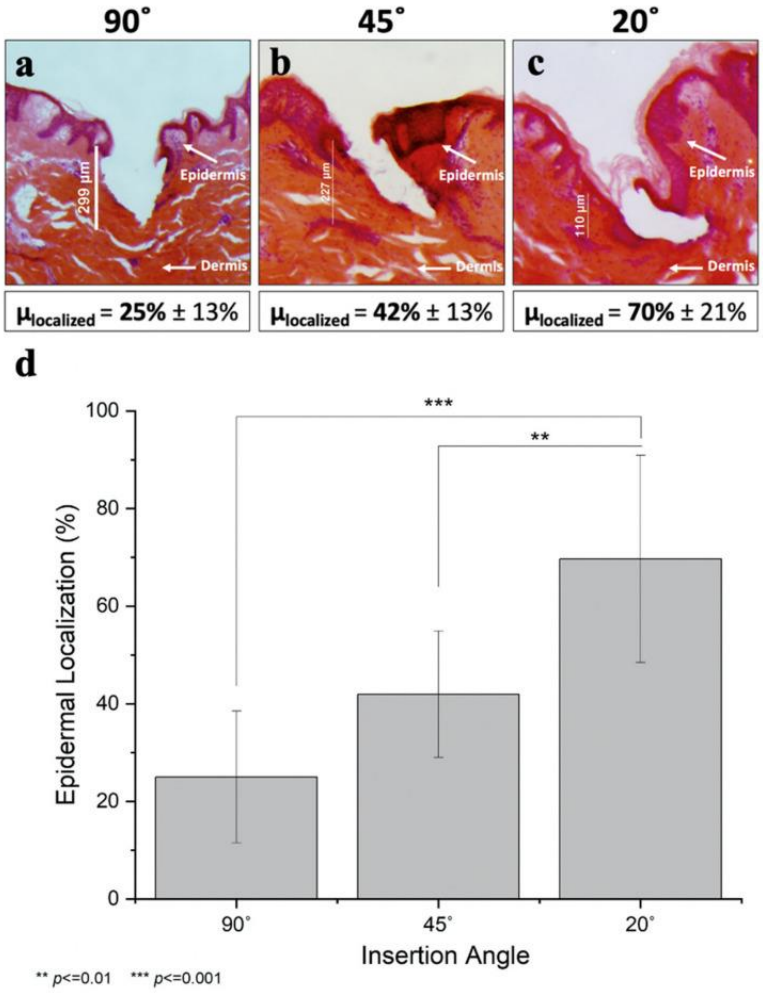

Figure C.5: Percent epidermal localization in skin after angled insertion. MNs measuring 250 µm in length were inserted at various angles into porcine skin ex vivo. Representative H&E-stained images of histological skin sections after insertion of MNs coated with peanut antigen at angles of (a) 90°, (b) 45°, and (c) 20°. Percent localization was determined by dividing the insertion site's interfacial contact length with the purple-stained epidermis regions by the total perimeter of the insertion site within the tissue. (d) Mean and standard deviation of percent localization after angled MN insertion for 9 replicates.

The coefficient of variation was highest for the perpendicularly inserted MNs; this can be explained by the natural morphology of the porcine epidermis, which is structurally similar to human epidermis [244, 245]. The epidermis has an undulating finger-like structure, with epidermal thickness varying as a function of position. When MNs were

inserted perpendicularly to the skin surface, they randomly localized either in one of the finger-like protrusions of the epidermis or in one of the “troughs” (Figure C.5a), causing significant variability in the interfacial contact distance at each insertion site. In contrast, MNs inserted at an angle almost always pierced through several of these finger-like protrusions, thereby decreasing the variability (Figure C.5b,c). Additionally, MNs were sometimes bent during insertion, and this served to increase epidermal localization because the direction in which the needles were bent resulted in shallower insertion depths (Figure C.5c). Because the force was always applied from above, the MNs were consistently bent in a predictable manner, tending to be parallel to the skin’s surface, thus leading to shallower depths of insertion.

C.4.5 OCT Imaging of Angled MN Insertion into Skin

To complement the analysis performed on histological skin sections stained after MN insertion, we also imaged the skin by OCT to visualize MNs embedded in situ in the skin (Figure C.6). In these images, the MNs can be seen as a bright line extending from the upper right corner. While the skin is present across the whole bottom half of the images, it can only be seen on the left side, because the right side is shadowed from view by the angled insertion device positioned between the skin and the OCT imaging head. In these images, the MN can be seen penetrating into the skin at an angle reaching depths of approximately 100 μm after 20° insertion and approximately 200 μm after 45° insertion, which is in general agreement with the data from histological sections.

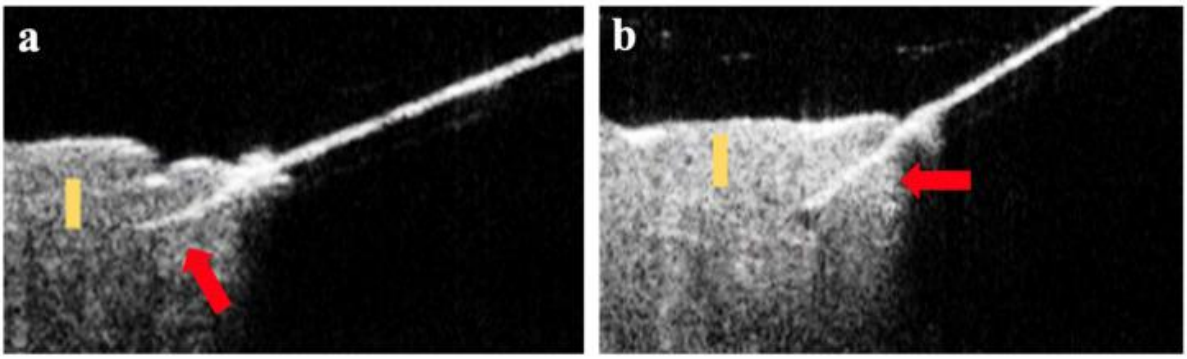

Figure C.6: Representative OCT images of MNs inserted into skin at an angle. The MNs appear as a bright line that extends from the top right into the skin (red arrow). The light region on the lower left is skin. The dark region on the lower right is skin that is shadowed by the MN and therefore cannot be seen. The skin is oriented with the stratum-corneum-side up. (a) MN inserted at 20°. Yellow scale bar (100 µm) shows a MN insertion depth of approximately 100 µm. (b) MN inserted at 45°. Yellow scale bar (100 µm) shows a MN insertion depth of close to 200 µm.

C.5 Discussion

This study introduced angled insertion of MNs into the skin to reduce insertion depth and thereby target drug delivery to the epidermis. We achieved a shallow insertion depth with increased epidermal targeting by using a short MN (250 µm long) inserted at an acute angle to the skin surface (20°) that enabled an insertion depth less than 100 µm and epidermal targeting of up to 70%.

Shallow insertion of MNs into skin has been studied before, but not via angled MN insertion. One approach involves very short MNs (*e.g.*, <100 µm long) and their application to skin at sufficiently high velocity that the skin does not deform during the MN insertion process, thereby enabling insertion of MNs that would otherwise be too short to penetrate skin [236]. A limitation of this approach is that coating such short MNs is difficult [246] and that insertion at high velocity requires a special applicator, which adds cost, size, and

complexity to the MN delivery system. Here, we distinguish between an applicator, which provides the force (*e.g.*, using a spring) to accomplish the insertion, and our device, which is a guide that assists a manual insertion. We expect that angled MN insertion can be manually accomplished with appropriate design of a simple-to-use MN patch and its housing without the need for a bulky, expensive applicator. Another approach, using hollow MNs, involves drilling MNs into the skin by rotational insertion [247]. This minimizes skin-surface deformation and allows MN insertion to precise depths for injection into skin. This approach was used for individual MNs, because each MN needs to rotate around its own central axis, making it difficult to employ using arrays of MNs.

Many skin treatments could benefit from epidermal targeting. For example, dermatological disorders, such as basal and squamous cell carcinomas, cutaneous warts, and vitiligo, have pathology in the epidermis [248] which means that epidermal delivery can increase drug efficacy. Furthermore, because the viable epidermis (possible mediated by the basal membrane at the dermal–epidermal junction) provides a significant barrier to diffusion of macromolecules, protein delivered to epidermis may be retained there [249]. Of particular interest to this study is allergy immunotherapy, for which targeted epidermal delivery is expected to facilitate generating immune tolerance while reducing the risk of adverse side effects from systemic antigen exposure [250]. Additionally, MN-based allergy immunotherapy may reduce the need for SCIT, democratizing allergy treatment in several ways. First, immunotherapy by MN patch may substantially lower the treatment cost, as more than $4000 per year is spent on injecting medication into children suffering from food allergies [251]. Mitigating the issue of needle phobia may also increase patient compliance and expand the patient base for non-oral food-allergy immunotherapy. If MN patches for

immunotherapy can be administered at home, parents may eliminate many trips to the doctor by administering patches themselves.

While this study demonstrates the feasibility of epidermal targeting by using angled MNs, additional studies are needed to fully validate the approach and assess its utility. For example, this study was limited to MN application to porcine skin ex vivo. Future studies need to assess delivery in vivo and in human skin. In addition, epidermal localization was shown mostly by histological analysis of MN tracks in the skin and deposition of coated material from the MNs. The ability of antigen or other materials delivered in this way to not only be delivered to epidermis, but remain there, even in the presence of an active vasculature, notably in the superficial dermis, needs to be studied. Drug size and other characteristics will affect local drug distribution in the skin based on rates of diffusion, tissue binding and other factors. While MNs, especially ones as short as 250 μm, have been shown to be painless and well tolerated [252, 253] the safety and acceptability of angled MN insertion need to be studied. Finally, while the angled insertion device used in this study was effective, use outside the research setting would benefit from a smaller device with a fixed angle, requiring no expertise or training to use.

C.6 Conclusions

This work demonstrated that angled MN insertion can be used to target antigen delivery to the upper layers of the skin, notably the epidermis. We first developed an MN coating method to achieve a target dose of 0.5 μg peanut protein antigen (*Arachis hypogaea*) per MN by adjusting coating formulation composition, MN length, and number of dip-coating cycles. Using a custom 3D-printed biplanar angular insertion device, we

inserted MNs into porcine skin ex vivo with controlled insertion angles of 20°, 45°, and 90°. Histological analysis determined that angled insertion at 20° reduced mean depth of MN penetration into skin from 265 to 97 μm compared to perpendicular (90°) insertion; this result was consistent with additional imaging performed by OCT. The extent of epidermal targeting increased from 25% after perpendicular delivery to 70% after delivery at a 20° angle. We conclude that angled MN insertion provides a promising approach to targeting drug delivery to the epidermis that may improve allergy immunotherapy and enable other applications with epidermal delivery targets.

APPENDIX D. SUPPLEMENTARY MATERIALS FOR APPENDIX C

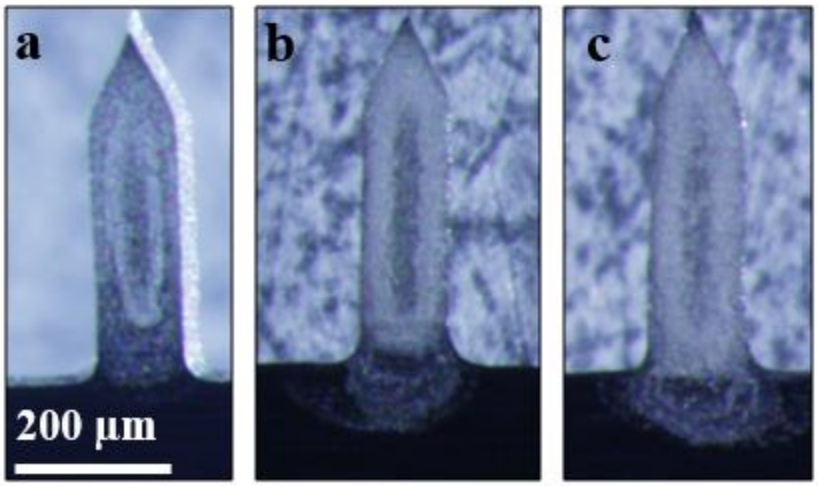

Figure D.1: Representative images of MNs with coatings past the base of MNs. MNs measuring were coated using a formulation containing 1% (*w/v*) CMC, 0.5% (*w/v*) Pluronic F-68, 2% (*w/v*), and peanut antigen using (a) 5, (b) 10 or (c) 15 dip-coating cycles.

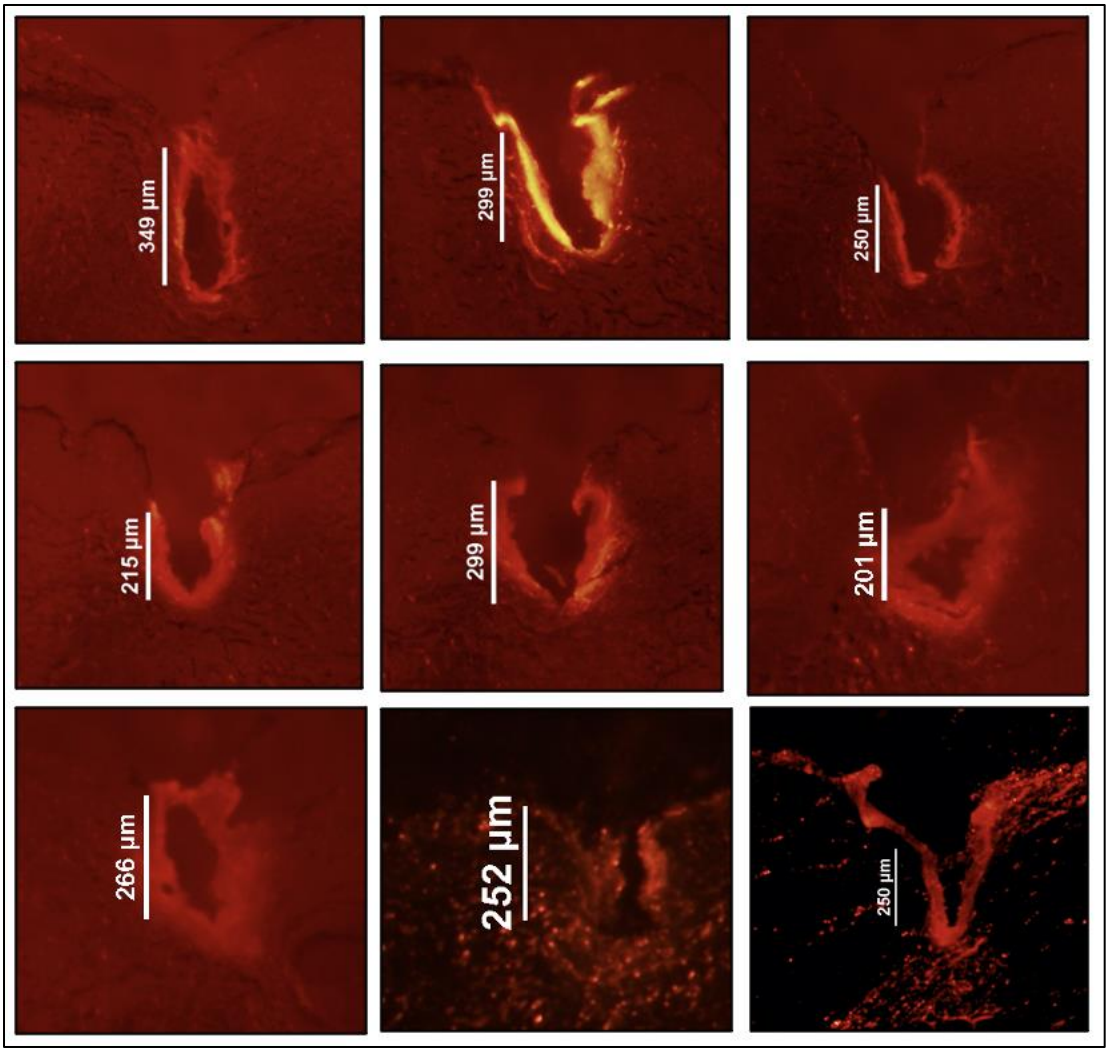

Figure D.2: Images of histological skin sections after insertion of MNs coated with red-fluorescent sulforhodamine dye at an angle of 90° used to generated data presented in Figure C.4.

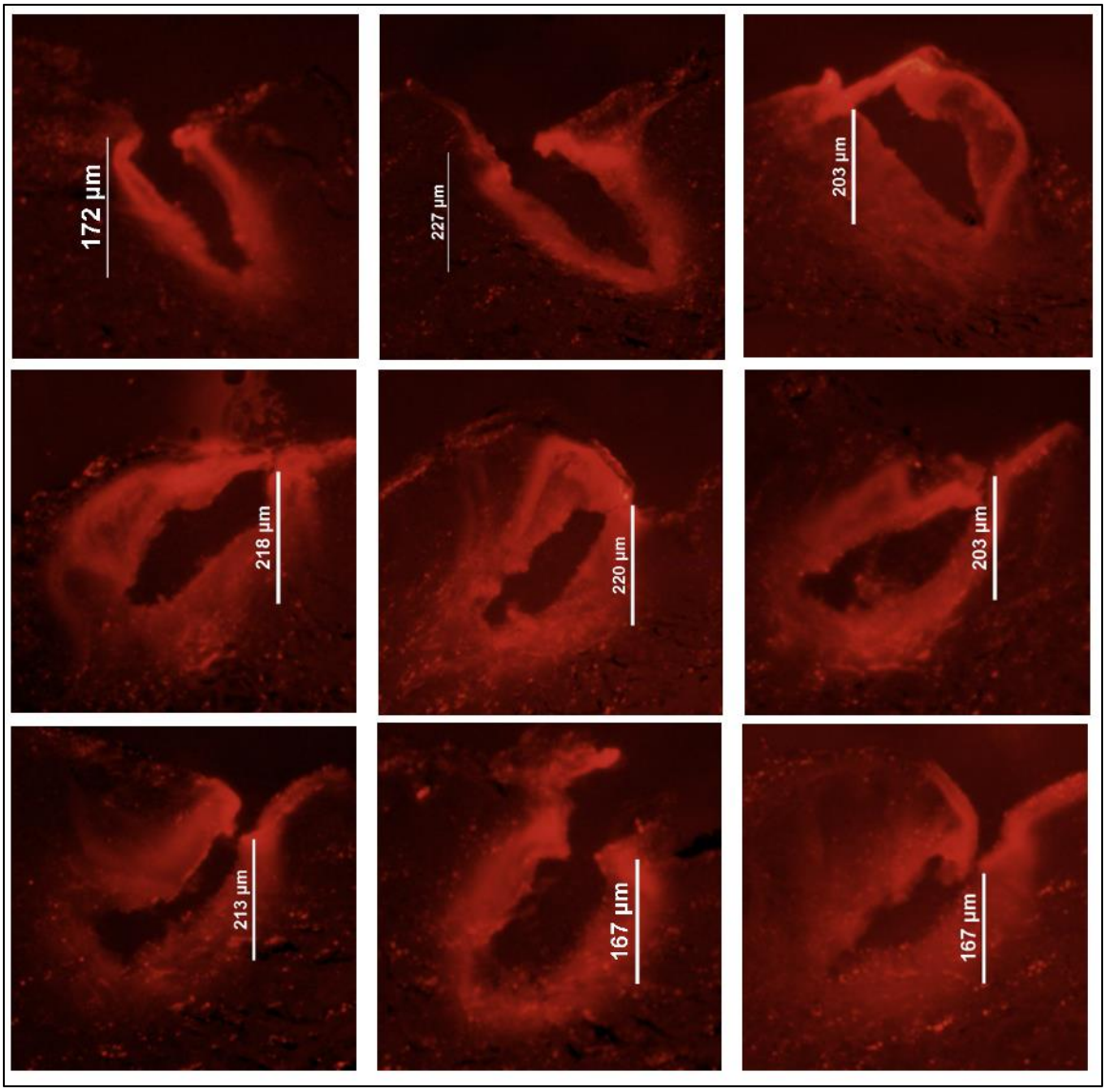

Figure D.3: Images of histological skin sections after insertion of MNs coated with red-fluorescent sulforhodamine dye at an angle of 45° used to generated data presented in Figure C.4.

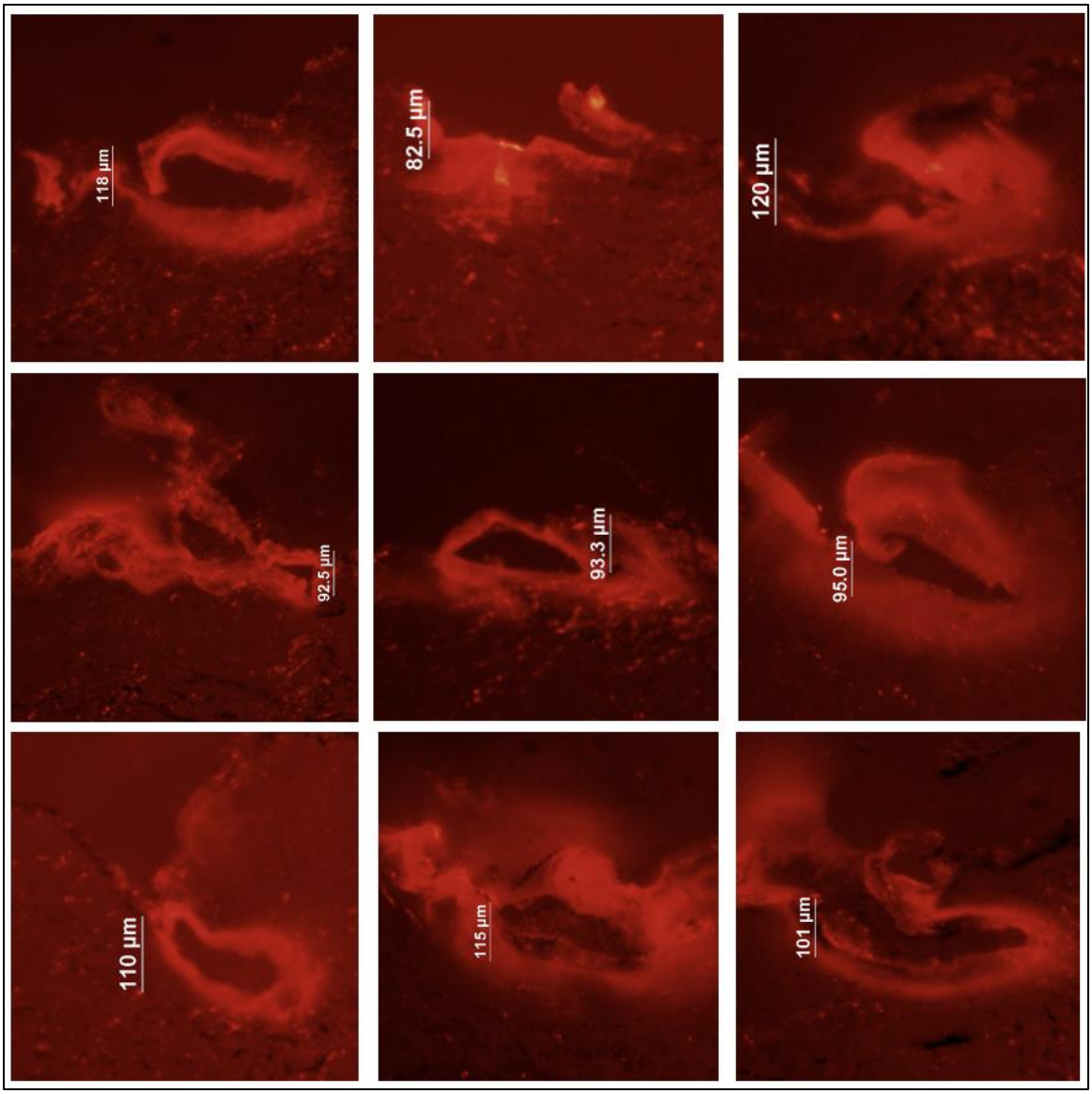

Figure D.4: Images of histological skin sections after insertion of MNs coated with red-fluorescent sulforhodamine dye at an angle of 20° used to generated data presented in Figure C.4.

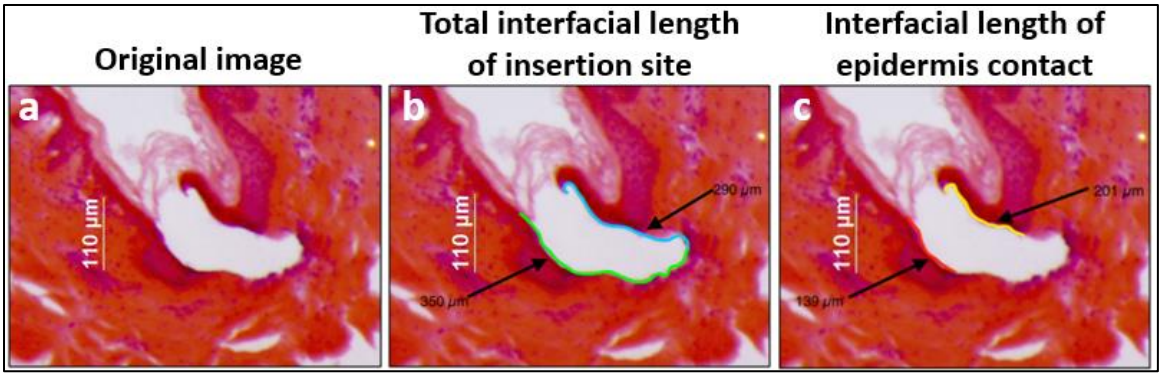

Figure D.5: Representative H&E-stained images of 250 µm-long MNs inserted at 20° illustrating the method to calculate epidermis percent localization: (a) original insertion site image; (b) total interfacial length of the insertion site (640 µm); (c) interfacial epidermis contact length of the insertion site (340 µm).

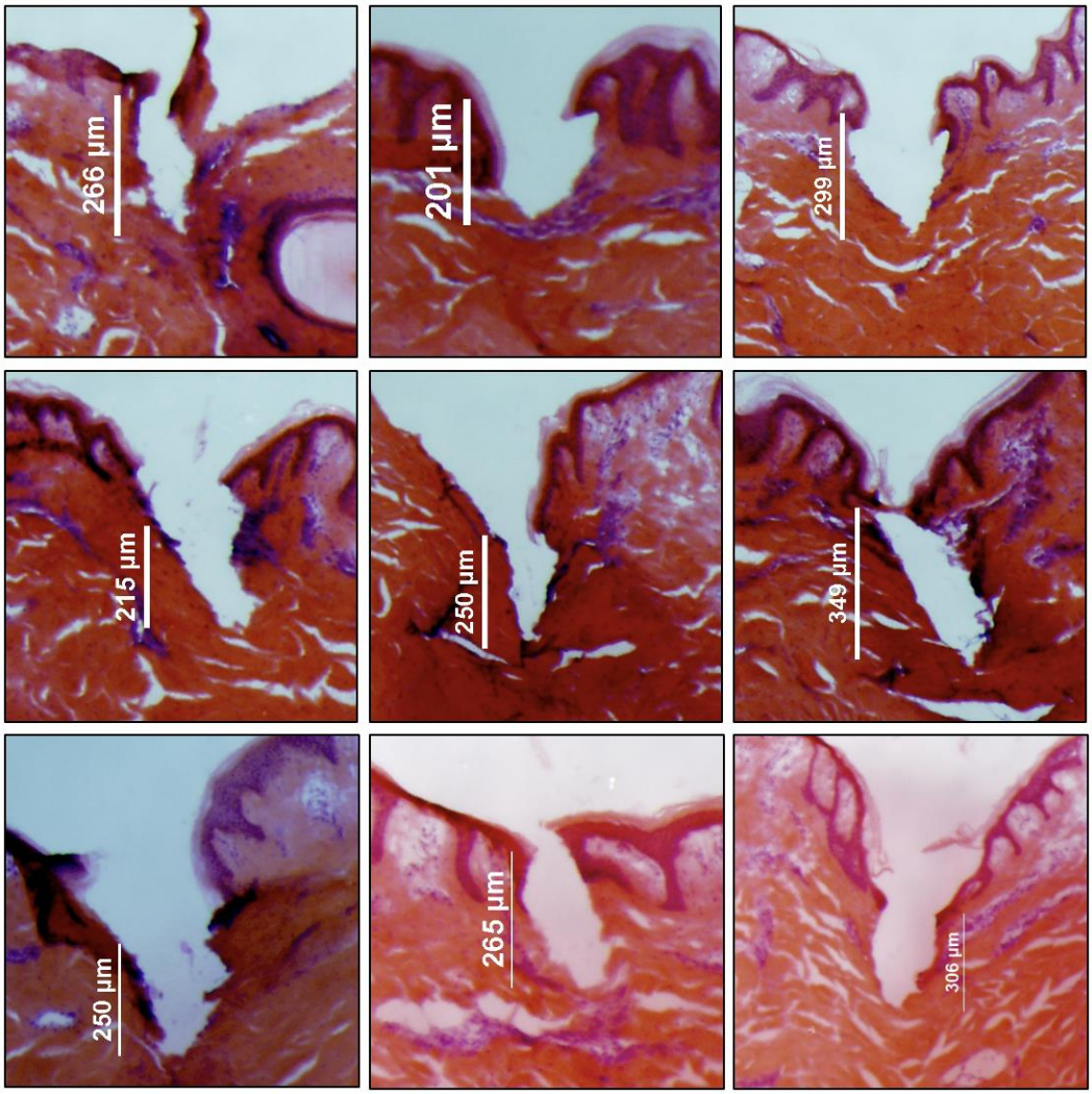

Figure D.6: Images of histological skin sections stained with H&E after insertion of MNs at an angle of 90˚ used to generated data presented in Figure C.5.

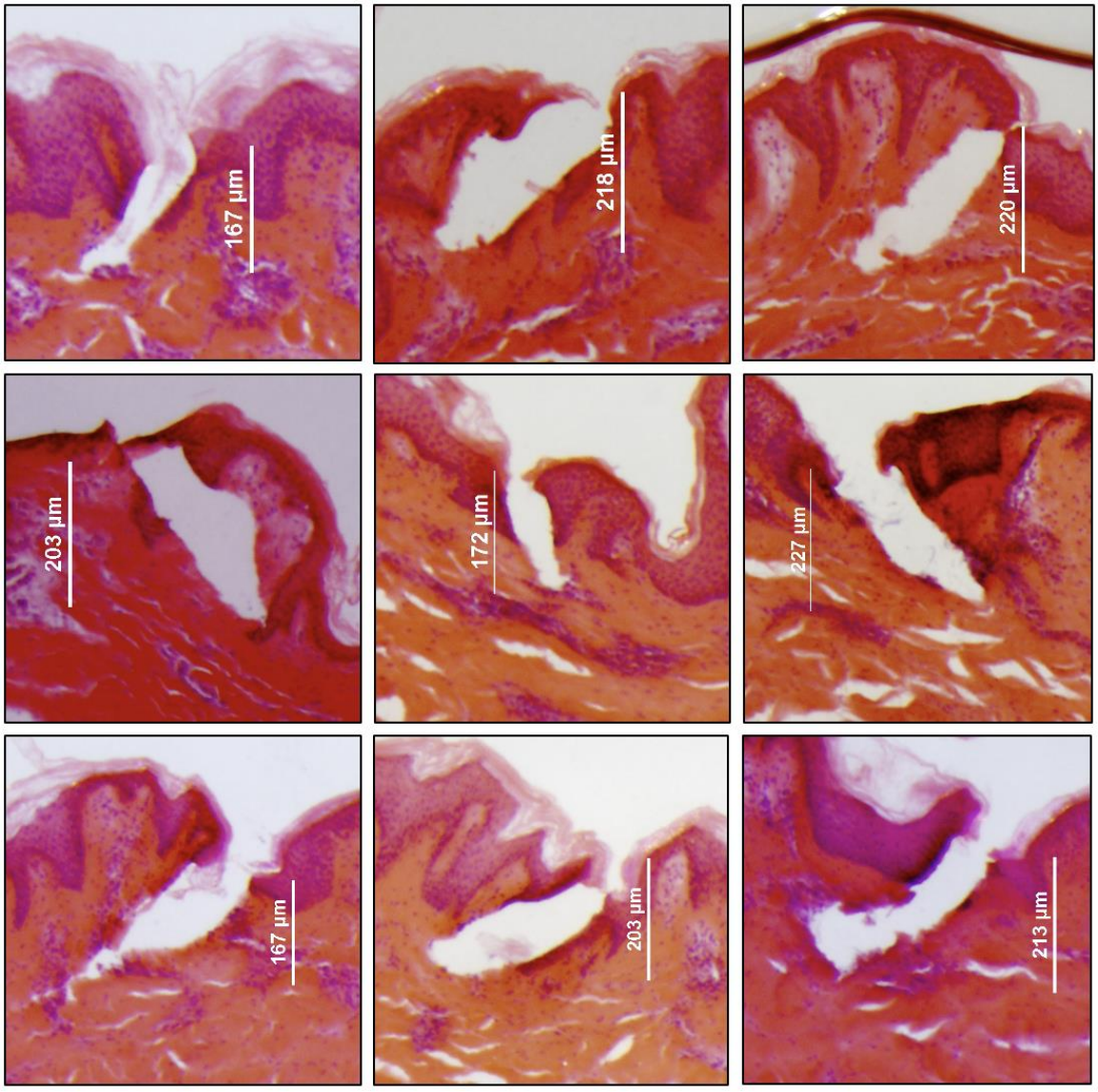

Figure D.7: Images of histological skin sections stained with H&E after insertion of MNs at an angle of 45˚ used to generated data presented in Figure C.5.

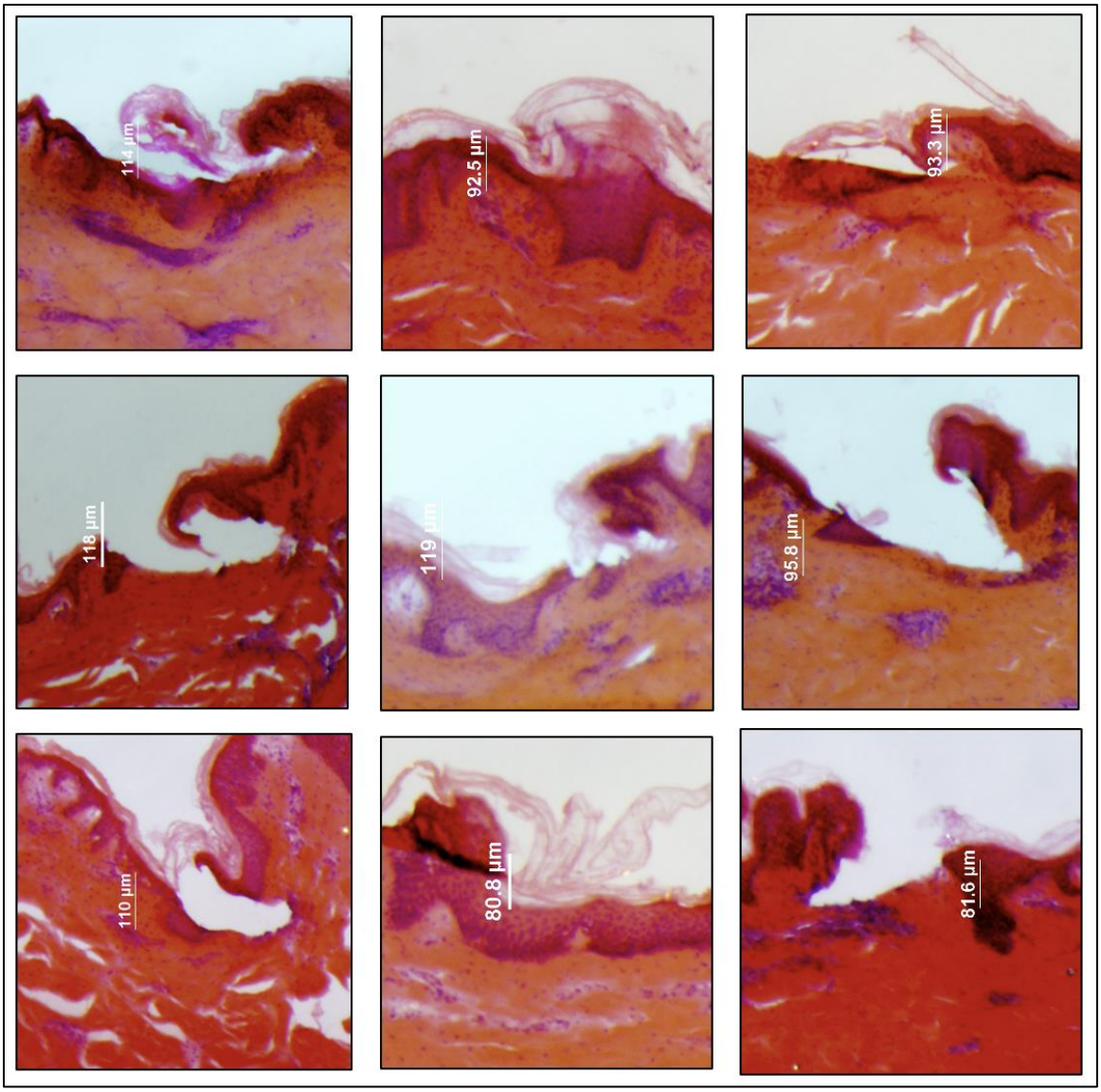

Figure D.8: Images of histological skin sections stained with H&E after insertion of MNs at an angle of 20˚ used to generated data presented in Figure C.5.

Table D.1: Percent epidermal localization and associated statistics for each of the three insertion angles studied.

Percent Epidermal Localization				
		Angle of Insertion		
		90˚	**45˚**	**20˚**
Replicate	1	16.8%	52.6%	100.0%
	2	39.1%	46.9%	100.0%
	3	25.0%	18.9%	72.0%
	4	40.9%	34.9%	47.5%
	5	11.9%	26.5%	83.4%
	6	8.7%	44.0%	61.0%
	7	18.7%	61.4%	52.9%
	8	45.5%	44.0%	67.3%
	9	18.4%	53.8%	43.0%
Statistics	**Mean**	**25.0%**	**42.6%**	**69.7%**
	StDev	**13.5%**	**13.6%**	**21.2%**

REFERENCES

1. Smith, K.A., *Edward jenner and the small pox vaccine.* Front Immunol, 2011. **2**: p. 21.

2. Han, S., *Clinical vaccine development.* Clin Exp Vaccine Res, 2015. **4**(1): p. 46-53.

3. Douglas, R.G., Samant, V.B., *The Vaccine Industry.* Plotkin's Vaccines, 2018.

4. Kandola, K. and Y. Bergevin, *Immunization and child health in developing countries: Canada's response.* Paediatr Child Health, 2000. **5**(7): p. 378-80.

5. Pambudi, N.A., et al., *Vaccine cold chain management and cold storage technology to address the challenges of vaccination programs.* Energy Reports, 2022. **8**: p. 955-972.

6. WHO, *Monitoring vaccine wastage at a country level*. 2005, World Health Organization.

7. Pollard, A.J. and E.M. Bijker, *A guide to vaccinology: from basic principles to new developments.* Nat Rev Immunol, 2021. **21**(2): p. 83-100.

8. Iwasaki, A. and S.B. Omer, *Why and How Vaccines Work.* Cell, 2020. **183**(2): p. 290-295.

9. A. Patricia Wodi, V.M. *Immunology and Vaccine-Preventable Diseases*. Principles of Vaccination 2021.

10. Minor, P.D., *Live attenuated vaccines: Historical successes and current challenges.* Virology, 2015. **479-480**: p. 379-392.

11. Nzolo, D., et al., *Adverse events following immunization with oral poliovirus in Kinshasa, Democratic Republic of Congo: preliminary results.* Pathog Glob Health, 2013. **107**(7): p. 381-4.

12. Burke, C.J., T.A. Hsu, and D.B. Volkin, *Formulation, stability, and delivery of live attenuated vaccines for human use.* Crit Rev Ther Drug Carrier Syst, 1999. **16**(1): p. 1-83.

13. Barbara Sanders, M.K., Hanneke Schuitemaker, *Inactivated Viral Vaccines*, in *Vaccine Analysis: Strategies, Principles, and Control*, V.E.T. Brian K. Nunnally, Robert D. Sitrin, Editor. 2014, Springer Berlin Heidelberg.

14. Murdin, A.D., L. Barreto, and S. Plotkin, *Inactivated poliovirus vaccine: past and present experience.* Vaccine, 1996. **14**(8): p. 735-46.

15. Clem, A.S., *Fundamentals of vaccine immunology.* J Glob Infect Dis, 2011. **3**(1): p. 73-8.

16. Hu, C.M. and L. Zhang, *Nanotoxoid Vaccines.* Nano Today, 2014. **9**(4): p. 401-404.

17. Moyle, P.M. and I. Toth, *Modern subunit vaccines: development, components, and research opportunities.* ChemMedChem, 2013. **8**(3): p. 360-76.

18. Vartak, A. and S.J. Sucheck, *Recent Advances in Subunit Vaccine Carriers.* Vaccines (Basel), 2016. **4**(2).

19. Adkins, J.C. and A.J. Wagstaff, *Recombinant hepatitis B vaccine: a review of its immunogenicity and protective efficacy against hepatitis B.* BioDrugs, 1998. **10**(2): p. 137-58.

20. Donaldson, B., et al., *Virus-like particle vaccines: immunology and formulation for clinical translation.* Expert Rev Vaccines, 2018. **17**(9): p. 833-849.

21. Kushnir, N., S.J. Streatfield, and V. Yusibov, *Virus-like particles as a highly efficient vaccine platform: diversity of targets and production systems and advances in clinical development.* Vaccine, 2012. **31**(1): p. 58-83.

22. Nooraei, S., et al., *Virus-like particles: preparation, immunogenicity and their roles as nanovaccines and drug nanocarriers.* J Nanobiotechnology, 2021. **19**(1): p. 59.

23. Chaudhary, N., D. Weissman, and K.A. Whitehead, *mRNA vaccines for infectious diseases: principles, delivery and clinical translation.* Nature Reviews Drug Discovery, 2021. **20**(11): p. 817-838.

24. Zhang, C., et al., *Advances in mRNA Vaccines for Infectious Diseases.* Front Immunol, 2019. **10**: p. 594.

25. Mascellino, M.T., et al., *Overview of the Main Anti-SARS-CoV-2 Vaccines: Mechanism of Action, Efficacy and Safety.* Infect Drug Resist, 2021. **14**: p. 3459-3476.

26. Hassel, B., *Tetanus: pathophysiology, treatment, and the possibility of using botulinum toxin against tetanus-induced rigidity and spasms.* Toxins (Basel), 2013. **5**(1): p. 73-83.

27. Blencowe, H., et al., *Tetanus toxoid immunization to reduce mortality from neonatal tetanus.* Int J Epidemiol, 2010. **39 Suppl 1**(Suppl 1): p. i102-9.

28. Rabadi, T. and M.F. Brady, *Tetanus Toxoid*, in *StatPearls*. 2022, StatPearls Publishing Copyright © 2022, StatPearls Publishing LLC.: Treasure Island (FL).
29. *Diphtheria, Tetanus, and Pertussis Vaccine Recommendations*. Vaccines and Preventable Diseases 2022.

30. Fetuga, B.M., T.A. Ogunlesi, and F.A. Adekanmbi, *Risk factors for mortality in neonatal tetanus: a 15-year experience in Sagamu, Nigeria.* World J Pediatr, 2010. **6**(1): p. 71-5.

31. O'Hare, B., et al., *Income and child mortality in developing countries: a systematic review and meta-analysis.* J R Soc Med, 2013. **106**(10): p. 408-14.

32. WHO. *Immunization coverage*. 2022 [cited 2022.

33. Muhoza P, D.-H.M., Diallo MS, et al., *Routine Vaccination Coverage — Worldwide, 2020.* MMWR Morb Mortal Wkly Rep, 2021. **70**: p. 1495-1500.

34. Bangura, J.B., et al., *Barriers to childhood immunization in sub-Saharan Africa: A systematic review.* BMC Public Health, 2020. **20**(1): p. 1108.

35. Cockcroft, A., et al., *Why children are not vaccinated against measles: a cross-sectional study in two Nigerian States.* Archives of Public Health, 2014. **72**(1): p. 48.

36. Bogale, H.A., A.F. Amhare, and A.A. Bogale, *Assessment of factors affecting vaccine cold chain management practice in public health institutions in east Gojam zone of Amhara region.* BMC Public Health, 2019. **19**(1): p. 1433.

37. Dairo, D.M. and O.E. Osizimete, *Factors affecting vaccine handling and storage practices among immunization service providers in Ibadan, Oyo State, Nigeria.* Afr Health Sci, 2016. **16**(2): p. 576-83.

38. *Cold Chain Logistics Market to Reach Valuation of USD 464.0 Million by 2028*. 2022.

39. Dumpa, N., et al., *Stability of Vaccines.* AAPS PharmSciTech, 2019. **20**(2): p. 42.

40. Preston, K.B. and T.W. Randolph, *Stability of lyophilized and spray dried vaccine formulations.* Advanced Drug Delivery Reviews, 2021. **171**: p. 50-61.

41. Hansen, L.J.J., et al., *Freeze-drying of live virus vaccines: A review.* Vaccine, 2015. **33**(42): p. 5507-5519.

42. Vogel, F.R. and M.F. Powell, *A compendium of vaccine adjuvants and excipients.* Pharm Biotechnol, 1995. **6**: p. 141-228.

43. Ionova, Y. and L. Wilson, *Biologic excipients: Importance of clinical awareness of inactive ingredients.* PLoS One, 2020. **15**(6): p. e0235076.

44. Vandecruys, R., et al., *Use of a screening method to determine excipients which optimize the extent and stability of supersaturated drug solutions and application of this system to solid formulation design.* Int J Pharm, 2007. **342**(1-2): p. 168-75.

45. Caballero, M.L., et al., *Hidden Dangers: Recognizing Excipients as Potential Causes of Drug and Vaccine Hypersensitivity Reactions.* J Allergy Clin Immunol Pract, 2021. **9**(8): p. 2968-2982.

46. Chu, L.Y., et al., *Enhanced Stability of Inactivated Influenza Vaccine Encapsulated in Dissolving Microneedle Patches.* Pharm Res, 2016. **33**(4): p. 868-78.

47. Mistilis, M.J., et al., *Long-term stability of influenza vaccine in a dissolving microneedle patch.* Drug Delivery and Translational Research, 2017. **7**(2): p. 195-205.

48. Joyce, J.C., et al., *Thermostability of Measles and Rubella Vaccines in a Microneedle Patch.* Adv Ther (Weinh), 2021. **4**(10).

49. Nguyen, T.T., et al., *Progress in microneedle array patch (MAP) for vaccine delivery.* Human Vaccines & Immunotherapeutics, 2021. **17**(1): p. 316-327.

50. Lee, J., et al., *Metal–organic framework materials as catalysts.* Chemical Society Reviews, 2009. **38**(5): p. 1450-1459.

51. Kang, Z., L. Fan, and D. Sun, *Recent advances and challenges of metal–organic framework membranes for gas separation.* Journal of Materials Chemistry A, 2017. **5**(21): p. 10073-10091.

52. Rojas, S., A. Arenas-Vivo, and P. Horcajada, *Metal-organic frameworks: A novel platform for combined advanced therapies.* Coordination Chemistry Reviews, 2019. **388**: p. 202-226.

53. Furukawa, H., et al., *The Chemistry and Applications of Metal-Organic Frameworks.* Science, 2013. **341**(6149): p. 974-+.

54. Burtch, N.C., H. Jasuja, and K.S. Walton, *Water Stability and Adsorption in Metal-Organic Frameworks.* Chemical Reviews, 2014. **114**(20): p. 10575-10612.

55. Farha, O.K. and J.T. Hupp, *Rational Design, Synthesis, Purification, and Activation of Metal−Organic Framework Materials.* Accounts of Chemical Research, 2010. **43**(8): p. 1166-1175.

56. Baa, E., et al., *Current Trend in Synthesis, Post-Synthetic Modifications and Biological Applications of Nanometal-Organic Frameworks (NMOFs).* Chinese Journal of Chemistry, 2019. **37**(4): p. 378-404.

57. Wang, Z. and S.M. Cohen, *Postsynthetic Covalent Modification of a Neutral Metal−Organic Framework.* Journal of the American Chemical Society, 2007. **129**(41): p. 12368-12369.

58. Cai, W., et al., *Engineering Phototheranostic Nanoscale Metal–Organic Frameworks for Multimodal Imaging-Guided Cancer Therapy.* ACS Applied Materials & Interfaces, 2017. **9**(3): p. 2040-2051.

59. McKinlay, A.C., et al., *BioMOFs: Metal–Organic Frameworks for Biological and Medical Applications.* Angewandte Chemie International Edition, 2010. **49**(36): p. 6260-6266.

60. Horcajada, P., et al., *Metal–Organic Frameworks as Efficient Materials for Drug Delivery.* Angewandte Chemie International Edition, 2006. **45**(36): p. 5974-5978.

61. Horcajada, P., et al., *Porous metal–organic-framework nanoscale carriers as a potential platform for drug delivery and imaging.* Nature Materials, 2010. **9**(2): p. 172-178.

62. Horcajada, P., et al., *Flexible Porous Metal-Organic Frameworks for a Controlled Drug Delivery.* Journal of the American Chemical Society, 2008. **130**(21): p. 6774-6780.

63. Chowdhury, M.A., *The applications of metal-organic-frameworks in controlled release of drugs.* Review Journal of Chemistry, 2017. **7**(1): p. 1-22.

64. Luzuriaga, M.A., et al., *Enhanced Stability and Controlled Delivery of MOF-Encapsulated Vaccines and Their Immunogenic Response In Vivo.* ACS Applied Materials & Interfaces, 2019. **11**(10): p. 9740-9746.

65. Lyu, F., et al., *One-Pot Synthesis of Protein-Embedded Metal–Organic Frameworks with Enhanced Biological Activities.* Nano Letters, 2014. **14**(10): p. 5761-5765.

66. Liang, K., et al., *Biomimetic mineralization of metal-organic frameworks as protective coatings for biomacromolecules.* Nature Communications, 2015. **6**.

67. Talley, K. and E. Alexov, *On the pH-optimum of activity and stability of proteins.* Proteins, 2010. **78**(12): p. 2699-706.

68. Ricco, R., et al., *Metal-Organic Frameworks for Cell and Virus Biology: A Perspective.* Acs Nano, 2018. **12**(1): p. 13-23.

69. Liang, W., et al., *Control of Structure Topology and Spatial Distribution of Biomacromolecules in Protein@ZIF-8 Biocomposites.* Chemistry of Materials, 2018. **30**(3): p. 1069-1077.

70. Liang, K., et al., *Enzyme encapsulation in zeolitic imidazolate frameworks: a comparison between controlled co-precipitation and biomimetic mineralisation.* Chemical Communications, 2016. **52**(3): p. 473-476.

71. Liang, K., et al., *Metal–Organic Framework Coatings as Cytoprotective Exoskeletons for Living Cells.* Advanced Materials, 2016. **28**(36): p. 7910-7914.

72. Chen, Y., et al., *Size-Selective Biocatalysis of Myoglobin Immobilized into a Mesoporous Metal–Organic Framework with Hierarchical Pore Sizes.* Inorganic Chemistry, 2012. **51**(17): p. 9156-9158.

73. An-Wu Xu, Y.M., Helmut Cölfen, *Biomimetic mineralization.* Journal of Materials Chemistry, 2007. **17**: p. 415-449.

74. Park, K.S., et al., *Exceptional chemical and thermal stability of zeolitic imidazolate frameworks.* Proc Natl Acad Sci U S A, 2006. **103**(27): p. 10186-10191.

75. Zhang, H.F., M. Zhao, and Y.S. Lin, *Stability of ZIF-8 in water under ambient conditions.* Microporous and Mesoporous Materials, 2019. **279**: p. 201-210.

76. Wang, W., *Lyophilization and development of solid protein pharmaceuticals.* Int J Pharm, 2000. **203**(1-2): p. 1-60.

77. Hartmann, M. and X. Kostrov, *Immobilization of enzymes on porous silicas – benefits and challenges.* Chemical Society Reviews, 2013. **42**(15): p. 6277-6289.

78. Kida, K., et al., *Formation of high crystalline ZIF-8 in an aqueous solution.* CrystEngComm, 2013. **15**(9): p. 1794-1801.

79. Cychosz, K.A. and A.J. Matzger, *Water Stability of Microporous Coordination Polymers and the Adsorption of Pharmaceuticals from Water*. Langmuir, 2010. **26**(22): p. 17198-17202.

80. Pan, Y., et al., *Rapid synthesis of zeolitic imidazolate framework-8 (ZIF-8) nanocrystals in an aqueous system.* Chemical Communications, 2011. **47**(7): p. 2071-2073.

81. Zhang, H., et al., *Hydrolysis and condensation of ZIF-8 in water*. Microporous and Mesoporous Materials, 2019. **288**: p. 109568.

82. Wang, C., et al., *Metal–Organic Framework Encapsulation for Biospecimen Preservation.* Chemistry of Materials, 2018. **30**(4): p. 1291-1300.

83. Zheng, H., et al., *One-pot Synthesis of Metal–Organic Frameworks with Encapsulated Target Molecules and Their Applications for Controlled Drug Delivery.* Journal of the American Chemical Society, 2016. **138**(3): p. 962-968.

84. Wu, Q., et al., *Biocompatible and biodegradable zeolitic imidazolate framework/polydopamine nanocarriers for dual stimulus triggered tumor thermo-chemotherapy.* Biomaterials, 2018. **162**: p. 132-143.

85. Wu, M.X. and Y.W. Yang, *Metal-Organic Framework (MOF)-Based Drug/Cargo Delivery and Cancer Therapy.* Adv Mater, 2017. **29**(23).

86. Ruyra, À., et al., *Synthesis, Culture Medium Stability, and In Vitro and In Vivo Zebrafish Embryo Toxicity of Metal–Organic Framework Nanoparticles.* Chemistry – A European Journal, 2015. **21**(6): p. 2508-2518.

87. Skou, S., R.E. Gillilan, and N. Ando, *Synchrotron-based small-angle X-ray scattering of proteins in solution.* Nature protocols, 2014. **9**(7): p. 1727-1739.

88. Boldon, L., F. Laliberte, and L. Liu, *Review of the fundamental theories behind small angle X-ray scattering, molecular dynamics simulations, and relevant integrated application.* Nano Rev, 2015. **6**: p. 25661.

89. Brosey, C.A. and J.A. Tainer, *Evolving SAXS versatility: solution X-ray scattering for macromolecular architecture, functional landscapes, and integrative structural biology.* Curr Opin Struct Biol, 2019. **58**: p. 197-213.

90. Rambo, R.P. and J.A. Tainer, *Characterizing flexible and intrinsically unstructured biological macromolecules by SAS using the Porod-Debye law.* Biopolymers, 2011. **95**(8): p. 559-71.

91. Smilgies, D.M. and E. Folta-Stogniew, *Molecular weight-gyration radius relation of globular proteins: a comparison of light scattering, small-angle X-ray scattering and structure-based data.* J Appl Crystallogr, 2015. **48**(Pt 5): p. 1604-1606.

92. Zheng, W. and R.B. Best, *An Extended Guinier Analysis for Intrinsically Disordered Proteins.* J Mol Biol, 2018. **430**(16): p. 2540-2553.

93. Thomas, W., *SAXS Fundamentals*. 2021, Cornell high energy synchrotron source.

94. Hopkins, J.B., R.E. Gillilan, and S. Skou, *BioXTAS RAW: improvements to a free open-source program for small-angle X-ray scattering data reduction and analysis.* J Appl Crystallogr, 2017. **50**(Pt 5): p. 1545-1553.

95. May Nyman, L.M., *Small Angle X-ray Scattering of Group V Polyoxometalates*, in *Trends in Polyoxometalates Research*, D.S. L. Ruhlmann, Editor. 2015, Nova Science Publishers Inc. p. 151-170.

96. Putnam, C.D., et al., *X-ray solution scattering (SAXS) combined with crystallography and computation: defining accurate macromolecular structures, conformations and assemblies in solution.* Q Rev Biophys, 2007. **40**(3): p. 191-285.

97. Konegger, T., C. Drechsel, and H. Peterlik, *In-situ small angle X-ray scattering (SAXS) – A versatile tool for clarifying the evolution of microporosity in polymer-derived ceramics.* Microporous and Mesoporous Materials, 2021. **324**: p. 111268.

98. Yadav, R., et al., *Temperature Assisted in-Situ Small Angle X-ray Scattering Analysis of Ph-POSS/PC Polymer Nanocomposite.* Scientific Reports, 2016. **6**(1): p. 29917.

99. Tsao, C.-S., et al., *Characterization of Pore Structure in Metal−Organic Framework by Small-Angle X-ray Scattering.* Journal of the American Chemical Society, 2007. **129**(51): p. 15997-16004.

100. Goesten, M.G., et al., *Small-angle X-ray scattering documents the growth of metal-organic frameworks.* Catalysis Today, 2013. **205**: p. 120-127.

101. Singh, R., et al., *Stable MOF@enzyme composites for electrochemical biosensing devices.* Journal of Materials Chemistry C, 2021. **9**(24): p. 7677-7688.

102. Bunaciu, A.A., E.G. Udriştioiu, and H.Y. Aboul-Enein, *X-ray diffraction: instrumentation and applications.* Crit Rev Anal Chem, 2015. **45**(4): p. 289-99.

103. Holder, C.F. and R.E. Schaak, *Tutorial on Powder X-ray Diffraction for Characterizing Nanoscale Materials.* ACS Nano, 2019. **13**(7): p. 7359-7365.

104. Langford, J.I. and A.J.C. Wilson, *Scherrer after sixty years: A survey and some new results in the determination of crystallite size.* Journal of Applied Crystallography, 1978. **11**(2): p. 102-113.

105. Berthomieu, C. and R. Hienerwadel, *Fourier transform infrared (FTIR) spectroscopy.* Photosynthesis Research, 2009. **101**(2): p. 157-170.

106. Tiernan, H., B. Byrne, and S.G. Kazarian, *ATR-FTIR spectroscopy and spectroscopic imaging for the analysis of biopharmaceuticals.* Spectrochim Acta A Mol Biomol Spectrosc, 2020. **241**: p. 118636.

107. Jones, C.G., *Sanning Electron Microscopy: Preparation and Imaging for SEM*, in *Forensic Microscopy for Skeletal Tissues*, J.M. Walker, Editor. 2012, Humana Press.

108. Nguyen, J.N.T. and A.M. Harbison, *Scanning Electron Microscopy Sample Preparation and Imaging.* Methods Mol Biol, 2017. **1606**: p. 71-84.

109. Golding, C.G., et al., *The scanning electron microscope in microbiology and diagnosis of infectious disease.* Sci Rep, 2016. **6**: p. 26516.

110. Elliott, A.D., *Confocal Microscopy: Principles and Modern Practices.* Curr Protoc Cytom, 2020. **92**(1): p. e68.

111. Reynaud, K., et al., *Confocal microscopy: principles and applications to the field of reproductive biology.* Folia Histochem Cytobiol, 2001. **39**(2): p. 75-85.

112. Collazo, A., O. Bricaud, and K. Desai, *Use of confocal microscopy in comparative studies of vertebrate morphology.* Methods Enzymol, 2005. **395**: p. 521-43.

113. Gao, K., R. Oerlemans, and M.R. Groves, *Theory and applications of differential scanning fluorimetry in early-stage drug discovery*. Biophysical Reviews, 2020. **12**(1): p. 85-104.

114. Alexander, C.G., et al., *Novel microscale approaches for easy, rapid determination of protein stability in academic and commercial settings.* Biochimica et Biophysica Acta (BBA) - Proteins and Proteomics, 2014. **1844**(12): p. 2241-2250.

115. Sakamoto, S., et al., *Enzyme-linked immunosorbent assay for the quantitative/qualitative analysis of plant secondary metabolites.* J Nat Med, 2018. **72**(1): p. 32-42.

116. Aydin, S., *A short history, principles, and types of ELISA, and our laboratory experience with peptide/protein analyses using ELISA.* Peptides, 2015. **72**: p. 4-15.

117. Andre, F.E., et al., *Vaccination greatly reduces disease, disability, death and inequity worldwide.* Bull World Health Organ, 2008. **86**(2): p. 140-6.

118. Greenwood, B., *The contribution of vaccination to global health: past, present and future.* Philos Trans R Soc Lond B Biol Sci, 2014. **369**(1645): p. 20130433.

119. Arya, S.C., *Human immunization in developing countries: practical and theoretical problems and prospects.* Vaccine, 1994. **12**(15): p. 1423-35.

120. Feyisa, D., et al., *Adherence to WHO vaccine storage codes and vaccine cold chain management practices at primary healthcare facilities in Dalocha District of Silt'e Zone, Ethiopia.* Trop Dis Travel Med Vaccines, 2022. **8**(1): p. 10.

121. Madan, M., et al., *Rational design of heat stable lyophilized rotavirus vaccine formulations.* Human Vaccines & Immunotherapeutics, 2018. **14**(9): p. 2132-2141.

122. Stratta, L., et al., *Economic Analysis of a Freeze-Drying Cycle.* Processes, 2020. **8**(11).

123. Costantino, H.R., et al., *The secondary structure and aggregation of lyophilized tetanus toxoid.* Journal of Pharmaceutical Sciences, 1996. **85**(12): p. 1290-1293.

124. Mark J. Papania, D.Z., Courtney Jarrahian, *Technologies to Improve Immunization*, in *Plotkin's Vaccines*. 2018. p. 1320-1353.

125. Toniolo, S.P., et al., *Excipient selection for thermally stable enveloped and non-enveloped viral vaccine platforms in dry powders.* International Journal of Pharmaceutics, 2019. **561**: p. 66-73.

126. Agarwal, S., et al., *Characterizing and Minimizing Aggregation and Particle Formation of Three Recombinant Fusion-Protein Bulk Antigens for Use in a Candidate Trivalent Rotavirus Vaccine.* Journal of Pharmaceutical Sciences, 2020. **109**(1): p. 394-406.

127. Kim, Y.C., et al., *Fabrication of microneedle patches with lyophilized influenza vaccine suspended in organic solvent.* Drug Delivery and Translational Research, 2021. **11**(2): p. 692-701.

128. Mistilis, M.J., A.S. Bommarius, and M.R. Prausnitz, *Development of a Thermostable Microneedle Patch for Influenza Vaccination.* Journal of Pharmaceutical Sciences, 2015. **104**(2): p. 740-749.

129. AL-Japairai, K.A.S., et al., *Current trends in polymer microneedle for transdermal drug delivery.* International Journal of Pharmaceutics, 2020. **587**.

130. Lawson, H.D., S.P. Walton, and C. Chan, *Metal-Organic Frameworks for Drug Delivery: A Design Perspective.* Acs Applied Materials & Interfaces, 2021. **13**(6): p. 7004-7020.

131. Stock, N. and S. Biswas, *Synthesis of Metal-Organic Frameworks (MOFs): Routes to Various MOF Topologies, Morphologies, and Composites.* Chemical Reviews, 2012. **112**(2): p. 933-969.

132. Ettlinger, R., et al., *Toxicity of metal-organic framework nanoparticles: from essential analyses to potential applications.* Chemical Society Reviews, 2022. **51**(2): p. 464-484.

133. Li, X., et al., *Encapsulation of enzyme by metal-organic framework for single-enzymatic biofuel cell-based self-powered biosensor.* Nano Energy, 2020. **68**.

134. Hongde An, M.L., Jia Gao, Zhenjie Zhang, Shengqian Ma, Yao Chen, *Incorporation of biomolecules in Metal-Organic Frameworks for advanced applications.* Coordination Chemistry Reviews, 2019. **384**: p. 90-106.

135. Chen, B.L., et al., *Zeolitic imidazolate framework materials: recent progress in synthesis and applications.* Journal of Materials Chemistry A, 2014. **2**(40): p. 16811-16831.

136. Gross, A.F., E. Sherman, and J.J. Vajo, *Aqueous room temperature synthesis of cobalt and zinc sodalite zeolitic imidizolate frameworks.* Dalton Transactions, 2012. **41**(18): p. 5458-5460.

137. Luzuriaga, M.A., et al., *Enhanced Stability and Controlled Delivery of MOF-Encapsulated Vaccines and Their Immunogenic Response In Vivo.* Acs Applied Materials & Interfaces, 2019. **11**(10): p. 9740-9746.

138. Xuchun Qiu, L.L., Wei Xu, Chen Chen, Ming Li, Yanhong Shi, Xiangyang Wu, Kun Chen, Chongchen Wang, *Zeolitic Imidazolate Framework-8 Nanoparticles Exhibit More Severe Toxicity to the Embryo/Larvae of Zebrafish (Danio rerio) When Co-Exposed with Cetylpyridinium Chloride.* Antioxidants, 2022. **11**(5): p. 945.

139. Kumar, P., et al., *Biological applications of zinc imidazole framework through protein encapsulation.* Applied Nanoscience, 2016. **6**(7): p. 951-957.

140. Wu, Q., et al., *A tumor treatment strategy based on biodegradable BSA@ZIF-8 for simultaneously ablating tumors and inhibiting infection.* Nanoscale Horizons, 2018. **3**(6).

141. Abdelhamid, H.N., *Biointerface Between ZIF-8 and Biomolecules and their Applications.* Biointerface Research in Applied Chemistry, 2021. **11**(1): p. 8283-8297.

142. Zhang, G.Q., et al., *Poly(ethylene glycol)-Mediated Assembly of Vaccine Particles to Improve Stability and Immunogenicity.* Acs Applied Materials & Interfaces, 2021. **13**(12): p. 13978-13989.

143. Singh, R., et al., *Biomimetic metal-organic frameworks as protective scaffolds for live-virus encapsulation and vaccine stabilization.* Acta Biomaterialia, 2022. **142**: p. 320-331.

144. *Protein Labeling Kits (For Alexa Fluor™, Pacific Blue™, Fluorescein-EX, and Oregon Green™ 488)*, Invitrogen, Editor. 2021, Thermo Fisher.

145. Esser, E.S., et al., *Tetanus vaccination with a dissolving microneedle patch confers protective immune responses in pregnancy.* Journal of Controlled Release, 2016. **236**: p. 47-56.

146. Li, S. and J.J. Gassensmith, *Synthesis of Metal–Organic Frameworks on Tobacco Mosaic Virus Templates*, in *Protein Scaffolds: Design, Synthesis, and Applications*, A.K. Udit, Editor. 2018, Springer New York: New York, NY. p. 95-108.

147. Mohan, S. and P.L. Foley, *Everything You Need to Know About Satisfying IACUC Protocol Requirements.* Ilar j, 2019. **60**(1): p. 50-57.

148. Gad, S.C., et al., *Tolerable Levels of Nonclinical Vehicles and Formulations Used in Studies by Multiple Routes in Multiple Species With Notes on Methods to Improve Utility.* International Journal of Toxicology, 2016. **35**(2): p. 95-178.

149. Baker, M.J., et al., *Using Fourier transform IR spectroscopy to analyze biological materials.* Nat Protoc, 2014. **9**(8): p. 1771-91.

150. Ji, Y., et al., *DFT-Calculated IR Spectrum Amide I, II, and III Band Contributions of N-Methylacetamide Fine Components.* ACS Omega, 2020. **5**(15): p. 8572-8578.

151. Wang, Q., et al., *GOx@ZIF-8(NiPd) Nanoflower: An Artificial Enzyme System for Tandem Catalysis.* Angewandte Chemie International Edition, 2017. **56**(50): p. 16082-16085.

152. Mittal, A., S. Gandhi, and I. Roy, *Mechanistic interaction studies of synthesized ZIF-8 nanoparticles with bovine serum albumin using spectroscopic and molecular docking approaches.* Scientific Reports, 2022. **12**(1): p. 10331.

153. Maddigan, N.K., et al., *Protein surface functionalisation as a general strategy for facilitating biomimetic mineralisation of ZIF-8.* Chemical Science, 2018. **9**(18): p. 4217-4223.

154. *Stability testing of new drug substances and products Q1A(R2)*. 2003, International conference on harmonisation.

155. Yin, H., et al., *Thermal stability of ZIF-8 under oxidative and inert environments: A practical perspective on using ZIF-8 as a catalyst support.* Chemical Engineering Journal, 2015. **278**: p. 293-300.

156. Alsarraf, H., et al., *Biophysical comparison of diphtheria and tetanus toxins with the formaldehyde-detoxified toxoids, the main components of diphtheria and tetanus vaccines.* Virulence, 2017. **8**(8): p. 1880-1889.

157. Waterman, K.C., *The application of the Accelerated Stability Assessment Program (ASAP) to quality by design (QbD) for drug product stability.* AAPS PharmSciTech, 2011. **12**(3): p. 932-7.

158. Kumar, V., et al., *Studies on the stability of tetanus and pertussis components of DPT vaccine on exposure to different temperatures.* Indian J Pathol Microbiol, 1982. **25**(1): p. 50-4.

159. Schwendeman, S.P., et al., *Stabilization of tetanus and diphtheria toxoids against moisture-induced aggregation.* Proceedings of the National Academy of Sciences, 1995. **92**(24): p. 11234-11238.

160. Deller, M.C., L. Kong, and B. Rupp, *Protein stability: a crystallographer's perspective.* Acta crystallographica. Section F, Structural biology communications, 2016. **72**(Pt 2): p. 72-95.

161. Eijsink, V.G., et al., *Rational engineering of enzyme stability.* J Biotechnol, 2004. **113**(1-3): p. 105-20.

162. Kumru, O.S., et al., *Vaccine instability in the cold chain: mechanisms, analysis and formulation strategies.* Biologicals, 2014. **42**(5): p. 237-59.

163. Zhou, H.-C., J.R. Long, and O.M. Yaghi, *Introduction to Metal–Organic Frameworks.* Chemical Reviews, 2012. **112**(2): p. 673-674.

164. Liang, K., et al., *Biomimetic mineralization of metal-organic frameworks as protective coatings for biomacromolecules.* Nature Communications, 2015. **6**(1): p. 7240.

165. Urabe, Y., et al., *Encapsulation of hemoglobin in mesoporous silica (FSM)-enhanced thermal stability and resistance to denaturants.* Chembiochem, 2007. **8**(6): p. 668-74.

166. Niu, Z., et al., *Synthesis and Characterization of Bionanoparticle-Silica Composites and Mesoporous Silica with Large Pores.* Nano Res., 2010. **2**: p. 474-483.

167. Tu, J., et al., *Mesoporous Silica Nanoparticles with Large Pores for the Encapsulation and Release of Proteins.* ACS Appl Mater Interfaces, 2016. **8**(47): p. 32211-32219.

168. Li, T., A.J. Senesi, and B. Lee, *Small Angle X-ray Scattering for Nanoparticle Research.* Chemical Reviews, 2016. **116**(18): p. 11128-11180.

169. Kikhney, A.G. and D.I. Svergun, *A practical guide to small angle X-ray scattering (SAXS) of flexible and intrinsically disordered proteins.* FEBS Lett, 2015. **589**(19 Pt A): p. 2570-7.

170. Mertens, H.D. and D.I. Svergun, *Structural characterization of proteins and complexes using small-angle X-ray solution scattering.* J Struct Biol, 2010. **172**(1): p. 128-41.

171. Korasick, D.A. and J.J. Tanner, *Determination of protein oligomeric structure from small-angle X-ray scattering.* Protein Sci, 2018. **27**(4): p. 814-824.

172. Lipfert, J. and S. Doniach, *Small-angle X-ray scattering from RNA, proteins, and protein complexes.* Annu Rev Biophys Biomol Struct, 2007. **36**: p. 307-27.

173. Brotherton, E.E., et al., *In Situ Small-Angle X-ray Scattering Studies During Reversible Addition–Fragmentation Chain Transfer Aqueous Emulsion Polymerization.* Journal of the American Chemical Society, 2019. **141**(34): p. 13664-13675.

174. Zhang, F., et al., *A General Small-Angle X-ray Scattering-Based Screening Protocol for Studying Physical Stability of Protein Formulations.* Pharmaceutics, 2021. **14**(1).

175. Putnam, C.D., *Guinier peak analysis for visual and automated inspection of small-angle X-ray scattering data.* J Appl Crystallogr, 2016. **49**(Pt 5): p. 1412-1419.

176. Burger, V.M., D.J. Arenas, and C.M. Stultz, *A Structure-free Method for Quantifying Conformational Flexibility in proteins.* Scientific Reports, 2016. **6**(1): p. 29040.

177. Grant, T.D., et al., *The accurate assessment of small-angle X-ray scattering data.* Acta Crystallogr D Biol Crystallogr, 2015. **71**(Pt 1): p. 45-56.

178. Liu, H. and P.H. Zwart, *Determining pair distance distribution function from SAXS data using parametric functionals.* Journal of Structural Biology, 2012. **180**(1): p. 226-234.

179. Pauw, B.R., *Everything SAXS:small-angle scattering pattern collection and correction.* J Phys Condens Matter, 2014. **26**(23): p. 239501.

180. Saliba, D., et al., *Crystal Growth of ZIF-8, ZIF-67, and Their Mixed-Metal Derivatives.* Journal of the American Chemical Society, 2018. **140**(5): p. 1812-1823.

181. Son, Y.-R., S.G. Ryu, and H.S. Kim, *Rapid adsorption and removal of sulfur mustard with zeolitic imidazolate frameworks ZIF-8 and ZIF-67.* Microporous and Mesoporous Materials, 2020. **293**: p. 109819.

182. Borzova, V.A., et al., *Kinetics of Thermal Denaturation and Aggregation of Bovine Serum Albumin.* PloS one, 2016. **11**(4): p. e0153495-e0153495.

183. Kumar, P., et al., *Biological applications of zinc imidazole framework through protein encapsulation.* Applied Nanoscience, 2016. **6**(7): p. 951-957.

184. Shade, D., B. Marszalek, and K.S. Walton, *Structural similarity, synthesis, and adsorption properties of aluminum-based metal-organic frameworks.* Adsorption, 2021. **27**(2): p. 227-236.

185. Pauw, B.R., et al., *The modular small-angle X-ray scattering data correction sequence.* J Appl Crystallogr, 2017. **50**(Pt 6): p. 1800-1811.

186. Wu, H., et al., *Controlled synthesis of highly stable zeolitic imidazolate framework-67 dodecahedra and their use towards the templated formation of a hollow Co3O4 catalyst for CO oxidation.* RSC Advances, 2016. **6**(9): p. 6915-6920.

187. Shahsavari, M., et al., *Synthesis and Characterization of GO/ZIF-67 Nanocomposite: Investigation of Catalytic Activity for the Determination of Epinine in the Presence of Dobutamine.* Micromachines, 2022. **13**(1): p. 88.

188. Rafiei, S., et al., *Efficient biodiesel production using a lipase@ZIF-67 nanobioreactor.* Chemical Engineering Journal, 2018. **334**: p. 1233-1241.

189. Nandiyanto, A.B.D., R. Oktiani, and R. Ragadhita, *How to Read and Interpret FTIR Spectroscope of Organic Material.* 2019, 2019. **4**(1): p. 22.

190. Guo, X., et al., *Controlling ZIF-67 crystals formation through various cobalt sources in aqueous solution.* Journal of Solid State Chemistry, 2016. **235**: p. 107-112.

191. Nyman, M. and L. McQuade, *Small Angle X-ray Scattering of Group V Polyoxometalates*. 2015. p. 151-170.

192. Jeffries, C.M., et al., *Preparing monodisperse macromolecular samples for successful biological small-angle X-ray and neutron-scattering experiments.* Nature protocols, 2016. **11**(11): p. 2122-2153.

193. Molodenskiy, D., et al., *Thermally induced conformational changes and protein–protein interactions of bovine serum albumin in aqueous solution under different pH and ionic strengths as revealed by SAXS measurements.* Physical Chemistry Chemical Physics, 2017. **19**(26): p. 17143-17155.

194. Singh, R., et al., *Biomimetic metal-organic frameworks as protective scaffolds for live-virus encapsulation and vaccine stabilization.* Acta Biomater, 2022. **142**: p. 320-331.

195. Wang, X., P.C. Lan, and S. Ma, *Metal–Organic Frameworks for Enzyme Immobilization: Beyond Host Matrix Materials.* ACS Central Science, 2020. **6**(9): p. 1497-1506.

196. Schofield, T.L., *Vaccine stability study design and analysis to support product licensure.* Biologicals, 2009. **37**(6): p. 387-396.

197. Ganar, K., et al., *Newcastle disease virus: current status and our understanding.* Virus Res, 2014. **184**: p. 71-81.

198. Vandelaer, J., et al., *Tetanus in developing countries: an update on the Maternal and Neonatal Tetanus Elimination Initiative.* Vaccine, 2003. **21**(24): p. 3442-5.

199. *Vaccine (Shot) for Tetanus*. Vacines for Your Children 2022.

200. Xu, X., et al., *Safety and Immunogenicity of a Recombinant Tetanus Vaccine in Healthy Adults in China: A Randomized, Double-Blind, Dose Escalation, Placebo- and Positive-Controlled, Phase 1/2 Trial.* Adv Sci (Weinh), 2021. **8**(15): p. e2002751.

201. Munn, A.S., et al., *Large-scale continuous hydrothermal production and activation of ZIF-8.* Chemical Communications, 2015. **51**(64): p. 12811-12814.

202. Carraro, F., et al., *Continuous-Flow Synthesis of ZIF-8 Biocomposites with Tunable Particle Size.* Angewandte Chemie International Edition, 2020. **59**(21): p. 8123-8127.

203. Wagner, A., et al., *Toxicity screening of two prevalent metal organic frameworks for therapeutic use in human lung epithelial cells.* Int J Nanomedicine, 2019. **14**: p. 7583-7591.

204. Secundo, F., *Conformational changes of enzymes upon immobilisation.* Chemical Society Reviews, 2013. **42**(15): p. 6250-6261.

205. Wu, C., et al., *Unveiling the thermolysis natures of ZIF-8 and ZIF-67 by employing in situ structural characterization studies.* Physical Chemistry Chemical Physics, 2019. **21**(32): p. 17571-17577.

206. Man, T., et al., *Hierarchically encapsulating enzymes with multi-shelled metal-organic frameworks for tandem biocatalytic reactions.* Nature Communications, 2022. **13**(1): p. 305.

207. Jung, S., et al., *Curcumin/Zeolitic Imidazolate Framework-8 Nanoparticle-Integrated Microneedles for pH-Responsive Treatment of Skin Disorders.* ACS Applied Nano Materials, 2022. **5**(9): p. 13671-13679.

208. Van Vleet, M.J., et al., *In Situ, Time-Resolved, and Mechanistic Studies of Metal–Organic Framework Nucleation and Growth.* Chemical Reviews, 2018. **118**(7): p. 3681-3721.

209. Burks, W., *Peanut allergy: a growing phenomenon.* J Clin Invest, 2003. **111**(7): p. 950-2.

210. Gupta, R.S., et al., *The prevalence, severity, and distribution of childhood food allergy in the United States.* Pediatrics, 2011. **128**(1): p. e9-17.

211. Al-Ahmed, N., S. Alsowaidi, and P. Vadas, *Peanut allergy: an overview.* Allergy Asthma Clin Immunol, 2008. **4**(4): p. 139-43.

212. Prescott, S. and K.J. Allen, *Food allergy: riding the second wave of the allergy epidemic.* Pediatr Allergy Immunol, 2011. **22**(2): p. 155-60.

213. Cox, L., M. Calderón, and O. Pfaar, *Subcutaneous allergen immunotherapy for allergic disease: examining efficacy, safety and cost-effectiveness of current and novel formulations.* Immunotherapy, 2012. **4**(6): p. 601-16.

214. Patrawala, M., et al., *Peanut Oral Immunotherapy: a Current Perspective.* Curr Allergy Asthma Rep, 2020. **20**(5): p. 14.

215. Hemmings, O., et al., *Ara h 2 is the dominant peanut allergen despite similarities with Ara h 6.* J Allergy Clin Immunol, 2020. **146**(3): p. 621-630.e5.

216. Tophof, M.A., et al., *Side effects during subcutaneous immunotherapy in children with allergic diseases.* Pediatr Allergy Immunol, 2018. **29**(3): p. 267-274.

217. Orenius, T., et al., *Fear of Injections and Needle Phobia Among Children and Adolescents: An Overview of Psychological, Behavioral, and Contextual Factors.* SAGE Open Nurs, 2018. **4**: p. 2377960818759442.

218. Keet, C.A. and R.A. Wood, *Emerging therapies for food allergy.* J Clin Invest, 2014. **124**(5): p. 1880-6.

219. Lucendo, A.J., A. Arias, and J.M. Tenias, *Relation between eosinophilic esophagitis and oral immunotherapy for food allergy: a systematic review with meta-analysis.* Ann Allergy Asthma Immunol, 2014. **113**(6): p. 624-9.

220. Dioszeghy, V., et al., *Epicutaneous immunotherapy results in rapid allergen uptake by dendritic cells through intact skin and downregulates the allergen-specific response in sensitized mice.* J Immunol, 2011. **186**(10): p. 5629-37.

221. Bloom, D. *FDA Denies Approval of Viaskin Peanut "Patch" Therapy*. 2020.

222. Calzada, D., et al., *Immunological Mechanisms in Allergic Diseases and Allergen Tolerance: The Role of Treg Cells.* J Immunol Res, 2018. **2018**: p. 6012053.

223. Berings, M., et al., *Advances and highlights in allergen immunotherapy: On the way to sustained clinical and immunologic tolerance.* J Allergy Clin Immunol, 2017. **140**(5): p. 1250-1267.

224. Jarvi, N.L. and S.V. Balu-Iyer, *Immunogenicity Challenges Associated with Subcutaneous Delivery of Therapeutic Proteins.* BioDrugs, 2021. **35**(2): p. 125-146.

225. Salmon, J.K., C.A. Armstrong, and J.C. Ansel, *The skin as an immune organ.* West J Med, 1994. **160**(2): p. 146-52.

226. Prausnitz, M.R., *Microneedles for transdermal drug delivery.* Adv Drug Deliv Rev, 2004. **56**(5): p. 581-7.

227. Kim, J.H., et al., *Successful transdermal allergen delivery and allergen-specific immunotherapy using biodegradable microneedle patches.* Biomaterials, 2018. **150**: p. 38-48.

228. Faraji Rad, Z., P.D. Prewett, and G.J. Davies, *An overview of microneedle applications, materials, and fabrication methods.* Beilstein J Nanotechnol, 2021. **12**: p. 1034-1046.

229. Haj-Ahmad, R., et al., *Microneedle Coating Techniques for Transdermal Drug Delivery.* Pharmaceutics, 2015. **7**(4): p. 486-502.

230. Shakya, A.K., C.H. Lee, and H.S. Gill, *Cutaneous vaccination with coated microneedles prevents development of airway allergy.* J Control Release, 2017. **265**: p. 75-82.

231. Jeong, S.Y., et al., *The Current Status of Clinical Research Involving Microneedles: A Systematic Review.* Pharmaceutics, 2020. **12**(11).

232. Prausnitz, M., *Inactivated influenza vaccine delivered by microneedle patch or by hypodermic needle.* US National Library of Medicine: Bethesda, MD, USA, 2019.

233. Branski, L.K., et al., *A porcine model of full-thickness burn, excision and skin autografting.* Burns, 2008. **34**(8): p. 1119-27.

234. Lee, J.W., J.H. Park, and M.R. Prausnitz, *Dissolving microneedles for transdermal drug delivery.* Biomaterials, 2008. **29**(13): p. 2113-24.

235. Laurent, P.E., et al., *Safety and efficacy of novel dermal and epidermal microneedle delivery systems for rabies vaccination in healthy adults.* Vaccine, 2010. **28**(36): p. 5850-6.

236. Crichton, M.L., et al., *The effect of strain rate on the precision of penetration of short densely-packed microprojection array patches coated with vaccine.* Biomaterials, 2010. **31**(16): p. 4562-72.

237. van der Maaden, K., et al., *Impact-insertion applicator improves reliability of skin penetration by solid microneedle arrays.* Aaps j, 2014. **16**(4): p. 681-4.

238. Feuille, E. and A. Nowak-Wegrzyn, *Allergen-Specific Immunotherapies for Food Allergy.* Allergy Asthma Immunol Res, 2018. **10**(3): p. 189-206.

239. Gautam, A., et al., *Topical Delivery of Protein and Peptide Using Novel Cell Penetrating Peptide IMT-P8.* Sci Rep, 2016. **6**: p. 26278.

240. Gill, H.S. and M.R. Prausnitz, *Coated microneedles for transdermal delivery.* J Control Release, 2007. **117**(2): p. 227-37.

241. Li, S., W. Li, and M. Prausnitz, *Individually coated microneedles for co-delivery of multiple compounds with different properties.* Drug Deliv Transl Res, 2018. **8**(5): p. 1043-1052.

242. *Thermo Fisher Scientific Pierce BCA Protein Assay Kit User Guide 2020*. [cited 2022 24 March]; Available from: https://assets.thermofisher.com/TFS-Assets/LSG/manuals/MAN0011430_Pierce_BCA_Protein_Asy_UG.pdf.

243. Martanto, W., et al., *Mechanism of fluid infusion during microneedle insertion and retraction.* J Control Release, 2006. **112**(3): p. 357-61.

244. Turner, N.J., D. Pezzone, and S.F. Badylak, *Regional variations in the histology of porcine skin.* Tissue Eng Part C Methods, 2015. **21**(4): p. 373-84.

245. Khiao In, M., et al., *Histological and functional comparisons of four anatomical regions of porcine skin with human abdominal skin.* Anat Histol Embryol, 2019. **48**(3): p. 207-217.

246. Chen, X., et al., *Dry-coated microprojection array patches for targeted delivery of immunotherapeutics to the skin.* J Control Release, 2009. **139**(3): p. 212-20.

247. Wang, P.M., et al., *Precise microinjection into skin using hollow microneedles.* J Invest Dermatol, 2006. **126**(5): p. 1080-7.

248. Jean Bolognia, J.V.S., Lorenzo Cerroni, *Dermatology*. 4th ed. Vol. 2. 2017: Elsevier.

249. Andrews, S.N., E. Jeong, and M.R. Prausnitz, *Transdermal delivery of molecules is limited by full epidermis, not just stratum corneum.* Pharm Res, 2013. **30**(4): p. 1099-109.

250. Johansen, P., et al., *New routes for allergen immunotherapy.* Hum Vaccin Immunother, 2012. **8**(10): p. 1525-33.

251. Gupta, R., et al., *The economic impact of childhood food allergy in the United States.* JAMA Pediatr, 2013. **167**(11): p. 1026-31.

252. Kaushik, S., et al., *Lack of pain associated with microfabricated microneedles.* Anesth Analg, 2001. **92**(2): p. 502-4.

253. Gill, H.S., et al., *Effect of microneedle design on pain in human volunteers.* Clin J Pain, 2008. **24**(7): p. 585-94.